DAVIDSON
LABORATOI

PROPELLER BLADE PRESSURE DI

DUE TO LOADING AND THICKNE

by

S. Tsakonas, W.R. Jacobs,

STEVENS INSTITUTE
OF TECHNOLOGY

CASTLE POINT STATION
HOBOKEN, NEW JERSEY 07030

REPORT DOCUMENTATION PAGE		READ INSTRUCTIONS BEFORE COMPLETING FORM
1. REPORT NUMBER SIT-DL-76-1869	2. GOVT ACCESSION NO.	3. RECIPIENT'S CATALOG NUMBER
4. TITLE (and Subtitle) Propeller Blade Pressure Distribution Due to Loading and Thickness Effects.		5. TYPE OF REPORT & PERIOD COVERED Final rept.
		6. PERFORMING ORG. REPORT NUMBER
7. AUTHOR(s) S. Tsakonas, W.R. Jacobs, M.R. Ali		8. CONTRACT OR GRANT NUMBER(s) N00014-75-C-0482 NEW
9. PERFORMING ORGANIZATION NAME AND ADDRESS Davidson Laboratory Stevens Institute of Technology Hoboken, N.J. 07030		10. PROGRAM ELEMENT, PROJECT, TASK AREA & WORK UNIT NUMBERS 93 p.
11. CONTROLLING OFFICE NAME AND ADDRESS David Taylor Naval Ship Research and Dev. Center Bethesda Maryland 20084		12. REPORT DATE April 1976
		13. NUMBER OF PAGES x + 47 pp. +18 figs. +18pp of App. A,B,C,D,E,
14. MONITORING AGENCY NAME & ADDRESS(if different from Controlling Office)		15. SECURITY CLASS. (of this report) Unclassified
		15a. DECLASSIFICATION/DOWNGRADING SCHEDULE

16. DISTRIBUTION STATEMENT (of this Report)

Approved for public release; distribution unlimited.

17. DISTRIBUTION STATEMENT (of the abstract entered in Block 20, if different from Report)

18. SUPPLEMENTARY NOTES

19. KEY WORDS (Continue on reverse side if necessary and identify by block number)

Hydrodynamics
Unsteady Theory for Propeller Blade Pressure Distribution

20. ABSTRACT (Continue on reverse side if necessary and identify by block number)

See Abstract (over)

ABSTRACT

A theoretical approach is developed and a computational procedure adapt-
able to a high speed digital computer is established for the evaluation of the
blade pressure distribution of a marine propeller due to thickness and loading
effects. The dual role of the blade thickness is considered. The contribution
of the "nonplanar thickness" to the propeller loading and pressure distribution
and the effect of the "flow distortion thickness" are studied by means of the
"thin body" approximation.

The surface integral equation which relates the unknown loading to the
known velocity distribution on the blades is solved by the mode approach in
conjunction with the "lift operator" technique. The analysis treats both design
and off-design conditions in steady-state and unsteady flows, and the proper
chordwise modes are selected for each condition.

The numerical solution yields the blade loading and resulting hydrodynamic
forces and moments and blade bending moments, and, in addition, the blade
pressure distributions on each blade face due to both loading and thickness
effects, thus providing information necessary for the prediction of cavitation
inception. Calculations have been performed for a set of three 3-bladed
propellers of different EAR operating in a screen-generated wake, for compar-
ison with experimental data.

STEVENS INSTITUTE OF TECHNOLOGY

DAVIDSON LABORATORY
CASTLE POINT STATION
HOBOKEN, NEW JERSEY

Report SIT-DL-76-1869

April 1976

PROPELLER BLADE PRESSURE DISTRIBUTION
DUE TO LOADING AND THICKNESS EFFECTS

by

S. Tsakonas, W.R. Jacobs, M.R. Ali

Approved by: _J. P. Breslin, Director_

DDC

OCT 20 1976

D

ABSTRACT

A theoretical approach is developed and a computational procedure adaptable to a high speed digital computer is established for the evaluation of the blade pressure distribution of a marine propeller due to thickness and loading effects. The dual role of the blade thickness is considered. The contribution of the "nonplanar thickness" to the propeller loading and pressure distribution and the effect of the "flow distortion thickness" are studied by means of the "thin body" approximation.

The surface integral equation which relates the unknown loading to the known velocity distribution on the blades is solved by the mode approach in conjunction with the "lift operator" technique. The analysis treats both design and off-design conditions in steady-state and unsteady flows, and the proper chordwise modes are selected for each condition.

The numerical solution yields the blade loading and resulting hydrodynamic forces and moments and blade bending moments, and, in addition, the blade pressure distributions on each blade face due to both loading and thickness effects, thus providing information necessary for the prediction of cavitation inception. Calculations have been performed for a set of three 3-bladed propellers of different EAR operating in a screen-generated wake, for comparison with experimental data.

KEYWORDS

Hydrodynamics
Unsteady Theory for Propeller Blade Pressure Distribution

TABLE OF CONTENTS

NOMENCLATURE

$A(\lambda)$	function defined in Eqs. (33) and (35)
a	π/J (nondimensional) inversely proportional to advance ratio at design condition
a_{od}	π/J_{od} (nondimensional) inversely proportional to advance ratio of off-design condition
$\bar{a}$	designation of NACA-a meanline
C_F, C_D	frictional coefficients
C_P	pressure coefficient
c	expanded chord length, ft.
$F_{x,y,z}$	propeller-induced forces in x,y,z direction (see Fig. 1)
f_c	camberline ordinates from face pitch line
f_τ	blade thickness distribution
$I_m(\ )$	modified Bessel function of first kind, of order m
$I^{(\bar{m})}(\ )$	defined in Eq. (20)
i	index
J	design advance ratio
J_{od}	off-design advance ratio
ΔJ	$J_{od} - J$
j	index
K	kernel of integral equation
$\bar{K}^{(\bar{m},\bar{n})}$	modified kernel after chordwise integrations
$K_m(\ )$	modified Bessel function of second kind of order m
k	variable of integration
$L^{(q)}(\rho, \theta_\alpha)$	loading distribution in lb/ft.
$L^{(q)}(r)$	spanwise loading in lb/ft.
$L^{(q,\bar{n})}(\rho)$	spanwise loading coefficients of the chordwise modes in lb/ft.

ℓ	integer multiple
M_b	blade bending moment about face pitch line
$M(\xi,\rho,\theta_o)$	source strength at point (ξ,ρ,θ_o)
m	index of summation
$\bar{m}$	order of lift operator
N	number of blades
n	blade index
n	rps
$\bar{n}$	order of chordwise mode
$\vec{n}$	unit normal vector on helicoidal surface at loading point
$\vec{n}'$	unit normal vector on helicoidal surface at control point
P	pressure, lb/ft^2
ΔP	$P_- - P_+$, pressure jump, lb/ft^2
$P(r)$	geometric pitch at each radial position, ft.
$Q_{x,y,z}$	propeller-induced moments about x,y,z axis (see Fig. 1)
q	order of harmonic of inflow field
R',R	Descartes distance
R_c	Reynolds number based on chord length
r	radial ordinate of control point
r_o	propeller radius, ft.
S	propeller lifting surface, ft^2
s	chordwise location as fraction of chord length
t	time, sec.
t_o	maximum thickness of blade, ft.
U	free stream velocity, ft/sec. (design)
U_{od}	free stream velocity, ft/sec. (off design)
u	variable of integration

$v^{(q)}(r)$	Fourier coefficients of the known downwash velocity distribution
V_c	normal velocity due to camber effects
V_f	normal velocity due to flow-incidence angle
V_N	normal velocity due to wake
V_τ	normal velocity due to nonplanar thickness
V_L	longitudinal perturbation velocity $(V_x - U)$
V_T	tangential perturbation velocity
V_x	measured axial velocity
W	velocity distribution normal to propeller
$W^{(q,\bar{m})}$	defined in Equation (20)
x	longitudinal ordinate of control point
x, r, ϕ	cylindrical coordinates of control point
x, y, z	Cartesian coordinate system
β	$\tan^{-1}(U/\Omega r) = \tan^{-1}(1/ar)$
δ	defined in Eq. (12)
$\Theta(\bar{n})$	chordwise mode shapes
Θ	$-\Omega t$ (see Fig. 2)
θ	angular ordinate of loading point
θ_o	angular position of loading point with respect to blade reference line, in moving coordinate system (see Fig. 2)
θ_b	subtended angle of projected blade semichord, radians
$\bar{\theta}_n$	$2\pi(n-1)/N$, $n = 1, 2, \dots N$
$\theta_p(r)$	geometric pitch angle at each radial position
θ_α	angular chordwise location of loading point (in trigonometric transformation Eq. 14)
$\Lambda^{(\bar{n})}(y)$	defined in Eq. (21) (see Appendix A)

$\Lambda_1^{(\bar{n})}(y)$	defined in Appendix A
ν	kinematic viscosity
ξ	longitudinal ordinate of loading point
ξ, ρ, θ	cylindrical coordinates of loading point
ρ	radial ordinate of loading point
ρ_f	mass density of fluid
ρ_o	ratio of leading edge radius to chord
σ	angular measure of skewness from blade reference line (see Fig. 2)
$\Delta\sigma$	$\sigma^r - \sigma^\rho$ = difference in skewness at control and loading point
τ	variable of integration
ϕ	velocity potential
$\phi(\bar{m})$	generalized lift operator (Eq. (18))
ϕ	angular ordinate of control point
ϕ_o	angular position of control point with respect to blade reference line, in moving coordinate system (see Fig. 2)
ϕ_α	angular chordwise location of control point (in trigonometric transformation Eq. 15)
Ψ	acceleration potential
Ω	magnitude of angular velocity of propeller
ω	angular frequency of loading

Superscripts

r	refers to control point
ρ	refers to loading point

INTRODUCTION

Davidson Laboratory has been engaged in a series of investigations concerned with the adaptation of the linearized unsteady lifting surface theory to the case of a marine propeller operating in a nonuniform flow field (see, for example, References 1-3), the objective of which has been the prediction of blade loading distributions, propeller-generated forces and moments and blade bending moments. In these investigations, it has been assumed that the lifting surfaces (blades) have zero thickness.

The linearized wing theory considers that an arbitrary wing cross-section is composed of a symmetrical part corresponding to its thickness distribution and an asymmetrical part of zero thickness but with camber and angle of attack. The asymmetrical part contributes to the lift of the wing. On the other hand, the thickness distribution contributes nothing to the lifting properties of a wing unless it is nonplanar.

The marine propeller with its blade describing a helicoidal surface is one of the few nonplanar lifting surfaces. The blade thickness plays a dual role, influencing both the lifting and non-lifting characteristics of the blade. As part of the nonplanar surface, it will induce a continuous component of velocity on points of the surface itself, thus affecting the blade loading distribution. On the other hand, the symmetrical flow disturbance caused by the blade thickness will influence the pressure distributions on the suction and pressure sides of the blade without contributing to the net blade loading. Both effects, designated for brevity as due to "nonplanar" thickness and "flow distortion" thickness, will occur in steady-state flow conditions since the blade thickness is a time-independent quantity.

The study of the blade pressure distribution arising from both loading and thickness effects has been undertaken so that the necessary information can be obtained for cavitation and blade stress analyses. The study treats both design and off-design conditions.

The surface integral equation which relates the unknown loading to the known velocity distribution on the blade is solved by the mode approach in conjunction with the "lift operator" technique. The selection of the proper chordwise modes in the steady-state flow condition at design advance ratio J is dictated by the shape of the loading distribution in two-dimensional flow on a foil with the same camber distribution (NACA - $\bar{a}$ mean lines, NACA mean lines of the 4- and 5-digit wing series, lenticular mean line, etc.). At off-design J in the steady-state condition, there is an angle of attack due to the difference ΔJ and the additional loading (to that at design J) due to this angle of attack is represented by the first (cotangent) term of the known Birnbaum chordwise modes. The complete Birnbaum modes, which have the proper leading edge singularity and satisfy the Kutta condition at the trailing edge, are used to represent the chordwise loading distribution in the unsteady flow conditions at both design and off-design J.

The linearized unsteady lifting surface theory requires the singular behavior at the leading edge. Although the singularity is integrable, its presence in the blade pressure distributions is unrealistic. Therefore, whenever the Birnbaum modes are used, a correction factor to remove the leading edge singularity based on Van Dyke's[4] and Lighthill's[5] method is introduced in the blade pressure distribution.

I. AN OUTLINE OF THE ANALYSIS

In the analysis which follows, the blades of any ship propeller are treated as warped lifting surfaces which encounter the spatially varying inflow and, hence, develop unsteady forces which are cyclic functions of blade position. The blades need not be of a pure helicoidal surface, i.e., they may have varying pitch over the radius. However, the reference surface, along which the shed vorticity is considered to be convected, is restricted to be a pure helicoid whose local pitch is fixed by the joint action of the forward speed of the ship and the tangential velocity at any radius, or simply the pitch angle of this vortex-wake surface is $\tan^{-1}(\frac{U}{r\Omega})$.

The theory is formulated to give the linearized pressure distribution on each side of the blade at eight radial locations. These distributions are made up of an antisymmetric part associated with the lifting action of the blade and a symmetric part developed by the blade thickness distribution. As the blade surface is non-planar, the flow produced at any element by all other thickness elements produces a weak normal flow and this flow is balanced by the induction of anti-symmetric loading elements which, in turn, contribute to the pressure distribution as well as to the forces and moments. This small loading is referred to as being the result of the presence of non-planar thickness; the major part of the asymmetrical loading is produced by the presence of camber, geometric flow angle and the normal velocity components associated with the hull spatially variable wake. The anti-symmetric part of the blade pressure distributions are solely responsible for the forces, whereas the symmetrical and asymmetrical contributions determine the pressures on each side, the knowledge of which is essential for prediction of cavitation inception.

A. Propeller Loading Distribution

1. Integral Equation

The linearized unsteady lifting surface theory for a marine propeller, with its blades lying on a helicoidal surface and operating in non-uniform flow of an incompressible, ideal fluid, is formulated by means of the acceleration potential method. It is based on a small perturbation approximation and, also, on the assumptions that the propeller blades are thin and operate without cavitation and flow separation.

It is known that the pressure field generated by a lifting sur-
face S is given by distributed doublets with axis parallel to the local
normal and with strength equal to the pressure jump across the surface.
If the acceleration potential function, ψ, a scalar function of position,
is introduced and defined as having its gradient equal to the accelera-
tion vector, then the strength of the doublet distribution is propor-
tional to the discontinuity of ψ between the values for the positive
and negative oriented surfaces with respect to the direction of the nor-
mal $\vec{n}$, i.e.,

$$\Delta\psi = \psi_+ - \psi_- = \frac{1}{\rho_f}(P_- - P_+) = \frac{1}{\rho_f}\Delta P \tag{1}$$

Here use is made of the linearized relation between the acceleration po-
tential and the perturbation pressure, viz.,

$$\psi = -\frac{P}{\rho_f} \tag{2}$$

where P is local pressure and ρ_f is fluid mass density. Thus, the pres-
sure jump is defined as that between the pressure at the back (suction
side) and the pressure at the face (pressure side) of the blade.

The pressure P at any point (x,r,ϕ) (in cylindrical coordinates)
at time t due to all pressure doublets distributed over dummy (loading)
points (ξ,ρ,θ) will be given by

$$P(x,r,\phi;t) = \frac{-1}{4\pi} \iint_S \Delta P(\xi,\rho,\theta;t) \frac{\partial}{\partial n} \frac{dS}{R'(x,r,\phi;\xi,\rho,\theta)} \tag{3}$$

where $\frac{\partial}{\partial n}$ is the normal derivative on the surface S at the loading
point (ξ,ρ,θ), with $\vec{n}$ the unit normal vector having positive
axial component

and $R'(x,r,\phi;\xi,\rho,\theta) = [(x-\xi)^2 + r^2 + \rho^2 - 2r\rho\cos(\theta-\phi)]^{1/2}$ is the Descartes
distance between the given control point (x,r,ϕ) and the loading
point (ξ,ρ,θ).

The relation between the velocity potential function ϕ and the
acceleration potential function ψ has been established by solving the
Euler equation of motion:

$$\phi(x,r,\phi;t) = \frac{1}{U} \int_{-\infty}^{x} \psi(\tau,r,\phi;t - \frac{x-\tau}{U})d\tau \qquad (4)$$

where U is the undisturbed forward velocity of the lifting surface and the integral represents the total effect at time t of all previous accelerations of a fluid particle at present at the observation point x.

For doublets with pulsating strength $\Delta P(\xi,\rho,\theta)e^{i\omega t}$ at loading points (ξ,ρ,θ) which, together with the observation (control) points (x,r,ϕ) are rotating with angular velocity $-\Omega$ (where the negative sign is introduced to accord with a right-handed coordinate system), Eq. (3) becomes

$$\psi(x,r,\phi_o;t) = + \frac{1}{4\pi\rho_f} \iint_S \Delta P(\xi,\rho,\theta_o)e^{i\omega t}\frac{\partial}{\partial n} \frac{dS}{R'(x,r,\phi_o-\Omega t;\xi,\rho,\theta_o-\Omega t)}$$

$$(5)$$

where ω = frequency in radians/sec.

θ_o,ϕ_o = angular position of loading, control points with respect to blade reference line in moving coordinate system (Fig. 2).

Substituting Eq. (5) in Eq. (4) and identifying the lifting surfact as the helicoidal surface, $x = \phi_o/a$ or $\xi = \theta_o/a$, of an N-bladed propeller yields

$$\phi(x,r,\phi_o;t) = + \frac{1}{4\pi\rho_f U} \sum_{n=1}^{N} e^{iq\Omega t} \iint_S \Delta P^{(q)}(\xi,\rho,\theta_o)$$

$$\cdot \int_{-\infty}^{x} e^{iq[a(\tau-x) - \bar{\theta}_n]} \frac{\partial}{\partial n}(\frac{1}{R})d\tau dS \qquad (6)$$

where $a = \Omega/U$

$q = \omega/\Omega$ = order of blade harmonic

$\bar{\theta}_n = 2\pi(n-1)/N, \quad n = 1,2,\dots N$

$R = \{(\tau-\xi)^2 + r^2 + \rho^2 - 2r\rho \cos[\theta_o - \phi_o + \bar{\theta}_n - a(\tau-x)]\}^{1/2}$

Then the induced velocity at the control point $(x,r,\phi_o;t)$ due to the loading at $(\xi,\rho,\theta_o;t)$, when both points are located on the propeller blades, can be determined from Eq. (6). The normal component of the velocity induced by all elements will be given by

$$\frac{\partial}{\partial n'}\phi(x,r,\phi_o;t) \qquad (7)$$

5

where $\vec{n}'$ is the unit normal vector on the helicoidal surface at the control point, having a positive axial component.

The requirement for an impermeable boundary (i.e., no flow through the lifting surface) is

$$W + \frac{\partial}{\partial n'} \phi(x,r,\phi_o;t) = 0$$

where W is the known (imposed) perturbation velocity normal to any blade chord

$$W = - \frac{\partial}{\partial n'} \phi(x,r,\phi_o;t)$$

which expresses the equality of the negative of self-induced normal velocity with the imposed velocity in the downwash (positive n') direction. This yields the integral equation for the unknown pressure change ΔP at frequency q:

$$W = \frac{-e^{iq\Omega t}}{4\pi\rho_f U} \sum_{n=1}^{N} \iint_S \Delta P^{(q)}(\xi,\rho,\theta_o) \frac{\partial}{\partial n'} \int_{-\infty}^{x} e^{iq[a(\tau-x)-\bar{\theta}_n]} \frac{\partial}{\partial n} \left(\frac{1}{R}\right) d\tau dS \qquad (8)$$

where

$$\frac{\partial}{\partial n} = \frac{\rho}{\sqrt{1 + a^2 r^2}} \left(a \frac{\partial}{\partial \xi} - \frac{1}{\rho^2} \frac{\theta}{\partial \theta_o}\right)$$

$$\qquad (9)$$

$$\frac{\partial}{\partial n'} = \frac{r}{\sqrt{1 + a^2 r^2}} \left(a \frac{\partial}{\partial x} - \frac{1}{r^2} \frac{\partial}{\partial \phi_o}\right)$$

It should be noted that the left side of Equation (8) is the component of the flow normal to the nose tail line of any section of the propeller blade, whereas the right side is the induced velocity normal to the helicoidal reference surface. This lack of precise identity in resolution of the onset flow and the flow induced by all loading elements is in keeping with the linearized small-perturbation theory employed. Specifically, the onset flow normal to the nose tail line is (upon omitting camber for the present) expressed by

6

$$W = -\sqrt{(U + V_L)^2 + (\Omega r + V_T)^2}\sin(\theta_p - \tan^{-1}(\frac{U + V_L}{\Omega r + V_T}))$$

where V_L and V_T are longitudinal and tangential perturbation velocities. When this is expanded to secure the first order approximation (defined for the condition $V_L = V_T = 0$), we obtain

$$W = -\sqrt{U^2 + (\Omega r)^2}\sin(\theta_p - \beta) + (V_L\cos\theta_p - V_T\sin\theta_p)$$

and, for small values of $\theta_p - \beta$, this reduces to the linear approximation

$$W = -\sqrt{U^2 + (\Omega r)^2}(\theta_p - \beta) + (V_L\cos\theta_p - V_T\sin\theta_p)^*$$

Here $\beta = \tan^{-1}\frac{U}{\Omega r} = \tan^{-1}\frac{1}{ar}$ and θ_p is the pitch angle of the propeller.

It is to be noted also that blades with zero camber, zero thickness and having pitch angle variation $\theta_p \equiv \beta$ when set into a flow with zero perturbation, i.e., $V_L = V_T = 0$, will experience no crossflow and, hence, will develop no pressure loading. Thus, all these quantities, incidence angle, camber, hull wake and inductions from non-planar thickness are considered as perturbations of the reference flow whose direction is defined by β and which, by itself, produces zero loading. The effects of each of these imposed flows on the blades are calculated separately and simply added together as allowed by the linearity of the theory.

The left-hand side of Eq. (8) can be written in the form

$$W = \sum_{q=0} V^{(q)}(r, \phi_0)e^{-iq\Theta} \tag{10}$$

where $\Theta = -\Omega t$ in terms of a moving coordinate system and V is in complex form. All but the hull wake are perturbations from the steady-state flow only, $q = 0$, and are analytically computed from the propeller geometry. The normal wake velocities are derived from an harmonic analysis of the wake measurements as will be shown in a later section.

---

[*] See J.P. Breslin, "Determination of the Normal Velocity to a Propeller Blade Section in a Ship Wake," Tech. Memo. SIT-DL-76-172, January 1976.

On utilizing Eq. (10), the integral equation (8) requires at each frequency q that

$$v^{(q)}(r)e^{-iq\phi_0} = \iint_S \Delta P^{(q)}(\xi,\rho,\theta_0) \, K(r,\phi_0;\rho,\theta_0;q)dS \tag{11}$$

where the kernel function is given by

$$K(r,\phi_0;\rho,\theta_0;q) = -\frac{1}{4\pi\rho_f U} \lim_{\delta\to 0} \sum_{n=1}^{N} e^{-iq\bar{\theta}_n} \frac{\partial}{\partial n'} \int_{-\infty}^{x} e^{iqa(\tau-x)} \frac{\partial}{\partial n}(\frac{1}{R})d\tau \tag{12}$$

and $\quad \delta = \dfrac{\theta_0 - \phi_0}{a} - (x-\xi).$

The time factor has been eliminated from both sides of Eq. (11) and it is understood that the real part of the solution must be taken at the end. The limiting process is introduced in the kernel function to avoid the mathematical difficulty due to the presence of a high-order singularity. The kernel function is one of the most complex of lifting surface theory since, in addition to its high-order singularity, it presents other complications arising from the helicoidal surface and from the interference of the other blades. Thus, attention is given to the numerical solution of the integral equation by means of a high-speed digital computer. The analysis has been carried to the stage where laborious computations can be efficiently performed by the numerical procedure.

It has been assumed that the shape of the chordwise loading distribution is the same as that in two-dimensional flow; the spanwise distribution is left to be determined by the solution of the integral equation. A method called the "generalized lift operator" technique[1] is applied which reduces the surface integral equation to a line integral equation along the propeller radius. Then, by the collocation method, the line integral equation is reduced to a set of algebraic equations in the unknown spanwise loading distribution.

The mathematical complexity of the problem has imposed a series of concessions with regard to propeller geometry and helicoidal blade wake. To save time and expense in computing, a most important concession was that of approximating the blade helicoidal wake in "staircase" fashion,[2] which appears to be physically realistic. However, with improvement of the high-speed digital computers, the exact treatment of the blade wake[3] is being utilized.

Following Ref. (3), the substitutions listed below are made in Eq. (11),

$$L^{(q)}(\rho,\theta_\alpha) = \Delta P^{(q)}(\xi,\rho,\theta_o) \cdot \rho\theta_b^\rho \quad (\text{lb/ft}) \tag{13}$$

$$\theta_o \equiv \sigma^\rho - \theta_b^\rho \cos\theta_\alpha \quad , \quad 0 \leq \theta_\alpha \leq \pi \tag{14}$$

$$\phi_o \equiv \sigma^r - \theta_b^r \cos\phi_\alpha \quad , \quad 0 \leq \phi_\alpha \leq \pi \tag{15}$$

$$\text{and} \quad \frac{1}{R} = \frac{1}{\pi} \sum_{m=-\infty}^{\infty} e^{im[\theta_o-\phi_o+\bar{\theta}_n-a(\tau-x)]} \int_{-\infty}^{\infty} I_m(|k|\rho)K_m(|k|r)e^{i(\tau-\xi)k}dk \tag{16}$$

for $\rho < r$. (If $\rho > r$, ρ and r are interchanged in the modified Bessel functions $I_m(\ )$ and $K_m(\ )$ of the first and second kinds.) Here σ is the angular position of the midchord line from the generator line through the hub in the projected propeller plane, θ_b is the subtended angle of the projected blade semichord, θ_α and ϕ_α are angular chordwise locations of the loading and control points, respectively, and the superscripts ρ and r refer to values at loading and control points, respectively.

After the appropriate chordwise mode shapes $\theta(\bar{n})$ are introduced, so that

$$L^{(q)}(\rho,\theta_\alpha) = \sum_{\bar{n}=1}^{\bar{n}\,max} L^{(q,\bar{n})}(\rho)\,\theta(\bar{n}) \tag{17}$$

where $L^{(q,\bar{n})}(\rho)$ are the spanwise loading components to be determined by the solution of the integral equations, the chordwise integration of the kernel (Eq. (12)) over θ_α is performed. Then both sides of the integral equation (11) are operated upon by the "generalized" lift operator ; thus,

$$\frac{1}{\pi} \int_0^\pi \phi(\bar{m}) \ \{Eq. \ (11)\} \ d\phi_\alpha \tag{18}$$

where

$$\phi(1) = 1 - \cos\phi_\alpha \quad \text{(the Glauert lift operator)}$$

$$\phi(2) = 1 + 2 \cos\phi_\alpha$$

$$\phi(\bar{m}) = \cos(\bar{m}-1)\phi_\alpha \quad \text{for} \quad \bar{m} > 2$$

A set of line integral equations is thus obtained with maximum order $\bar{m}$ equal to maximum $\bar{n}$ of chordwise modes:

$$\frac{W^{(q,\bar{m})}(r)}{U} = \sum_{\bar{n}=1}^{\bar{n} \ max} \int_\rho L^{(q,\bar{n})}(\rho) \ \bar{K}^{(\bar{m},\bar{n})}(r,\rho;q)d\rho \tag{19}$$

where

$$\frac{W^{(q,\bar{m})}(r)}{U} = \frac{1}{\pi} \int_0^\pi \phi(\bar{m}) \ \frac{\{V^{(q)}(r)e^{-iq\phi_o}\}d\phi_\alpha}{U} = \frac{V^{(q)}(r)}{U} \ e^{-iq\sigma^r} \ I^{(\bar{m})}(q\theta_b^r) \tag{20}$$

$$I^{(\bar{m})}(q\theta_b^r) = \frac{1}{\pi} \int_0^\pi \phi(\bar{m}) \ e^{iq\theta_b^r \cos\phi_\alpha} d\phi_\alpha$$

$I^{(\bar{m})}(y)$ is given for various $\bar{m}$ in Appendix A.

The modified kernel function after the θ_α and ϕ_α chordwise integrations is finally (see Ref. 3):

$$\bar{K}^{(\bar{m},\bar{n})} = \{\frac{-N}{4\pi\rho_f U^2 r_o}\} \ \frac{r}{a\sqrt{1+a^2 r^2}} \ \sum_{\substack{m=-\infty \\ m=q+\ell N}}^\infty e^{-im\Delta\sigma}$$

$$\cdot \ \{e^{i(m-q)\Delta\sigma}[a^2(m-q) + \frac{m}{r^2}] \ [a^2(m-q) + \frac{m}{\rho^2}] \ I^{(\bar{m})}(q\theta_b^r)\Lambda^{(\bar{n})}(q\theta_b^\rho) \ \cdot$$

$$\cdot \; I_m(a|m-q|\rho) \; K_m(a|m-q|r)$$

$$-\frac{i}{\pi} \int_{-\infty}^{\infty} (ak+\frac{m}{r^2})(ak+\frac{m}{\rho^2}) e^{i\frac{k}{a}\Delta\sigma} \frac{\Lambda^{(\overline{m})}((m-\frac{k}{a})\theta_b^r) \Lambda^{(\overline{n})}((m-\frac{k}{a})\theta_b^\rho)}{k-a(m-q)} I_m(|k|\rho) K_m(|k|r) dk \}$$

$$(21)$$

where $\Lambda^{(\overline{n})}(z) = \int_o^\pi \Theta(\overline{n}) e^{-iz\cos\theta_\alpha} \sin\theta_\alpha d\theta_\alpha$ and $\Delta\sigma = \sigma^r - \sigma^\rho$.

In Eq. (21), all terms outside the first braces are nondimensionalized with respect to propeller radius r_o as is also ρ in Eq. (19). $\Lambda^{(\overline{n})}(z)$ for various $\overline{n}$ and $\Theta(\overline{n})$ is also given in Appendix A.

The integral equations given by Eq. (19) with the kernel given by Eq. (21) are solved numerically by the usual collocation method, with the loading $L^{(q,\overline{n})}(\rho)$ assumed to be constant over each small radial strip. Then only the kernel needs to be integrated over the radial strip.

Reference 3 details the analytical development and the various numerical procedures to obtain the finite contributions of the Cauchy-type singularity of the k-integral at $k = a(m-q)$ and of the higher order Hadamard-type singularity when $\rho = r$.

2. *Chordwise Modes*

The proper selection of chordwise modes is dictated by the loading distribution on a foil in two-dimensional flow. Thus, in the unsteady flow case, the unknown loading function is approximated in the chordwise direction by the known Birnbaum distribution which has the proper leading edge singularity and satisfies the Kutta condition at the trailing edge. In this case, Eq. (17) is

$$L^{(q)}(\rho,\theta_\alpha) = \sum_{\overline{n}=1}^{\overline{n}\,max} L^{(q,\overline{n})}(\rho) \; \Theta(\overline{n})$$

$$= \frac{1}{\pi} \{ L^{(q,1)} \cot\frac{\theta_\alpha}{2} + \sum_{\overline{n}=2}^{\overline{n}\,max} L^{(q,\overline{n})}(\rho) \sin(\overline{n}-1)\theta_\alpha \} \quad (22a)$$

In the steady-state flow condition, the chordwise mode shapes are selected to conform to the observed pressure distributions of the NACA foil sections. Furthermore, the analysis and corresponding program is divided into two parts, for design and off-design propeller conditions.

At design advance ratio J, the propeller operates at almost optimum efficiency and the chordwise loading distribution due to blade camber, thickness, angle of attack and inflow conditions (mean wake effects) does not deviate much in shape from the loading distribution of an airfoil in two-dimensional flow. At off-design advance ratio, however, the same propeller in the same wake is subjected to a change in angle of attack due to ΔJ, the difference between off-design and design advance ratio. The additional load distribution, due to this change in angle of attack in the off-design condition, is in accordance with thin wing theory represented by the first term of Eq. (22a).

The camber distribution is a decisive factor in the selection of the proper mode shapes of the chordwise loading distribution in the steady-state flow condition, since it is known that many properties of wing sections are primarily functions of the shape of the mean line. Thus, the program in the steady-state case deals with two different types of mode shapes.

The first is appropriate to the NACA-$\bar{a}$ mean lines characterized by the fact that the chordwise loading is constant from $x/c = 0$ at the leading edge to $x/c = \bar{a}$ ($\bar{a}$ varying from 0 to 1) and then decreases linearly to zero at $x/c = 1$, the trailing edge. For brevity, this type is designated as "roof-top" loading. In this case, Eq. (17) becomes

$$L^{(o)}(\rho,\theta_\alpha) = L(\rho)^{(o,1)} \Theta(1) = \begin{cases} L(\rho)^{(o,1)}, & 0 \leq x \leq \bar{a} \\ L(\rho)^{(o,1)} \left(\dfrac{1-x}{1-\bar{a}}\right), & \bar{a} \leq x \leq 1 \end{cases} \qquad (22b)$$

and $\Lambda^{(1)}(z)$ of Eq. (21) is as given in Appendix A.

The second type of mode shape in the steady flow case is appropriate to NACA mean lines of the 4- and 5-digit wing series (including the lenticular mean line) and to arbitrary mean lines in general which are characterized by the fact that the chordwise loading is finite everywhere and zero at both edges and can thus be described by a series of sine mode shapes:

$$L^{(o)}(\rho,\theta_\alpha) = \frac{1}{\pi} \sum_{\bar{n}=1}^{\bar{n}\,max} L(\rho)^{(o,\bar{n})} \sin \bar{n}\,\theta_\alpha \qquad (22c)$$

12

It is to be noted that, when the complete Birnbaum mode series, Eq. (22a), or the cotangent term alone, is used and the solutions for the span-wise loadings are substituted in the chordwise distribution, a correction for the leading-edge singularity is introduced based on Van Dyke's and Lighthill's method[4],[5].

3. Perturbation Velocity Distributions

As mentioned earlier, the left-hand side of the integral equation represents the positive normal components of the velocity perturbations from the basic flow due to non-uniformity of the flow (wake), to blade camber, blade thickness (non-planar) and incident flow angle, in the design condition, and to an additional angle of attack in the off-design condition arising from the difference between off-design and design advance ratios.

a) Normal Velocity Due to Wake

This is the contribution of the flow non-uniformity to $V^{(q)}(r)/U$ of Eq. (20). The positive normal component (i.e. downwash) of the wake velocity along the middle chord of each radial strip is given by

$$\frac{V_N(r)}{U} = \frac{V_L(r)}{U} \cos\theta_p(r) - \frac{V_T(r)}{U} \sin\theta_p(r)$$

where

$$\frac{V_L(r)}{U} = -1 + \frac{V_x}{U} \qquad , \qquad \text{perturbation of uniform flow}$$

$$\frac{V_x(r)}{U} = \text{measured axial velocity}$$

$$\frac{V_T(r)}{U} = \text{measured tangential velocity}$$

$$\theta_p(r) = \tan^{-1}\frac{P(r)}{2\pi r r_o}$$

$P(r)$ = propeller pitch, ft.

r_o = propeller radius, ft.

r = radial distance in terms of r_o

13

so that

$$\frac{V_N(r)}{U} = [\frac{V_x(r)}{U} - 1] \cos\theta_p(r) - \frac{V_T(r)}{U} \sin\theta_p(r) \tag{23}$$

It is to be noted that the present sign convention requires that, looking forward, the positive position angles θ are defined counterclockwise from $\theta = 0$ at the upright position of the blade, that the axial component of the wake V_x is positive downstream (positive x-direction) and the tangential component V_T is positive in the counterclockwise direction.

The harmonic analysis of the measured wakes yields

$$\frac{V_x(r)}{U} = a_o(r) + \sum_{q=1}^{\infty} [a_q(r)\cos q\theta + b_q(r)\sin q\theta]$$

$$\frac{V_T(r)}{U} = A_o(r) + \sum_{q=1}^{\infty} [A_q(r)\cos q\theta + B_q(r)\sin q\theta]$$

The zero harmonic of the normal velocity is then

$$\frac{V_N^{(o)}(r)}{U} = (a_o(r) - 1) \cos\theta_p(r) - A_o(r) \sin\theta_p(r) \tag{23a}$$

and the other harmonics are

$$\frac{V_N^{(q)}(r)}{U} = [a_q(r) \cos\theta_p(r) - A_q(r) \sin\theta_p(r)]\cos q\theta$$

$$+ [b_q(r) \cos\theta_p(r) - B_q(r) \sin\theta_p(r)]\sin q\theta \tag{23b}$$

As stated previously (see Eq. (10)), the left-hand side of the integral equation must be in complex form

$$\frac{\bar{w}^{(q)}}{U} = [(\frac{V_N^{(q)}}{U})_R + i(\frac{V_N^{(q)}}{U})_I]e^{-iq\theta}$$

14

and it is understood that the real part is to be taken eventually. The real part is

$$(\frac{V_N^{(q)}}{U})_R \cos q\theta + (\frac{V_N^{(q)}}{U})_I \sin q\theta$$

Therefore, the input to the program for the real part is from Eq. (23b)

$$(\frac{V_N^{(q)}(r)}{U})_R = a_q(r) \cos\theta_p(r) - A_q(r) \sin\theta_p(r) \tag{24}$$

and for the imaginary part

$$(\frac{V_N^{(q)}(r)}{U})_I = b_q(r) \cos\theta_p(r) - B_q(r) \sin\theta_p(r)$$

b) Normal Velocity Due to Blade Camber

The velocity V_c normal to the blade in negative direction induced by the flow disturbance caused by blade camber is independent of time (since the blades are considered rigid) so that only the steady state loading is affected. The loading due to camber effect is obtained, therefore, from the steady-state part of integral equation (19) with $V^{(o)}(r)/U$ of (20) replaced by

$$\frac{V_c^{(o)}(r)}{U} = \frac{\sqrt{1 + a^2 r^2}}{c(r)} \frac{\partial f_c(r,s)}{\partial s}$$

$$= \frac{2\sqrt{1 + a^2 r^2}}{c(r) \sin\phi_\alpha} \frac{\partial f_c(r,\phi_\alpha)}{\partial \phi_\alpha} \tag{25}$$

where

$\frac{\partial f_c(r,s)}{\partial s}$ = slope of the camberline $f_c(r,s)$ given at discrete points measured from the face pitch line

$s = (1 - \cos\phi_\alpha)/2$, chordwise location non-dimensionalized on the basis of $c(r)$

$c(r)$ = chord in feet

ϕ_α = angular chordwise position

15

On application of the generalized lift operator (see Eq. (18)) to both sides of the integral equation, the left-hand side of Eq. (19) for this particular component, camber, becomes for each order $\bar{m}$

$$\frac{\bar{V}_c^{(o,\bar{m})}(r)}{U} = \frac{2\sqrt{1 + a^2 r^2}}{c(r)} \int_0^\pi \Phi(\bar{m}) \frac{\partial f_c}{\partial \phi_\alpha} \frac{d\phi_\alpha}{\sin\phi_\alpha} \tag{26}$$

where, as can be seen from Eq. (18), $\Phi(\bar{m})$ can be expressed in terms of $\cos m\phi_\alpha$. Integrating by parts

$$\frac{1}{c(r)} \int \frac{\cos m\phi}{\sin\phi} \frac{\partial f_c}{\partial \phi} d\phi = \frac{f_c(r,s)\cos m\phi}{c(r)\sin\phi}$$

$$+ \frac{1}{c(r)} \int \frac{f_c(r,s)}{\sin^2\phi} [m \sin m\phi \sin\phi + \cos m\phi \cos\phi] d\phi \tag{27}$$

In the small range near the leading edges, $0 \leq \phi \leq \cos^{-1}(0.9)$ or $0 \leq s \leq 0.05$, the camberline is assumed to be parabolic and, in the range $\cos^{-1}(-.8) \leq \phi \leq \pi$ or $0.90 \leq s \leq 1.0$ near the trailing edge, the camberline is assumed to be a straight line. The integration is done analytically in these regions and numerically over the remainder of the chord.[6] The required input information is the ratio of camber ordinate $f_c(r,s)$ to chord $c(r)$ at 19 equidistant positions from $s = 0.05$ to 0.95 of chord. For arbitrary camber, these ratios are read into the program. The program has options to compute them in the cases of NACA-$\bar{a}$ meanlines ($\bar{a} = 0.8$, 0.8 modified, 1.0) and of lenticular (sine-squared) camberline from the ratio of maximum camber ordinate to chord at each radial position, and in the case of the NACA-4 digit series from the ratio of maximum camber ordinates to chord and the chordwise position of the maximum ordinate.

c) Normal Velocity Due to "non-planar" Blade Thickness

The thickness of propeller blades describing a helicoidal or non-planar surface, as stated earlier, generates a velocity field on the blade itself and, consequently, affects its loading distribution (in the steady-state only since the blades are considered rigid). The normal velocity component due to the effect is

$$\frac{v_\tau^{(o)}}{U} = -\frac{1}{U} \frac{\partial \phi_\tau(x, r, \phi_o; 0)}{\partial n'} \tag{28}$$

16

where $\partial/\partial n'$ is as defined in Eq. (9).

Resorting to the "thin body" approximation, the velocity potential Φ_τ is given by that of the source-sink distribution with strength proportional to the slope of the thickness distribution. In the case of an N-blade propeller, the velocity potential is given by

$$\Phi_\tau(x,r,\phi_o) = -\frac{1}{4\pi} \sum_{n=1}^{N} \int_{\theta_o} \int_{\rho} \frac{M(\xi,\rho,\theta_o)}{R} \frac{\sqrt{1+a^2\rho^2}}{a\rho} \rho \, d\rho \, d\theta_o \qquad (29)$$

Here the source strength M is

$$M(\xi,\rho,\theta_o) = 2U \sqrt{1+a^2\rho^2} \frac{df_\tau(\rho,o)}{\partial s} = 2U \frac{\partial f_\tau(\xi,\rho,\theta_o)}{\partial \xi}$$

where $f_\tau(\xi,\rho,\theta_o)$ = thickness distribution over one side of the blade section at radial position ρ in the propeller plane.

The Descartes distance R is

$$R = \{ (x-\xi)^2 + r^2 + \rho^2 - 2r\rho \cos(\theta_o - \phi_o + \bar{\theta}_n) \}^{1/2}$$

where $x = \phi_o/a = (\sigma^r - \theta_b^r \cos\phi_\alpha)/a$, $0 \le \phi_\alpha \le \pi$

$\xi = \theta_o/a = (\sigma^\rho - \theta_b^\rho \cos\theta_\alpha)/a$, $0 \le \theta_\alpha \le \pi$

$\bar{\theta}_n = 2\pi(n-1)/N$, $n = 1,2,\ldots N$

If the reciprocal of R is again expressed in a series as in Eq. (16), then

$$\frac{\partial}{\partial n'}\left(\frac{1}{R}\right) = \frac{i}{\pi} \frac{r}{\sqrt{1+a^2 r^2}} \sum_{m=-\infty}^{\infty} e^{im(\theta_o - \phi_o + \bar{\theta}_n)} \int_{-\infty}^{\infty} \left(ak + \frac{m}{r^2}\right)(IK)_m \, e^{i(x-\xi)k} dk$$

where $(IK)_m = \begin{cases} I_m(|k|\rho)K_m(|k|r) , & \rho < r \\ I_m(|k|r)K_m(|k|\rho) , & \rho > r \end{cases}$

Since $\sum_{n=1}^{N} e^{im\bar{\theta}_n} = \begin{cases} N & \text{for } m = \ell N, \ \ell = 0, \pm 1, \pm 2,\ldots \\ 0 & \text{for all other } m \end{cases}$

and $d\theta_o = \theta_b^\rho \sin\theta_\alpha d\theta$ and $\frac{\partial}{\partial \xi} = \frac{a}{\theta_b^\rho \sin\theta_\alpha} \frac{\partial}{\partial \theta_\alpha}$

Equation (28) can be reduced to

$$\frac{V_\tau^{(o)}(r)}{U} = \frac{iNr}{2\pi^2 \sqrt{1+a^2r^2}} \sum_{\substack{m=-\infty \\ m=\ell N}}^{\infty} e^{-im\Delta\sigma} \int_o^\pi \int_\rho \frac{\partial f_\tau(\rho,\theta_\alpha)}{\partial\theta_\alpha} \sqrt{1+a^2\rho^2}$$

$$\cdot \int_{-\infty}^{\infty} (ak + \frac{n}{r^2})(IK)_m e^{i\Delta\sigma k/a} e^{i(k-am)\theta_b^\rho \cos\theta_\alpha/a}$$

$$\cdot e^{-i(k-am)\theta_b^r \cos\phi_\alpha/a} dk \, d\sigma \, d\theta_\alpha \tag{30}$$

Before the θ_α-integration can be performed, it is necessary to supply an analytical expression for the thickness distribution $f_\tau(\rho,\theta_\alpha)$. When the NACA 4 and 5-digit wing series were derived, it was found that the ratio of thickness distribution y_τ to maximum thickness t_o of efficient wing sections were nearly the same when their camber was removed (mean line straightened).[7] The thickness distribution of these sections is given by

$$\frac{y_\tau}{c} = \pm \frac{t_o}{c} (1.4845\sqrt{x} - .630x - 1.758x^2 + 1.4215x^3 - .5075x^4)$$

where c is the chord length, x is the chordwise location, $0 \leq x \leq 1$, and the coefficient of $\sqrt{x}$ is equal to $\sqrt{2\rho_o}$, ρ_o being the ratio of the leading edge radius to the chord c. In general, for any propeller the blade thickness distribution in the projected plane can be approximated by

$$f_\tau(\rho,\theta_\alpha) \simeq 2\rho\theta^\rho \{\sqrt{2\rho_o(\rho)} \sqrt{x} + \frac{t_o(\rho)}{c(\rho)} [ax + bx^2 + cx^3 + dx^4]\}$$

and with $x = \frac{1-\cos\theta_\alpha}{2}$, $0 \leq \theta_\alpha \leq \pi$

$$f_\tau(\rho,\theta_\alpha) \simeq 2\rho\theta_b^\rho \{\sqrt{2\rho_o(\rho)} \sin\frac{\theta_\alpha}{2} + \frac{t_o(\rho)}{c(\rho)}[a_o(\rho) + \sum_{n=1}^{4} a_n(\rho)\cos n\theta_\alpha]\} \tag{31}$$

where f_τ and ρ are fractions of propeller radius r_o, $\rho_o(\rho)$ is the ratio of leading edge radius to chord length $c(\rho)$ at a given radial position and t_o/c is the ratio of maximum thickness to chord at that radial position. The coefficients of the fourth-order polynomial in x are calculated by the "least squares" method and then with the trigonometric substitution for x, the coefficients a_n of Eq. (31) are obtained and inserted in the input to the program.

The slopes of the thickness distribution are, from Eq. (31)

$$\frac{\partial f_\tau(\rho,\theta_r)}{\partial \theta_\alpha} = \rho\theta_b^\rho \sqrt{2\rho_o(\rho)} \cos\frac{\theta_\alpha}{2} - 2\rho\theta_b^\rho \frac{\tau_o(\rho)}{c(\rho)} \sum_{n=1}^{4} na_n(\rho)\sin n\theta_\alpha \} \quad (32)$$

Letting

$$A((k-am)\theta_b^\rho/a) = \int_0^\pi \frac{\partial f_\tau(\rho,\theta_\alpha)}{\partial \theta_\alpha} e^{i((k-am)\theta_b^\rho/a)\cos\theta_\alpha} d\theta_\alpha \quad (33)$$

and applying the generalized lift operator, Equation (30) becomes for each lift operator mode $\bar{m}$

$$\frac{\bar{V}_\tau^{(o,\bar{m})}(r)}{U} = \frac{iNr}{2\pi^2 \sqrt{1+a^2r^2}} \sum_{\substack{m=-\infty \\ m\approx \ell N}}^{\infty} e^{-im\Delta\sigma} \int_\rho \sqrt{1+a^2\rho^2}$$

$$\cdot \int_{-\infty}^{\infty} (ak+\frac{m}{r^2})(IK)_m e^{i\Delta\sigma k/a} I^{(\bar{m})}((am-k)\theta_b^r/a)A((k-am)\theta_b^\rho/a)dkd\rho \quad (34a)$$

Let $u = k - am$, then

$$\frac{\bar{V}_\tau^{(o,\bar{m})}(r)}{U} = \frac{iNr}{2\pi^2\sqrt{1+a^2r^2}} \int_\rho \sqrt{1+a^2\rho^2}$$

$$\cdot \sum_{\ell=-\infty}^{\infty} \int_{-\infty}^{\infty} [au+\ell N(a^2+\frac{1}{r^2})] I_{\ell N}(|u+a\ell N|\rho)K_{\ell N}(|u+a\ell N|r)e^{i\Delta\sigma u/a}$$

$$\cdot I^{(\bar{m})}(-u\theta_b^r/a)A(u\theta_b^\rho/a)dud\rho \quad (34b)$$

(for $\rho < r$).

Finally

$$\frac{\bar{V}_\tau^{(o,\bar{m})}(r)}{U} = - \frac{Nr}{\pi^2\sqrt{1+a^2r^2}} \int_\rho \sqrt{1+a^2\rho^2} \int_0^\infty Im.Part\{e^{i\Delta\sigma u/a} I^{(\bar{m})}(-u\theta_b^r/a)A(u\theta_b^\rho/a)\}$$

$$\cdot \{au I_o(u\rho)K_o(ur) + \sum_{\ell=1}^{\infty} \{[au+\ell N(a^2+\frac{1}{r^2})] I_{\ell N}(|u+a\ell N|\rho)K_{\ell N}(|u+a\ell N|r)$$

$$+ [au-\ell N(a^2+\frac{1}{r^2})] I_{\ell N}(|u-a\ell N|\rho)K_{\ell N}(|u-a\ell N|r)]\}dud\rho \quad (34c)$$

(for $\rho < r$, otherwise ρ and r are interchanged in the modified Bessel functions.) As can be seen from Appendix B

$$A(\lambda) = \rho\theta_b^\rho \sqrt{2\rho_o(\rho)}\; B(\lambda) - 2\rho\theta_b^\rho \frac{t_o(\rho)}{c(\rho)} \{2a_1(\rho)G(\lambda) + 3a_3(\rho)[6G(\lambda) - \frac{16}{\lambda}F(\lambda)]$$

$$+ i\; 8a_2(\rho)\; F(\lambda) \qquad\qquad (35)$$

$$+ i\; \frac{32a_4(\rho)}{\lambda}[4G(\lambda) + (\lambda - \frac{12}{\lambda})F(\lambda)]\}$$

where $B(\lambda) = \int_0^\pi e^{i\lambda\cos\theta}\cos\frac{\theta}{2}\,d\theta$ (See Appendix B, 5)

$$G(\lambda) = \frac{\sin\lambda}{\lambda}$$

$$F(\lambda) = \frac{\sin\lambda - \lambda\cos\lambda}{\lambda^2}$$

(It can be shown that when u = 0 the integrand of (34c) is zero.)

   d) Normal Velocity Due to Flow Angle

   The incident flow angle has been defined as the difference between the geometric pitch angle $\theta_p(r) = \tan^{-1}(P(r)/2\pi r)$ and the hydrodynamic pitch angle $\beta(r) = \tan^{-1}(1/ar)$ of the assumed helicoidal surface. The normal velocity (in the positive direction) $V_f^{(o)}(r)/U$ due to this effect depends only on the radial position, *not on the chordwise* ϕ_α position, and is given by

$$\frac{V_f^{(o)}(r)}{U} = -\sqrt{1 + a^2r^2}[\theta_p(r) - \beta(r)]$$

Therefore, after application of the generalized lift operator, it becomes

$$\frac{V_f^{(o,\bar{m})}(r)}{U} = \begin{cases} -\sqrt{1 + a^2r^2}[\theta_p(r) - \beta(r)] & \text{for } \bar{m} = 1 \text{ or } 2 \\ 0 & \text{for } \bar{m} > 2 \end{cases} \qquad (36)$$

since $I^{(1)}(0) = I^{(2)}(0) = 1$ and $I^{(\bar{m} > 2)}(0) = 0$. (See Appendix A)

   In Eq. (36) $a = \pi/J$ where J is design advance ratio. At off-design advance ratio J_{od}, the propeller is subjected to a change in angle of attack due to $\Delta J = J_{od} - J$. The normal velocity *perturbation* due to this change in angle of attack is

20

$$\frac{\Delta \bar{V}_f^{(o,\bar{m})}}{U_{od}} = \{-\sqrt{1 + a_{od}^2 r^2}[\theta_p(r) - \tan^{-1}\frac{J_{od}}{\pi r}] + \sqrt{1 + a^2 r^2}[\theta_p(r) - \beta(r)](U/U_{od})\}$$

(37)

for $\bar{m} = 1$ or 2, where $a_{od} = \pi/J_{od}$ and U_{od} is the off-design forward velocity.

4. Blade Pressure Distributions, Hydrodynamic Forces and Moments and Blade Bending Moments

a) Pressure Distribution

After the integral equation (19) is solved for propeller spanwise loading components $L^{(q,\bar{n})}(\rho)$ (lb/ft) due to the various perturbation velocity distributions, the spanwise loading distribution is determined from Eq. (17):

$$L^{(q)}(r) = \int_0^\pi L^{(q)}(r,\theta_\alpha)\sin\theta_\alpha d\theta_\alpha$$

$$= \int_0^\pi \sum_{\bar{n}=1}^{\bar{n}\,max} L^{(q,\bar{n})}(r)\,\Theta(\bar{n})\sin\theta_\alpha d\theta_\alpha$$

(38)

For the unsteady loading due to wake $(q \neq 0)$, the complete Birnbaum series is used with the chordwise loading distribution given by Eq. (22a). The spanwise loading distribution is, in this case,

$$L^{(q)}(r) = \frac{1}{\pi}\int_0^\pi \{L^{(q,1)}(r)(1 + \cos\theta_\alpha) + \sum_{n=2}^{\bar{n}\,max} L^{(q,\bar{n})}(r)\sin(\bar{n}-1)\theta_\alpha \sin\theta_\alpha\}d\theta_\alpha$$

$$= L^{(q,1)}(r) + \frac{1}{2} L^{(q,2)}(r)$$

(39a)

For the steady loading due to ΔJ in the off-design condition, the spanwise loading distribution is the first term of Eq. (39a).

In the steady state case $(q = 0)$ for NACA $\bar{a}$ mean line blade sections, the chordwise loading distribution is the so-called "roof-top" distribution, given by Eq. (22b), which can also be expressed as

$$L^{(o)}(r) = \begin{cases} L^{(o,1)}(r) & \text{for } 0 \leq \theta_\alpha \leq \cos^{-1}(1-2\bar{a}) \\ L^{(o,1)}(r)\,\dfrac{1 + \cos\theta_\alpha}{2(1-\bar{a})} & \text{for } \cos^{-1}(1-2\bar{a}) \leq \theta_\alpha \leq \pi \end{cases}$$

The spanwise loading distribution in this case is

21

$$L^{(o)}(r) = L^{(o,1)}(r) \left\{ \int_0^{\cos^{-1}(1-2\bar{a})} \sin\theta_\alpha d\theta_\alpha + \frac{1}{2(1-\bar{a})} \int_{\cos^{-1}(1-2\bar{a})}^{\pi} (1+\cos\theta_\alpha)\sin\theta_\alpha d\theta_\alpha \right\}$$

$$= L^{(o,1)}(r) \, (\bar{a}+1) \tag{39b}$$

The steady chordwise loading distribution for NACA mean lines of the 4- and 5-digit wing series and for arbitrary mean lines in general is given by Eq. (22c). The spanwise loading distribution is then given as

$$L^{(o)}(r) = \frac{1}{\pi} \int_0^{\pi} \sum_{\bar{n}=1} L^{(o,\bar{n})}(r) \, \sin\bar{n}\theta_\alpha \, \sin\theta_\alpha d\theta_\alpha$$

$$= \frac{1}{2} L^{(o,1)}(r) \tag{39c}$$

The chordwise pressure distributions in lb/ft^2 are obtained by dividing the chordwise loading distribution by the semi-chord in feet (see Eq. (13)).

Whenever the cotangent Birnbaum mode is used, the Van Dyke or Lighthill correction[4],[5] is applied to the chordwise pressure distribution to remove the physically unrealizable leading edge singularity.

Their simple rule for obtaining a uniformly valid solution is

$$\bar{C}_{P_1} = \frac{s}{s + \rho_o/2} \, C_{P_1}$$

where C_{P_1} = pressure coefficient according to first-order thin airfoil theory
s = $(1-\cos\theta_\alpha)/2$ = chordwise location from the leading edge in terms of chord length
ρ_o = leading edge radius of the profile in terms of chord length

The modified chordwise loading distribution is then

$$L^{(q)}(r,\theta_\alpha) = \frac{1}{\pi} \left(\frac{1-\cos\theta_\alpha}{1+\rho_o-\cos\theta_\alpha} \right) \left\{ L^{(q,1)}(r)\cot\frac{\theta_\alpha}{2} + \sum_{\bar{n}=2} L^{(q,\bar{n})}(r)\sin(\bar{n}-1)\theta_\alpha \right\} \tag{40}$$

Since the pressure near the leading edge is governed by the first term of (40), viz.,

$$\frac{1-\cos\theta_\alpha}{1+\rho_o-\cos\theta_\alpha} \cot\frac{\theta_\alpha}{2} = \frac{\sin\theta_\alpha}{1+\rho_o-\cos\theta_\alpha}$$

the location of maximum pressure near the leading edge is determined apparently from

$$\frac{d}{d\theta_\alpha} \frac{\sin\theta_\alpha}{1+\rho_o-\cos\theta_\alpha} = 0$$

Thus $(\cos\theta_\alpha)_{max} = 1/(1+\rho_o)$. This is the chordwise location of a point where the maximum pressure near the leading edge will occur after the application of the Van Dyke-Lighthill correction, provided ρ_o is not too large. If $\rho_o > .015$, the sine series of (40) will influence the location of maximum pressure near the leading edge.

b) Propeller-generated Forces and Moments

The principal components of the hydrodynamic forces and moments which are evaluated are listed below and shown in Figure 1 with the sign convention adopted:

Forces: F_x = thrust (x-direction)

F_y and F_z = horizontal and vertical components, respectively, of the bearing forces

Moments: Q_x = torque about the x-axis

Q_y and Q_z = bending moments about the y- and z-axis, respectively

The total forces at frequency $\ell N(\ell = 0,1,2...)$ induced by an N-bladed propeller are determined as (see Appendix C)

$$F_x = Re\{Nr_o e^{i\ell N\Omega t} \int_0^1 L^{(\ell N)}(r)\cos\theta_p(r)dr\}$$

$$F_y = Re\{\frac{Nr_o}{2} e^{i\ell N\Omega t} \int_0^1 \sum_{\bar{n}=1} [L^{(\ell N-1,\bar{n})}(r)\Lambda^{(\bar{n})}(-\theta_b^r) + L^{(\ell N+1,\bar{n})}(r)\Lambda^{(\bar{n})}(\theta_b^r)]$$

$$\sin\theta_p(r)dr\}$$

$$F_z = \text{Re } \{\frac{-Nr_o}{2i} e^{i\ell N\Omega t} \int_o^1 \sum_{\bar{n}=1} [L^{(\ell N-1,\bar{n})}(r)\Lambda^{(\bar{n})}(-\theta_b^r) - L^{(\ell N+1,\bar{n})}(r)\Lambda^{(\bar{n})}(\theta_b^r)]$$

$$\sin\theta_p(r)dr\} \tag{41a}$$

The moments are determined by:

$$Q_x = -\text{Re } \{Nr_o^2 e^{i\ell N\Omega t} \int_o^1 L^{(\ell N)}(r)\sin\theta_p(r)rdr\}$$

$$Q_y = \text{Re } \{\frac{Nr_o^2}{2} e^{i\ell N\Omega t} \int_o^1 \{ \sum_{\bar{n}=1} [L^{(\ell N-1,\bar{n})}(r)\Lambda^{(\bar{n})}(-\theta_b^r) + L^{(\ell N+1,\bar{n})}(r)\Lambda^{(\bar{n})}(\theta_b^r)]\cos\theta_p(r)$$

$$+ \sum_{\bar{n}=1} [L^{(\ell N-1,\bar{n})}(r)\Lambda_1^{(\bar{n})}(-\theta_b^r) - L^{(\ell N+1,\bar{n})}(r)\Lambda_1^{(\bar{n})}(\theta_b^r)](i\theta_b^r)\sin\theta_p(r)\tan\theta_p(r)\}rdr\}$$

$$Q_z = \text{Re}\{\frac{-Nr_o^2}{2i} e^{i\ell N\Omega t} \int_o^1 \{ \sum_{\bar{n}=1} [L^{(\ell N-1,\bar{n})}(r)\Lambda^{(\bar{n})}(-\theta_b^r) - L^{(\ell N+1,\bar{n})}(r)\Lambda^{(\bar{n})}(\theta_b^r)]\cos\theta_p(r)$$

$$+ \sum_{\bar{n}=1} [L^{(\ell N-1,\bar{n})}(r)\Lambda_1^{(\bar{n})}(-\theta_b^r) + L^{(\ell N+1,\bar{n})}(r)\Lambda_1^{(\bar{n})}(\theta_b^r)](i\theta_b^r)\sin\theta_p(r)\tan\theta_p(r)\}rdr.$$

$$\tag{41b}$$

where $\Lambda^{(\bar{n})}(z)$ and $\Lambda_1^{(\bar{n})}(z)$ are as defined in Appendix A.

It is seen from Eqs. (41a,b) that the transverse bearing forces and bending moments are evaluated from propeller loading components $L^{(q,\bar{n})}(r)$ associated with wake harmonics at frequencies adjacent to blade frequency, i.e. at $q = \ell N \pm 1$, whereas the thrust and torque are determined from the loading $L^{(q)}(r)$ (given by Eqs. 39a,b,c) at blade frequency $q = \ell N$. At $\ell = 0$ (steady-state) the mean transverse forces and bending moments are determined at shaft frequency. Thus:

$$\bar{F}_y = \text{Re } \{\frac{Nr_o}{2} \int_o^1 [\sum_{\bar{n}=1} L^{(1,\bar{n})}(r)\Lambda^{(\bar{n})}(\theta_b^r)]\sin\theta_p(r)dr\}$$

$$\bar{F}_z = \text{Re } \{\frac{Nr_o}{2i} \int_o^1 [\sum_{\bar{n}=1} L^{(1,\bar{n})}(r)\Lambda^{(\bar{n})}(\theta_b^r)]\sin\theta_p(r)dr\}$$

$$\bar{Q}_y = Re \{ \frac{Nr_o^2}{2} \int_0^1 \{ [\sum_{\bar{n}=1} L^{(1,\bar{n})}(r) \Lambda^{(\bar{n})}(\theta_b^r) \cos\theta_p(r) -$$

$$[\sum_{\bar{n}=1} L^{(1,\bar{n})}(r) \Lambda_1^{(\bar{n})}(\theta_b^r)] (i\theta_b^r) \sin\theta_p(r) \tan\theta_p(r) \} r dr \}$$

$$\bar{Q}_z = Re \{ \frac{NR_o^2}{2i} \int_0^1 \{ [\sum_{\bar{n}=1} L^{(1,\bar{n})}(r) \Lambda^{(\bar{n})}(\theta_b^r) \cos\theta_p(r) -$$

$$[\sum_{\bar{n}=1} L^{(1,\bar{n})}(r) \Lambda_1^{(\bar{n})}(\theta_b^r)] (i\theta_b^r) \sin\theta_p(r) \tan\theta_p(r) \} r dr \} \qquad (41c)$$

All forces and moments can be written in the form

$$R_e [c^{(q)} e^{i\phi_q} e^{-iq\theta}] = c^{(q)} \cos(-q\theta + \phi_q) = c^{(q)} \cos(q\theta - \phi_q)$$

where θ is blade angular position, *positive in the counter-clockwise direction* from zero at the upright position (12M), q is order of shaft frequency, $c^{(q)}$ is magnitude of force or moment, and ϕ_q is phase angle (electrical) determined as the angle whose tangent is the imaginary part (sine part) over the real part (cosine part). (The program output gives $c^{(q)}$ and ϕ_q.)

In comparing phase angles with those of experiment, care should be taken to ascertain if measured values refer to lead or lag position and if the quantity considered is at peak or trough. When the theoretical ϕ_q is positive, the peak (or trough) of the quantity is to the left of the upright position, i.e., leads. When ϕ_q is negative, the peak (or trough) is to the right of the upright position and lags that of input.

c) *Blade Bending Moments*

The blade bending moment about the face pitch line at any radius r_j of a blade is calculated from the chordwise integrated loading (span-wise component) $L^{(q)}(r)$ at any shaft frequency q as

$$M_b^{(q)} e^{iq\Omega t} = r_o^2 e^{iq\Omega t} \int_{r_j}^{1} L^{(q)}(r) \cos[\theta_p(r) - \theta_p(r_j)](r - r_j) dr \tag{42}$$

The positive blade bending moment about the face-pitch line is that which puts the face of the blade in compression (see Figure 1).

The instantaneous blade bending moment distribution when the propeller swings around its shaft in the clockwise direction is

$$M_b = R_e \sum_q M_b^q e^{-iq\theta} = \sum_q |M_b^q| \cos(q\theta - \phi_q) \tag{43}$$

where ϕ_q is the phase angle (electrical) determined by

$$\phi_q = \tan^{-1} \frac{(M_b^q)_{Im}}{(M_b^q)_{Re}}$$

and $(M_b^q)_{Re}, (M_b^q)_{Im}$ are real and imaginary parts of M_b^q.

It should be noted that in the program the value of r_j of Eq. (42) is limited to any of the midpoints of the radial strips into which the blade span is divided, at which points the pitch angles, as well as other geometrical characteristics, are given as input. The bending moment at

any other radial position can be obtained by interpolation or extrapolation. For example, for $r_j < (r_1 - \Delta r)$, where r_1 is the midpoint of the initial radial strip from the hub, r_h, and Δr is the span of the radial strip $(r_1 = r_h + \Delta r/2)$, the bending moment can be estimated as

$$M_b(r_j) = M_b(r_1) - \frac{[M_b(r_1) - M_b(r_2 = r_1 + \Delta r)]}{\Delta r}(r_j - r_1)$$

For the case of bending moment about the root r_h, this formula gives

$$M_b(r_h) = M_b(r_1) + \frac{M_b(r_1) - M_b(r_2)}{2}$$

5. *Frictional Thrust and Torque*

To obtain the frictional contribution to thrust and torque, one must resort to empirical formulae for the frictional coefficient in turbulent flow since, in this case, the theoretical analysis is extremely difficult. Hoerner[8] suggests a formula based on statistical analysis of measured velocity distributions across the boundary layer, viz. the Prandtl-Schlichting formula for the friction coefficient for one side of a smooth flat plate of length c:

$$C_F = \frac{0.455}{(\log_{10} R_c)^{2.58}} \tag{44}$$

where R_c is Reynolds number based on length c (of the expanded chord) i.e., in the nomenclature of this paper,

$$R_c(r) = \frac{U\sqrt{1 + a^2 r^2}\ c(r)}{\nu}$$

where ν is kinematic viscosity.

Because of thickness, the average velocity around a symmetrical foil section is higher than that of the undisturbed flow, the increase being proportional to the thickness ratio t_o/c. For the conventional section, the total frictional drag coefficient is approximated by[8]

$$C_D(r) = [2\ C_F(r)]\left(1 + 2\ \frac{t_o(r)}{c(r)}\right) \tag{45}$$

27

Although no allowance is made for viscous pressure drag, nor drag associated with the deviation of the local flow direction from that along the nose-tail line, this formula agrees basically with theoretical analyses of skin-friction drag and is substantiated by experimental results[8].

Taking $\Delta F_D(r)$ (elemental friction force) as the friction force per foot of propeller blade span with

$$\Delta F_D(r) = \frac{1}{2} \rho_f U^2 \ (1 + a^2 r^2) \ c(r) \ C_D(r) \tag{46}$$

for an N-bladed propeller, the total force in the positive x-direction and moment about the x-axis due to skin-friction drag are

$$F_{Dx} = N \int_r \Delta F_D(r) \ \sin\theta_p(r) \ dr$$

and

$$Q_{Dx} = N \int_r \Delta F_D(r) \ \cos\theta_p(r) \ r \ dr$$

On substitution of (44) - (46) and noting that the expanded chord length is equivalent to

$$c(r) = \frac{2 \, r \, r_o \, \theta_b^r}{\cos \theta_p(r)}$$

where r is a fraction of propeller radius r_o, the frictional thrust and torque become

$$F_{Dx} = N r_o^2 \ \rho_f U^2 \ \int_o^1 2 C_F(r) \, [1 + 2 \ \frac{t_o(r)}{c(r)}] \, (1 + a^2 r^2) \, r \theta_b^r \ \tan\theta_p(r) \, dr$$

$$Q_{Dx} = N r_o^3 \ \rho_f U^2 \ \int_o^1 2 C_F(r) \, [1 + 2 \ \frac{t_o(r)}{c(r)}] \, (1 + a^2 r^2) \, r^2 \theta_b^r \ dr$$

$$\tag{47}$$

F_{Dx} and Q_{Dx} are added algebraically to F_x and Q_x, respectively, as calculated in the preceding section. Thrust will be decreased slightly and torque increased more noticeably.

As was mentioned earlier, this is a first attempt to incorporate the frictional thrust and torque in the program; in the event of any improvement of the estimated frictional coefficient, this portion of the program can be easily modified.

B. *Thickness Effects (Non-lifting)*

With the propeller in translatory and rotational motion, an additional flow disturbance is generated about the propeller blade section due to the blade thickness distribution; the fluid is pushed equally to both sides, influencing the pressure distribution on both suction and pressure sides of the blade without contributing to the net blade loading. As noted previously, this effect will occur in steady flow conditions only since the blades are considered rigid. The pressure distribution resulting from this "flow distortion" thickness will be studied in this section by means of the "thin body" approximation.

The velocity potential due to source-sink distributions approximating the symmetrical thickness distribution of an N-bladed propeller is given by

$$\Phi(x,r,\phi_0;0) = -\frac{1}{4\pi} \sum_{n=1}^{N} \iint_S \frac{M(\rho,s)}{R} dS$$

$$= -\frac{1}{4\pi} \sum_{n=1}^{N} \int_0^{\pi} \int_\rho \frac{M(\rho,s)}{R} \frac{\sqrt{1+a^2\rho^2}}{a\rho} \rho\theta_b^\rho \sin\theta_\alpha d\theta_\alpha d\rho \qquad (48)$$

where the source strength is

$$M(\rho,s) = 2U\sqrt{1+a^2\rho^2}\,\frac{\partial f_\tau(\rho,s)}{ds} = 2U\frac{\partial f_\tau(\xi,\rho,\theta_0)}{\partial\xi}$$

the Descartes distance R is

$$[(x-\xi)^2 + r^2 + \rho^2 - 2r\rho\cos(\theta_0 - \phi_0 + \bar{\theta}_n)]^{1/2}$$

s is measured along the chord of the blade section and the other symbols are as defined in section A (see Eq. (29)).

From Bernoulli's equation, the linearized pressure P_τ is

$$P_\tau(x,r,\phi_0) = -\rho_f U\left(\frac{\partial\phi}{\partial x} + a\frac{\partial\phi}{\partial\phi_0}\right)$$

Hence

$$P_\tau(x,r,\phi_0) = \frac{\rho_f U^2}{2\pi a} \sum_{n=1}^{N} \int_0^{\pi} \int_\rho \frac{\partial f_\tau(\xi,\rho,\theta_0)}{\partial\xi} \left[\left(\frac{\partial}{\partial x} + a\frac{\partial}{\partial\phi_0}\right)\frac{1}{R}\right] \theta_b^\rho \sqrt{1+a^2\rho^2}\sin\theta_\alpha d\theta_\alpha d\rho$$

$$(49)$$

29

If use is made of the expansion

$$\frac{1}{R} = \frac{1}{\pi} \sum_{m=-\infty}^{\infty} e^{im(\upsilon_o - \phi_o + \bar{\upsilon}_n)} \int_{-\infty}^{\infty} (IK)_m \, e^{i(x-\xi)k} dk$$

where

$$(IK)_m = \begin{cases} I_m(|k|\rho) K_m(|k|r) & \text{for } \rho < r \\ I_m(|k|r) K_m(|k|\rho) & \text{for } r < \rho \end{cases}$$

then

$$(\frac{\partial}{\partial x} + a \frac{\partial}{\partial \upsilon_o}) \frac{1}{R} = \frac{i}{\pi} \sum_{m=-\infty}^{\infty} e^{im(\upsilon_o - \phi_o + \bar{\theta}_n)} \int_{-\infty}^{\infty} (k-am)(IK)_m \, e^{i(x-\xi)k} dk \quad (50)$$

Since

$$\xi = \theta_o/a = (\sigma^\rho - \theta_b^\rho \cos\theta_\alpha)/a$$

$$\frac{\partial f_\tau(\xi,\rho,\upsilon_o)}{\partial \xi} = \frac{a}{\theta_b^\rho \sin\theta_\alpha} \frac{\partial f_\tau(\rho,\theta_\alpha)}{\partial \theta_\alpha} \quad (51)$$

Also

$$\sum_{n=1}^{N} e^{im\bar{\theta}_n} = \begin{cases} N \text{ for } m = \ell N, \quad \ell = 0, \pm 1, \pm 2 \dots \\ 0 \text{ for } m \neq \ell N \end{cases} \quad (52)$$

On substituting (50) - (52) in Eq. (49), the pressure becomes

$$P_\tau(x,r,\phi_o) = \frac{iN\rho_f U^2}{2\pi^2} \int_o^\pi \int_\rho \frac{\partial f_\tau(\rho,\theta_\alpha)}{\partial \theta_\alpha} \sqrt{1+a^2\rho^2}$$

$$\cdot \sum_{\substack{m=-\infty \\ m=\ell N}}^{\infty} e^{im(\theta_o-\phi_o)} \int_{-\infty}^{\infty} (k-am)(IK)_m e^{i(x-\xi)k} dk d\theta_\alpha d\rho \quad (53)$$

With the trigonometric transformations for θ_o and ϕ_o

$$P_\tau(x,r,\phi_o) = \frac{iN_f U}{2\pi^2} \sum_{\substack{n=\ell l}} \int_o^\pi \int_\rho \frac{\partial f_\tau(\rho,\theta_\alpha)}{\partial \theta_\alpha} \sqrt{1+a^2\rho^2} \, e^{-im\Delta\sigma} \, e^{im(\theta_b^r \cos\phi_\alpha - \theta_b^\rho \cos\theta_\alpha)}$$

$$\cdot \int_{-\infty}^{\infty} (k-am)(IK)_m e^{ik\Delta\sigma/a} e^{-ik(\theta_b^r \cos\phi_\alpha - \theta_b^\rho \cos\theta_\alpha)/a} dk d\theta_\alpha d\rho \quad (54)$$

The υ_α-integral is as before (see Eq. (33) of Section A)

30

$$A((k-am)\theta_b^\rho/a) = \int_0^\pi \frac{\partial f_\tau(\rho,\theta_\alpha)}{\partial \theta_\alpha} e^{i((k-am)\theta_b^\rho/a)\cos\theta_\alpha} d\theta_\alpha \tag{55}$$

which is evaluated in Eq. (35).

As in the case of "non-planar" thickness effects, the thickness distribution can be represented by Eq. (31) and the derivative with respect to θ_α by Eq. (32). After substituting (55) and folding the m-series to $m = 0$ to $+\infty$, the pressure of Eq. (54) is brought to

$$P_\tau(x,r,\phi_o) = \frac{iN\rho_f U^2}{2\pi^2} \int_\rho \sqrt{1+a^2\rho^2}$$

$$\cdot \{ \int_{-\infty}^\infty A(k\theta_b/a)k(IK)_o e^{ik(\Delta\sigma-\theta_b^r\cos\phi_\alpha)/a} dk$$

$$+ \sum_{m=N,2N}^M \int_{-\infty}^\infty (IK)_m [A((k-am)\theta_b^\rho/a)(k-am)e^{i(k-am)(\Delta\sigma-\theta_b^r\cos\phi_\alpha)/a}$$

$$+ A((k+am)\theta_b^\rho/a)(k+am)e^{i(k+am)(\Delta\sigma-\theta_b^r\cos\phi_\alpha)/a}]dk\}d\rho \tag{56}$$

Let $k - am = u$ in the first term and $k + am = u$ in the second term of the second k-integral. Then this integral can be written (for $\rho < r$) as

$$\sum_{m=N,2N}^M \int_{-\infty}^\infty [A(u\theta_b^\rho/a)ue^{iu(\Delta\sigma-\theta_b^r\cos\phi_\alpha)/a}]$$

$$\cdot [I_m(|u+am|\rho)K_m(|u+am|r) + I_m(|u-am|\rho)K_m(|n-am|r)]du$$

$$= \sum_{m=N,2N}^M 2i \int_0^\infty \{\text{ImPart}[A(u\theta_b^\rho/a)e^{iu(\Delta\sigma-\theta_b^r\cos\phi_\alpha)/a}]\}$$

$$\cdot u [I_m(|u+am|\rho)K_m(|u+am|r) + I_m(|u-am|\rho)K_m(|u-am|r)]du$$

and Eq. (52) becomes finally

$$P_\tau(x,r,\phi_o) = \frac{-N\rho_f U^2}{\pi^2} \int_\rho \sqrt{1+a^2\rho^2}$$

$$\cdot \int_0^\infty \text{ImPart}[A(u\theta_b^\rho/a)e^{iu(\Delta\sigma-\theta_b^r\cos\phi_\alpha)/a}]$$

$$\cdot u \{I_o(u\rho)K_o(ur) + \sum_{m=N,2N}^M [I_m(u+am|\rho)K_m(|u+am|r)$$

$$+ I_m(|u-am|\rho)K_m(|u-am|r)]\}dud\rho \tag{57}$$

for $\rho < r$. (If $\rho > r$, ρ and r are interchanged in the modified Bessel functions. Note that a,ρ,r,u are non-dimensionalized by propeller radius r_o.)

It can be proved that the integrand is zero when $u = 0$. When $\rho \to r$, the ρ-integral has a logarithmic singularity. (This is shown in Appendix D). Although a logarithmic singularity is integrable, nevertheless, since the integration is performed numerically rather than analytically, special precautions must be taken in evaluating the integrand in the region of the singularity. The procedure is described in Appendix E.

C. *Blade Pressure Distributions Due to Loading and Thickness Effects on Each Blade Face*

The total pressure distribution on each blade face is a superposition of the pressure P_T due to the thickness effect which produces no lift, on the pressures arising from the effects of "non-planar" thickness, camber and angle of attack of the blade and of spatial nonuniformity of the inflow field. The last four components contribute to the lift because each produces a pressure difference ΔP between the back and front faces of the blade surface. On the suction side (back face) the pressure due to the loading contributors is $\Delta P/2$; on the pressure side (front face) the pressure is $-\Delta P/2$.

Since the blade is considered to be rigid, the non-lifting thickness effect will be present only in the steady state. In this case ($q = 0$) the blade pressure distribution is made up as follows:

a) On the pressure side

$$P_p^{(o)} = -\left(\frac{\Delta P}{2}\right)_w^{(o)} - \left(\frac{\Delta P}{2}\right)_c - \left(\frac{\Delta P}{2}\right)_f - \left(\frac{\Delta P}{2}\right)_{npt} + P_T \qquad (58)$$

b) On the suction side

$$P_s^{(o)} = \left(\frac{\Delta P}{2}\right)_w^{(o)} + \left(\frac{\Delta P}{2}\right)_c + \left(\frac{\Delta P}{2}\right)_f + \left(\frac{\Delta P}{2}\right)_{npt} + P_T \qquad (59)$$

where the subscripts, w, c, f and npt refer to wake, camber, flow angle, and "non-planar" thickness, respectively.

For the unsteady flow case, $q \neq 0$

a) $P_p^{(q)} = -(\frac{\Delta p}{2})_w^{(q)}$ (60)

b) $P_s^{(q)} = (\frac{\Delta p}{2})_w^{(q)}$ (61)

Having determined the pressure distribution on each side of the blade for all frequencies contributing significantly, the instantaneous pressure, which is the sum of the blade pressures due to all frequencies, can be evaluated as the blade swings around its shaft (see the following section D). The instantaneous pressure on the front (pressure) or back (suction) face at a given radial position r is, when the propeller swings around its shaft in the clockwise direction from its upright position (at 12 o'clock):

$$P_{p,s}(r) = \text{Re} \sum_{q=0} P_{p,s}^{(q)}(r)\ e^{-iq\theta} = \sum_{q=0} |P_{p,s}^{(q)}(r)| \cos(q\theta - \phi_q)$$ (62)

where

$$\phi_q = \text{phase angle} = \tan^{-1} \frac{(P_{p,s}^{(q)})_{\text{Im}}}{(P_{p,s}^{(q)})_{\text{Re}}}$$

and the subscripts Re and Im indicate the real and imaginary parts of $P_{p,s}^{(q)}(r)$. (θ and φ_q are negative in the clockwise direction.)

D. *Information Relative to Blade Stress Analysis and Cavitation Study*

Having determined a realistic blade hydrodynamic loading at all frequencies of importance for a propeller operating in non-uniform inflow, taking into account the exact geometry (skewed or unskewed blade on a helicoidal surface) and the mutual interaction of the blades, both the structural analysis of the blade (displacement and state of stress) and the cavitation study can now be undertaken.

A stress analysis based on the finite element approach and the corresponding program adaptable to high-speed digital computers, both developed by Mechanics Research, Inc., are now available at CDC computer centers world-wide. Designated as STARDYNE, this program has been used extensively for static and dynamic structural analysis.

Experience at Davidson Laboratory[9] with this program for the structural analysis of a propeller blade has suggested the format of the output of the DL program for blade loading distributions to suit the required input to the STARDYNE program. The DL program provides the mean and time-dependent blade loadings at all significant shaft frequencies at 19 points along the chords of eight radial strips. The program can be easily changed to evaluate the chordwise pressures at a greater number of points. However, since the number of radial strips governs the size of the kernel matrix, a finer mesh in the radial direction will be more easily achieved by interpolation of the values between adjacent radial strips.

The instantaneous blade loading, which is the sum of the loadings due to all frequencies with proper phasing, is applied as an input to the static STARDYNE program. The angular interval between successive blade positions can be refined, depending on the type of wake. In the case of a container ship with sharp wake peaks at 12 and 6 o'clock, a finer spatial mesh is required and a small angular interval, such as 10 degrees, is advisable during the complete revolution of a blade.

The blade pressure-jump distributions due to loading at each shaft frequency can be extracted from the output of the main program and recorded on a magnetic tape to be used in an auxiliary program to evaluate the instantaneous pressure jumps in a format required by the STARDYNE program.

Another feature of the DL program provides information for prediction of cavitation inception. The blade pressures due to loading and thickness effects on suction (back) and pressure (face) sides of the blade which have been calculated at all significant shaft frequencies will be similarly extracted from the general program and recorded on another magnetic tape. Another auxiliary program will use this tape for the evaluation of the instantaneous pressure coefficients,

$$C_p = \frac{P}{\frac{1}{2} \rho_f U^2 (1 + a^2 r^2)} \tag{63}$$

on suction and pressure sides of the blade separately as the blade swings around its shaft (see Eq. (62)). These values must be scanned to determine

34

the minimum pressure coefficient for use in predicting the locations for cavitation inception.

Also extracted from the general program and recorded on magnetic tape, for possible future use, are the loading solutions $L^{(q,\bar{n})}(r)$ for all shaft frequencies q and mode shapes $\bar{n}$ at the various radial positions r.

II. NUMERICAL RESULTS

The theoretical procedures developed in the preceding sections to determine the blade pressure distributions due to loading and thickness effects have been adapted to a high-speed digital computer (CDC 6600 or 7600). The computer program provides the resulting hydrodynamic forces and moments and blade bending moments as well as the blade pressure distributions on each blade face in steady and unsteady flow conditions. As noted, the unrealistic leading edge singularity introduced in the blade chordwise pressure distribution by the cotangent term of the Birnbaum distribution is removed by the Van Dyke-Lighthill correction method. In addition, the frictional contribution to steady-state thrust and torque has been approximated by using the Prandtl-Schlichting formula for the friction coefficient, without taking into account the viscous pressure drag or the drag associated with the deviation of the local flow direction from that along the nose-tail line.

A set of calculations has been performed for the series of 3-bladed propellers of expanded area ratio EAR = 0.3, 0.6 and 1.2 which had been studied in Reference 3 under the assumption of zero thickness, and for which experimental data were available from controlled NSRDC tests[15,16,17] in nonuniform inflow with wake structure rigidly specified (screen wake). The propellers, with destroyer-type blade outlines and modified NACA-66 section with a = 0.8 mean line, were one foot in diameter with hub diameter 0.2 feet and pitch ratio 1.08 at 0.7 radius. Relevant geometric characteristics of this set of 3-bladed propellers are given in the tables below. The ratios of maximum camber to chord length are given in Table I, of maximum thickness to chord length in Table II and of leading edge radius to chord in Table III.

TABLE I

Ratio of Maximum Camber to Chord, m_x/c

Radius	EAR = 0.3	EAR = 0.6	EAR = 1.2
.25	.0370	.0228	.0196
.35	.0388	.0231	.0202
.45	.0372	.0224	.0196
.55	.0340	.0212	.0185
.65	.0312	.0203	.0177
.75	.0290	.0198	.0170
.85	.0270	.0189	.0160
.95	.0247	.0174	.0147

TABLE II

Ratio of Maximum Thickness to Chord, τ_o/c

Radius	EAR = 0.3	EAR = 0.6	EAR = 1.2
.25	.253	.090	.032
.35	.192	.068	.024
.45	.146	.052	.018
.55	.113	.040	.014
.65	.087	.031	.011
.75	.068	.024	.0086
.85	.052	.018	.0066
.95	.045	.016	.0057

TABLE III

Ratio of Leading-edge Radius to Chord, ρ_o

Radius	EAR = 0.3	EAR = 0.6	EAR = 1.2
.25	.0410	.00525	.00066
.35	.0236	.00290	.00039
.45	.0136	.00170	.00021
.55	.00817	.00100	.00013
.65	.00484	.00060	.00008
.75	.00296	.00035	.00005
.85	.00173	.00025	.00003
.95	.00133	.00020	.00002

The coefficients $a_n(\rho)$ in the thickness distribution given by Eq. (31) are presented in Table IV for all three propellers and all radial positions. The thickness distribution variations with EAR and radial position are determined through the τ_o/c, ρ_o and θ_b factors of Eq. (31). (Note that the procedure for calculating $a_n(\rho)$ is given on page 18.)

TABLE IV

Coefficients $a_n(\rho)$

n	$a_n(\rho)$
1	0.5491
2	-0.1165
3	0
4	0

The tests had been conducted in the NSRDC 24-inch water tunnel using the closed-jet test section with a screen to produce the wake, a

37

3-cycle screen for the force along and moment about the longitudinal axis and a 4-cycle screen for the forces along and moments about the transverse and vertical axes. The tests were run at a constant speed of 15 rps with free stream velocity close to 12.5 ft/sec. The design mean thrust coefficient $\bar{K}_T$ was 0.150 (practically open-water value in the 3-cycle screen wake), the advance ratio varying slightly from propeller to propeller[17]. Wake information is given in Table V for 3- and 4-cycle screen wakes. Note that the Fourier coefficients a_q, b_q, A_q and B_q of Eq. (23)f can be easily determined from the information given in this table.

TABLE V
Wake Information from Harmonic Analysis
of 3-Cycle and 4-Cycle Screen Wakes (Reference (16))

Radius	3-Cycle Wake C_3	ϕ_3	4-Cycle Wake C_4	ϕ_4
0.2	0.089	18°	0.050	0
0.3	0.186	10°	0.134	0
0.4	0.220	6°	0.170	0
0.5	0.218	2°	0.184	0
0.6	0.203	0	0.192	0
0.7	0.212	0	0.208	0
0.8	0.230	0	0.224	0
0.9	0.252	0	0.235	0
0.95	0.251	0	0.243	0

Longitudinal Velocity $V_x/U = C_q \sin(q\Omega t + \phi_q) = C_q \sin(-q\theta + \phi_q)$
Tangential Velocity $V_T/U = 0$

The computations were run for a series of advance ratio in the steady-state case, design J and J = 0.7, 0.6 and 0.5, and at design J in the unsteady cases. The values of design J were 0.841, 0.831 and 0.844 for EAR = 0.3, 0.6 and 1.2, respectively.

The calculated mean thrust and torque coefficients at design J which include the effects of mean wake, camber, flow angle and nonplanar thickness on the loading and, in addition, the frictional thrust and torque, are compared with experimental data[17] in Figure 4. Calculated results are also shown without the frictional part.

38

Figure 5 exhibits the steady-state chordwise pressure distribution at one radial position, $0.65r_o$, on the suction and pressure sides of the blades for all three propellers, at design J. These were obtained from Eqs. (58) and (59), for the pressure and suction sides respectively.

Figures 6 and 7 compare the calculated blade-frequency thrust and torque coefficients and phases with the experimental data of Reference 16 using the blade-frequency (third) harmonics of the screen wake given in Table V. The earlier calculations of Refs. 15 and 3 were based on wake measurements reported by DTNSRDC which were taken with the screen open sections at a different position. In Figure 6, the phases (electrical) are given in accordance with the Davidson Laboratory definition on page 25 of this report. Figure 7 shows the mechanical phases according to Reference 16 and to Davidson Laboratory.

Figures 8 and 9 present comparisons of calculated and experimental blade-frequency transverse forces and moments of the three propellers at design J. The calculations use the harmonics given in Table V for the 4-cycle screen wake in which the tests were conducted[16].

Figures 10, 11 and 12 show the blade-frequency chordwise pressure distributions at $0.65r_o$ for the three propellers calculated as in Eqs. (60) and (61). The leading-edge singularity has been removed by the Van Dyke-Lighthill correction method (see Eq. (40)).

Calculations have also been conducted for off-design J = 0.5, 0.6 and 0.7 for uniform inflows. Figures 13, 14 and 15 compare the chordwise pressure distributions at one radial location, $0.65r_o$ for the three propellers at design J and J = 0.5 and 0.7. These blade pressure distributions agree qualitatively with experiments of Mavlyudov[18] (USSR). No other experimental information is available for comparison.

Having evaluated the pressure distributions in the design and off-design flow conditions, it is possible, in principle, to determine the cavitation inception of an operating propeller. Cavitation is assumed to ensue when the local pressure falls to the value of the vapor pressure in the fluid. The speed $V_i(r)$ of cavitation inception is known to be given by

39

$$\frac{V_i(r)}{V(r)} = \frac{\sigma}{|C_{p_m}|}$$

where $V(r) = U\sqrt{1 + a^2 r^2}$ = resultant velocity at a blade section at radial location r

σ = cavitation number or cavitation index

= (total pressure - vapor pressure)$/(\frac{1}{2}\rho_f V^2)$

and C_{p_m} = minimum pressure coefficient, $p_m/(\frac{1}{2}\rho_f V^2)$ (i.e., where C_p is most negative)

Cavitation is assumed not to occur when $\sigma > -C_{p_m}$, but will persist as long as $\sigma < -C_{p_m}$, the critical cavitation index being when $V_i/V = 1.0$ or $\sigma_i = |C_{p_m}|$.

The critical cavitation indices have been evaluated as the absolute values of the most negative pressure coefficients established by the theoretical steady-state blade pressure distribution curves. They are plotted in Figures 16, 17 and 18 for various advance ratios versus radial position and compared there with the experimental observations reported in Reference 17 for the same set of 3-bladed propellers operating in open water conditions. Since the experimental cavitation indices[17] were based on speed of advance rather than resultant velocity, the theoretical pressure coefficients have also been evaluated on that base $(C_{p_m} = p_m/(\frac{1}{2}\rho_f U^2)$.

Although no experimental values of σ_i for design J are given in Reference 17, the theoretical values shown in Figs. 16-18 for design J are justified by the experimental trends (i.e., extrapolation) in that vicinity. At off-design J, the theoretical predictions are sometimes conservative, sometimes non-conservative depending on ΔJ, EAR and radial location.

Since inception speed is inversely proportional to the square root of the minimum pressure coefficient, $\sigma_i = |C_{p_m}|$, whenever the index of inception of cavitation σ_i of the experiment is greater than σ_i of the theoretical calculation, i.e.

$\sigma_i(\text{exp}) > \sigma_i(\text{calc.})$

then U_i(exp.) $<$ U_i(calc.). This case indicates that the experiments
show that cavitation inception is at a lower speed than that predicted
by the theoretical calculations and thus the prediction is non-conservative.
On the other hand, when

$$\sigma_i(\text{exp}) < \sigma_i(\text{calc.})$$

or U_i(exp) $>$ U_i(calc.), the predicted values for cavitation inception
are conservative.

Figure 16, which is a comparison of calculated and experimentally
observed cavitation index for the 3-bladed propeller 4132 (EAR = 0.3),
shows conservative predictions when J = 0.7 or design J, whereas the
predictions are non-conservative, somewhat at J = 0.6 and especially so
at J = 0.5, except near the hub and near the tip. In Figures 17 and 18,
for the 3-bladed propellers 4118 (EAR = 0.6) and 4133 (EAR = 1.2), respec-
tively, all predictions are on the conservative side except those for J = 0.5.

Judging from this set of calculations, the predicted values of
cavitation inception are on the conservative side compared with experi-
mental observations as long as $\Delta J = J_d - J_{od} < 0.3$. Nevertheless, the
discrepancies which exist between predicted values of the index of cavita-
tion inception and the experimental observations require investigation.

These observed discrepancies must not be solely attributed to the
lack of accuracy of the linearized theory when modified by the Van Dyke
correction. It is well known that visual determination of inception of
cavitation is dependent upon the subjective evaluation of the observer
and is highly dependent on the surface finish and accuracy of the model
in the immediate vicinity of the leading edge of the blades. The variant
patterns of the viscous flow at appreciable angles of attack can involve
laminar separation with vortical flow standing off the blade surface
giving extremely low pressures in the core of the vortex (as cited fre-
quently by Eisenberg, for example) and, hence, inception at σ values
larger than the minimum pressure coefficient provided by inviscid theory
on the surface of the blade. Also, from the definitive measurements of
Huang and Hannan[19], it can be conjectured that large pressure fluctuations
can occur on the blade surface at the reattachment zone abaft laminar
separation. In addition, it is never certain that observed inception
is attributed to truly vaporous cavitation or to the expansion of un-
dissolved air.

41

The fact that the experimental σ-values are generally higher than the calculated $|C_{p_m}|$ at the maximum excursion in J (i.e., J = 0.5, ΔJ = 0.33) suggests that the real fluid effects alluded to above may be responsible. However, at the larger J = 0.7 (smaller ΔJ = 0.13), the disagreement is in the opposite direction except for the first propeller, EAR = 0.30, where the agreement is fine. Here the fluid speeds are of the order of twice as great as at J = 0.5 and the pressure peaks on the blades at reduced angle of attack, while lower in magnitude, are indeed sharper, i.e., the chordwise width of the pressure spike is reduced. One may speculate that the passage time of nuclei through the region of low pressure is considerably less at J = 0.7 than at J = 0.5 (higher speed, shorter extent) and that cavitation does not ensue until the σ values are dropped below the $|C_{p_m}|$.

The validity of the theoretical curves should be checked by employing a rational method for finding the effective angle of attack, the effective camber and the effective thickness of the two-dimensional section (to be substituted for each blade section) for which exact steady-state pressure distributions have been computed. This is not a simple process as was discovered when attempting to use the families of curves provided by Brockett[20] and a rule for finding the effective angle of attack attributed to W. Morgan. The effective angle of attack was found to be too imprecise; a very small error produces a larger error in the C_{p_m} value.

Clearly, further studies of the pressure distribution at the leading edge of propellers are necessary. The results obtained thus far should be regarded as quite reasonable. Further work may require a precise mechanization of the effective two-dimensional solutions using certain inputs from the three-dimensional propeller flow field, and local sectional loadings.

CONCLUSION

In this study, a theoretical approach is evolved and a computational procedure adaptable to a high-speed digital computer (CDC 6600 and 7600) is developed for evaluation of the linearized pressure distribution on each side of a marine propeller blade, with the objective to obtain sufficient and reliable information for cavitation and blade stress analyses.

The essential information for the blade stress analysis is the anti-symmetric part of the blade pressure distribution, attributed to the non-uniform inflow (wake), blade camber, incident flow angle and nonplanar thickness of the blade, all of which are associated with the lifting action of the blade and contribute to the hydrodynamic forces and moments and blade bending moments. The symmetric part of the blade pressure distribution, attributed to the planar thickness and associated with the non-lifting properties of the blade, contributes to the pressure distribution on each side of the blade, which is essential for the prediction of cavitation inception.

In addition to the blade pressure distributions at each frequency, the program furnishes the propeller-generated steady-state and time-dependent hydrodynamic forces and moments and the blade bending moment about the face-pitch line at the midpoint of any of the radial strips into which the span is divided. The program also provides the instantaneous blade pressure due to loading alone and the instantaneous pressures on suction and pressure sides, as well as the instantaneous blade bending moments, as the propeller swings around its shaft. The thrust and torque due to friction is estimated by using an approximate frictional drag coefficient; in the event of any improvement of the estimated frictional coefficient, this portion of the program can be easily modified.

In applying the mode approach to the solution of the surface integral equation, the analysis and the program are divided into two main parts, one dealing with the steady-state flow case ($q = 0$) and the other with the unsteady flow condition. The steady-state case is subdivided into design and off-design conditions. The selection of the proper chordwise modes in the steady-state flow condition at design advance ratio J is dictated by the shape of the loading distribution in two-dimensional flow on a foil with the same camber distribution. At off-design J in the steady-

43

state condition, there is an angle of attack due to the difference ΔJ (between design and off-design advance ratio) and the additional loading due to this angle of attack is represented by the cotangent term of the Birnbaum modes. In the unsteady flow condition, the complete Birnbaum modes are used.

The linearized unsteady lifting-surface theory requires the leading-edge singularity arising from the cotangent term of the Birnbaum modes. The "square-root" singularity is integrable, but its presence in the blade pressure distributions is unrealistic and has been removed by employing the Van Dyke-Lighthill correction factor.

A set of computations has been performed for the series of 3-bladed propellers for which experimental data were available from NSRDC tests in open water and in the non-uniform inflows due to 3-cycle and 4-cycle screen wakes. The calculated results for the hydrodynamic forces and moments, steady and unsteady, compare well with the experimental values. There is no experimental information on blade pressure distributions for this set of propellers. However, the blade pressure distribution curves in the steady-state case agree qualitatively with experimental curves[18] shown by Mavlyudov (USSR) for a different propeller model (NACA-16, $\bar{a} = 0.8$ mean line section, EAR = 0.95) at 0.8 radius. In the absence of experimentally measured blade pressure distributions for the propellers treated, a comparison is made indirectly through the index of cavitation inception in uniform inflow. It is seen that the predicted values of $\sigma_i = \left| C_{p_m} \right|$ are conservative except at the smallest off-design J = 0.5 (largest $\Delta J = 0.33$).

The cavitation index $\left| C_{p_m} \right|$ reflects the blade pressure in the neighborhood of the leading edge and this is dependent on the correction method for removing the leading edge singularity of the theoretical distribution. However, the observed discrepancies between theory and experiment cannot be attributed solely to the lack of accuracy of the linearized theory when modified by the Van Dyke correction. Experimental determination of the inception of cavitation is dependent on the subjective evaluation of the observer. It is also dependent on the surface finish and accuracy of the propeller model in the immediate vicinity of the leading edge of the blades and on the undissolved air content of the fluid as well. There is a

possibility that flow separation and vortex generation occur near the leading edge and this is not taken into account by the theory. Further studies, both theoretical and experimental, are necessary. The results obtained thus far may be considered reasonable.

REFERENCES

1. W. R. Jacobs and S. Tsakonas, "Generalized Lift Operator Technique
    for the Solution of the Downwash Integral Equation," DL Report 1308,
    Stevens Institute of Technology, August 1968; published as A New
    Procedure for the Solution of Lifting Surface Problems," J. Hydronautics
    Vol. 3, No. 1, January 1969.

2. S. Tsakonas, W. R. Jacobs and P. H. Rank, Jr., "Unsteady Propeller
    Lifting Surface Theory with Finite Number of Chordwise Modes," DL
    Report 1133, Stevens Institute of Technology, December 1966; J. Ship
    Research, Vol. 12, No. 1, March 1968.

3. S. Tsakonas, W. R. Jacobs and M. R. Ali, "An Exact Linear Lifting-
    Surface Theory for a Marine Propeller in a Nonuniform Flow Field,"
    DL Report 1509, Stevens Institute of Technology, February 1972
    J. Ship Research Vol. 17, No. 4, December 1973.

4. M. D. Van Dyke, "Second-Order Subsonic Airfoil Theory Including
    Edge Effects," NACA Report 1274, 1956.

5. M. J. Lighthill, "A New Approach to Thin Aerofoil Theory," Aero.
    Quart., Vol. 3, pt 3, November 1951.

6. S. Tsakonas and W. R. Jacobs, "Propeller Loading Distributions,"
    DL Report 1319, Stevens Institute of Technology, August 1968;
    J. Ship Research Vol. 13, No. 4, December 1969.

7. I. H. Abbott and A. E. Von Doenhoff, Theory of Wing Sections ,
    Dover Publications, Inc., New York, 1959.

8. S. F. Hoerner, Fluid-Dynamic Drag, published by the author, 1965.

9. S. Tsakonas and W. R. Jacobs, "Steady and Time-Dependent Propeller
    Blade Loading and Stress Analysis," Propellers 75 Symposium, Society
    of Naval Architects and Marine Engineers, July 1975.

10. S. Tsakonas, C. Y. Chen and W. R. Jacobs, "Exact Treatment of the
    Helicoidal Wake in the Propeller Lifting-Surface Theory," DL Report
    1117, Stevens Institute of Technology, August 1966; J. Ship Research
    Vol. 11, No. 3, September 1967.

11. J. W. Nicholson, "The Approximate Calculations of Bessel Functions
    of Imaginary Argument," Phil. Mag., Series 6, Vol. 20, December 1910.

12. L. B. W. Jolley, ed., Summation of Series, Dover Publications, Inc., New York, 1961.

13. J. B. Scarborough, Numerical Mathematical Analysis, The Johns Hopkins Press, Baltimore, Md., 1958.

14. C. E. Watkins, D. S. Woolston and H. J. Cunningham, "A Systematic Kernel Function Procedure for Determining Aerodynamic Forces on Oscillating or Steady Finite Wings at Subsonic Speeds," NASA Technical Report R-48, 1959.

15. S. Tsakonas, J.P. Breslin and M. Miller, "Correlation and Application of an Unsteady Flow Theory for Propeller Forces," Trans. SNAME, Vol.75, 1967.

16. M.L. Miller, "Experimental Determination of Unsteady Propeller Forces," Seventh ONR Symposium on Naval Hydrodynamics, August 1968, pp.255-290.

17. S.B. Denny, "Cavitation and Open Water Performance Tests of a Series of Propellers Designed by Lifting Surface Methods," NSRDC Report 2878, September 1968.

18. M.A. Mavlyudov, "Measurement of Pressure Distribution on the Blades of a Marine Propeller Model," Sbornik Statey po Gidrodinamike Dvirhiteley, "Sudostroyaniye" Publishing House, 1965, pp. 67-72.

19. T.T. Huang and D.E. Hannan, "Pressure Fluctuations in the Regions of Flow Transition," DTNSRDC Report 4723, December 1975.

20. T. Brockett, "Minimum Pressure Envelopes for Modified NACA-66 Sections with NACA a = 0.8 Camber and Buships Type I and Type II Sections," DTMB Report 1780, February 1966.
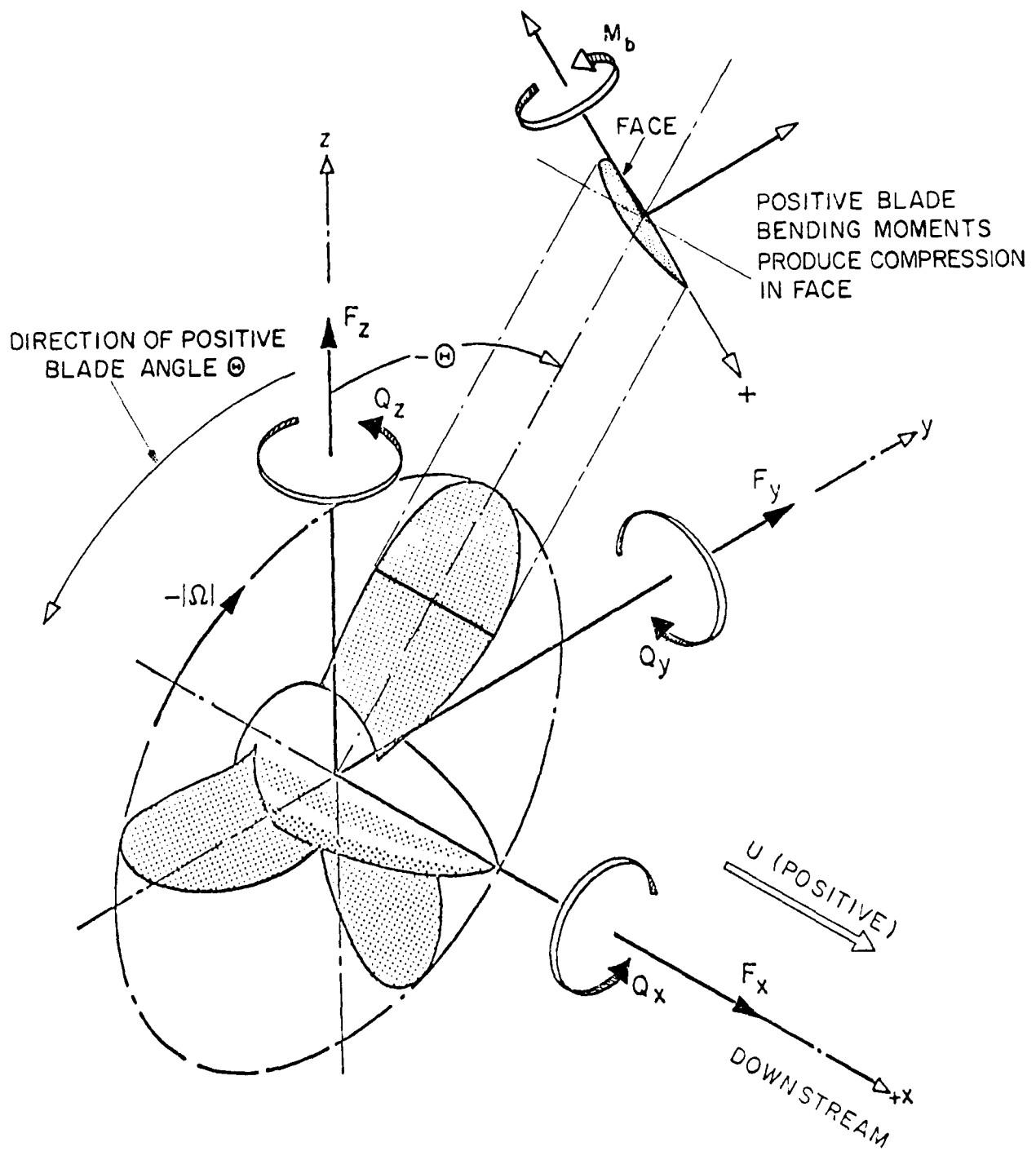
FIG. I   RESOLUTION OF FORCES AND MOMENTS
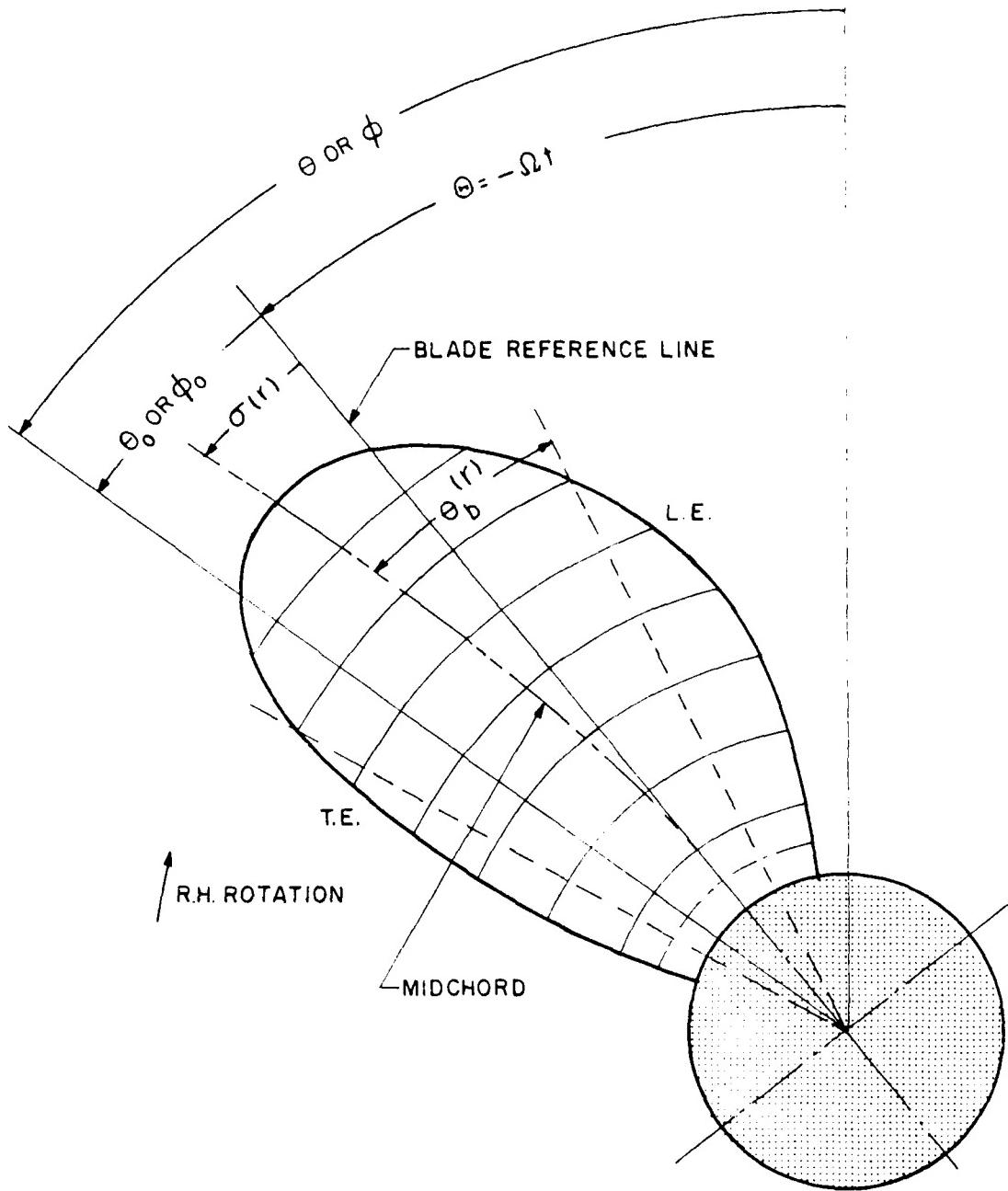
FIG.2.   DEFINITIONS OF ANGULAR MEASURES

NOTE: THE BLADE REFERENCE LINE IS THAT CONNECTING THE SHAFT CENTER WITH
THE MIDPOINT OF THE CHORD AT THE HUB
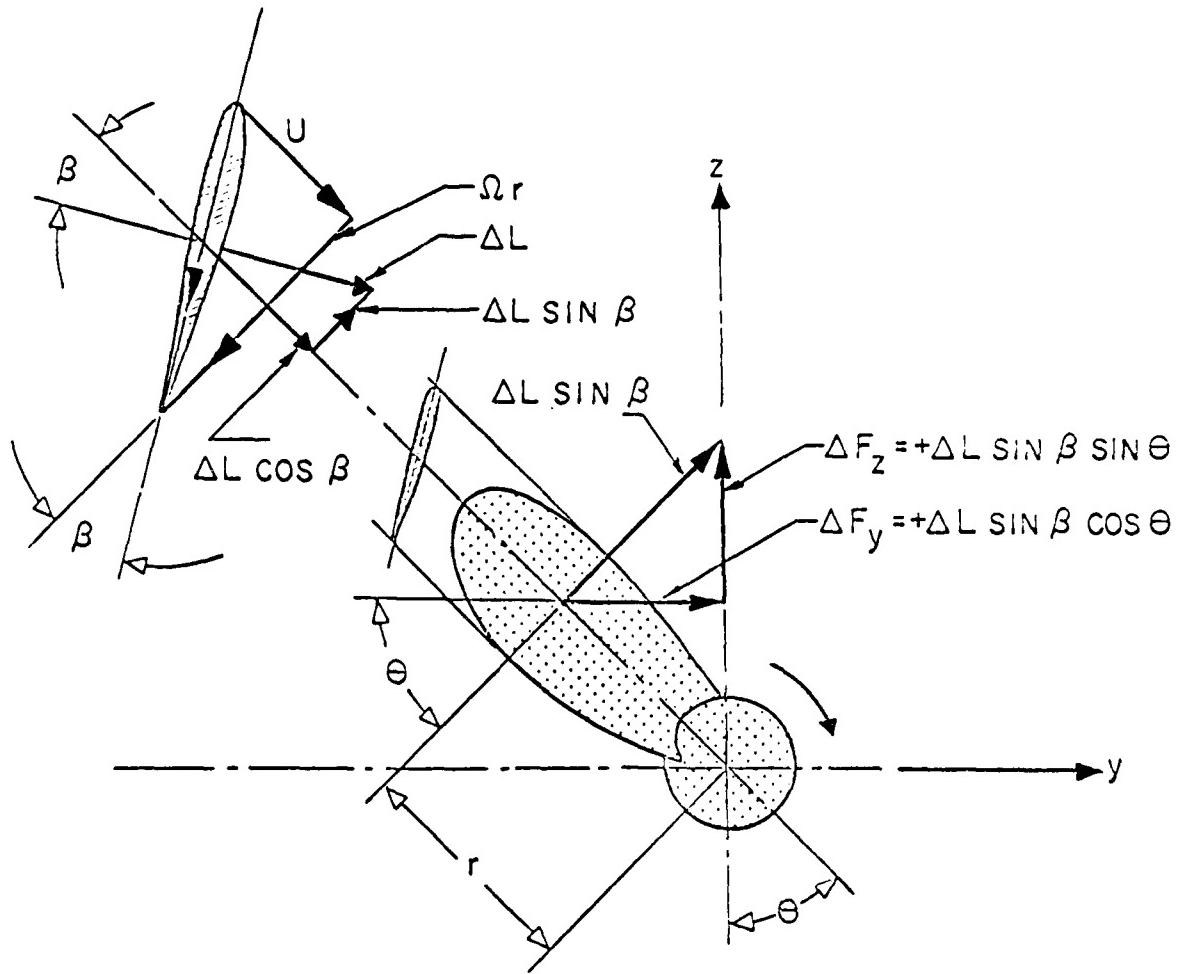
FIG. 3 RESOLUTION OF FORCES

FIG.4. MEAN THRUST AND TORQUE OF DTNSRDC 3-BLADED PROPELLERS AT DESIGN J

DESIGN J

$$C_P = P / \frac{\rho_f}{2} U^2 (1 + a^2 r^2)$$

PRESSURE SIDE

L.E.

T.E.

EAR=1.2

EAR=0.6

EAR=0.3

SUCTION SIDE
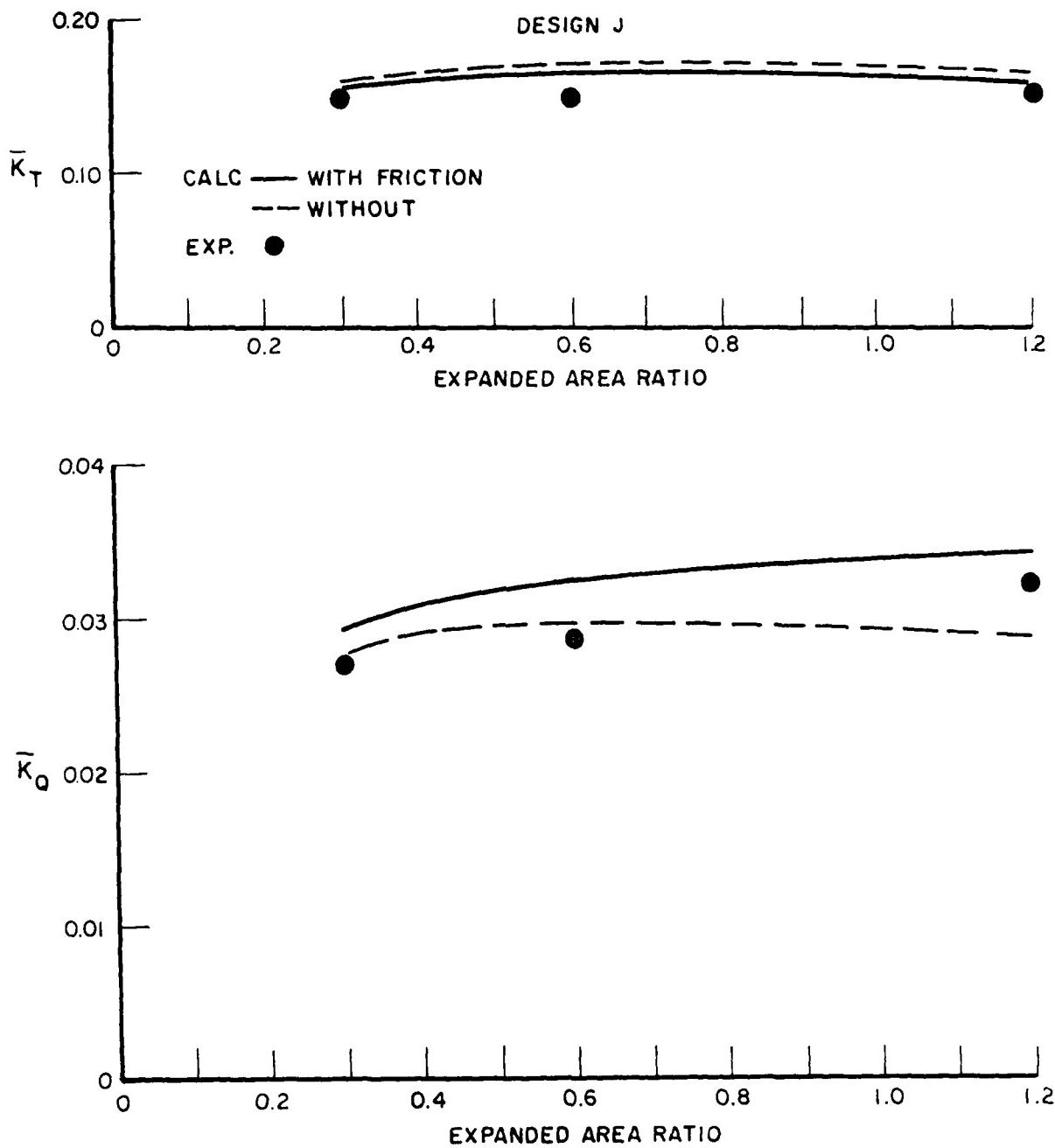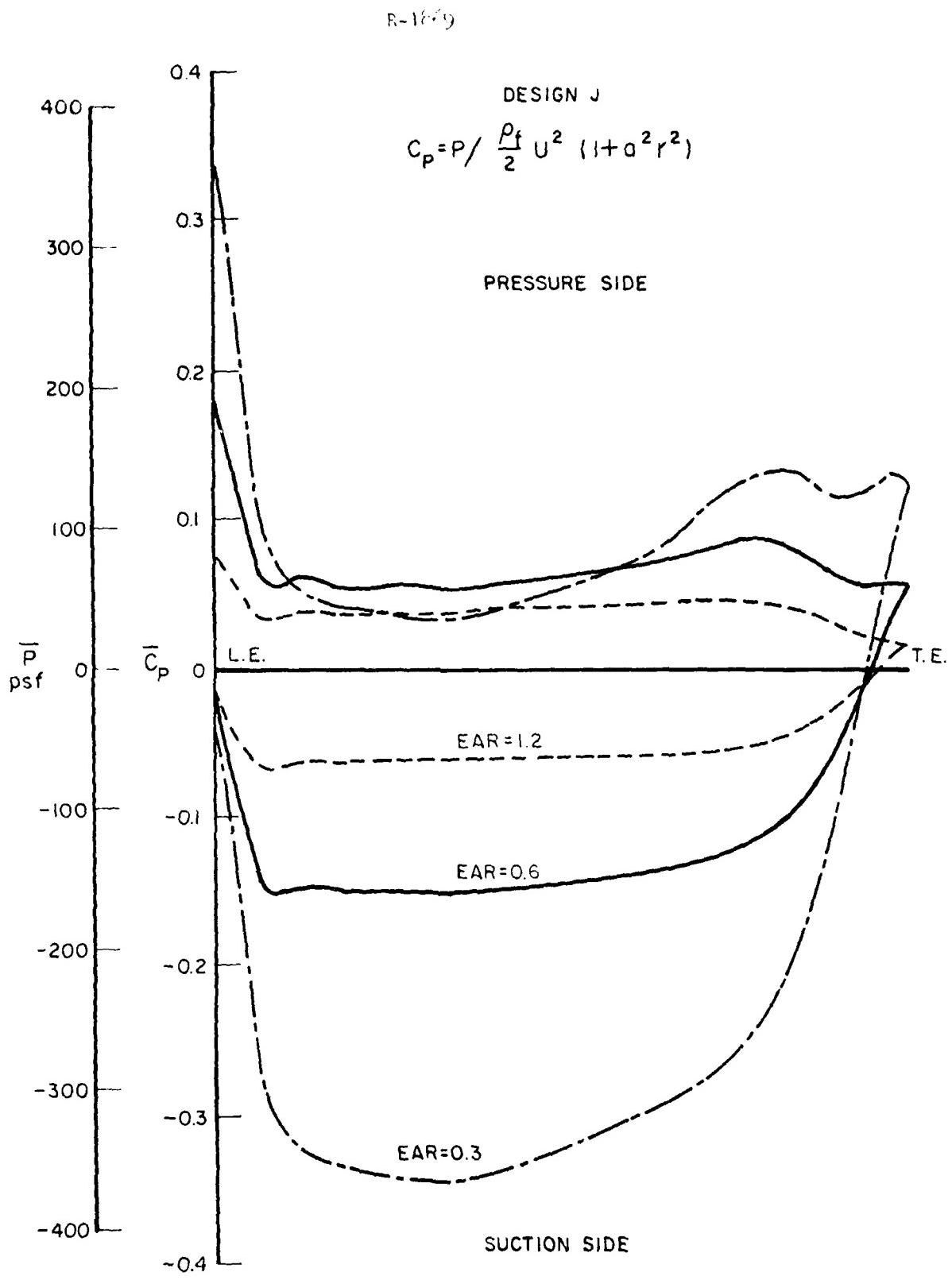
FIG. 5.   STEADY-STATE CHORDWISE PRESSURE DISTRIBUTION AT 0.65
RADIUS ON DTNSRDC 3-BLADED PROPELLERS AT DESIGN J.
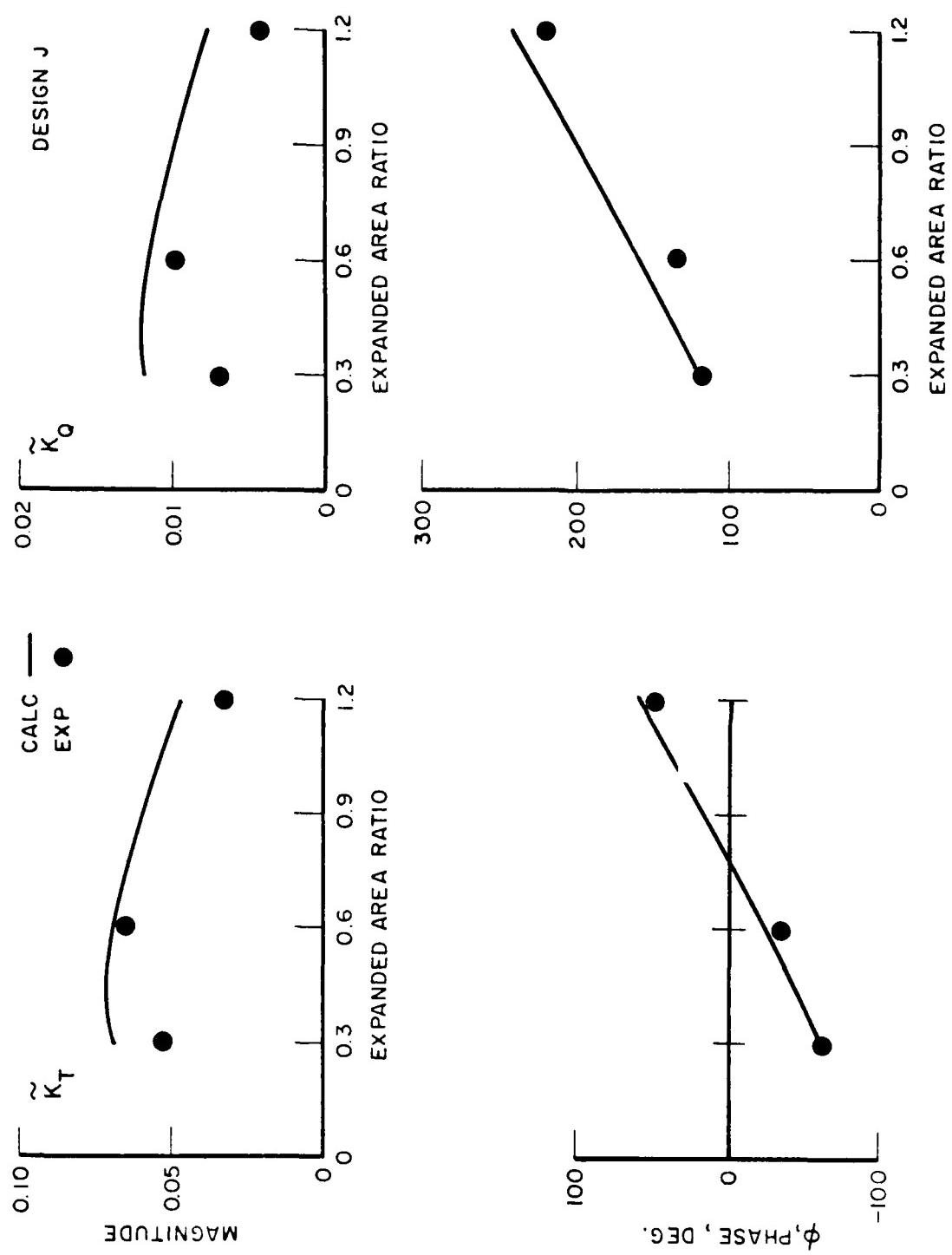
FIG. 6.   BLADE-FREQUENCY THRUST AND TORQUE OF DTNSRDC 3-BLADED PROPELLERS
(IN 3-CYCLE SCREEN WAKE)

FOR DL PHASE DEFINITION SEE FIG. 7. (WHERE $\phi/3$ IS SHOWN FOR EAR=0.6)
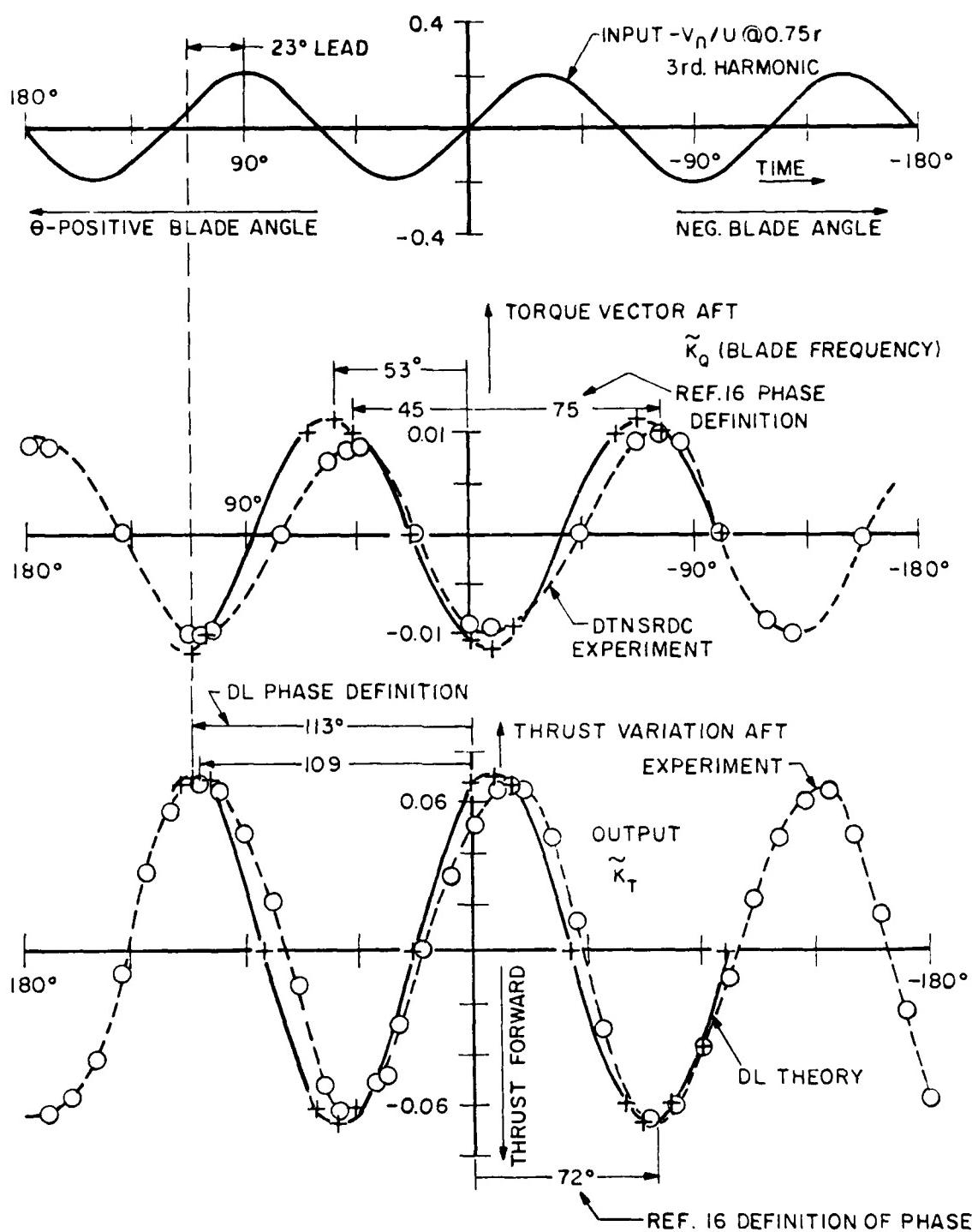
FIG. 7. MEASURED AND CALCULATED BLADE FREQUENCY THRUST AND TORQUE COEFFICIENTS FOR DTNSRDC PROPELLER 4118, EAR=0.6, USING WAKE VALUES OF TABLE V FROM 3-CYCLE SCREEN
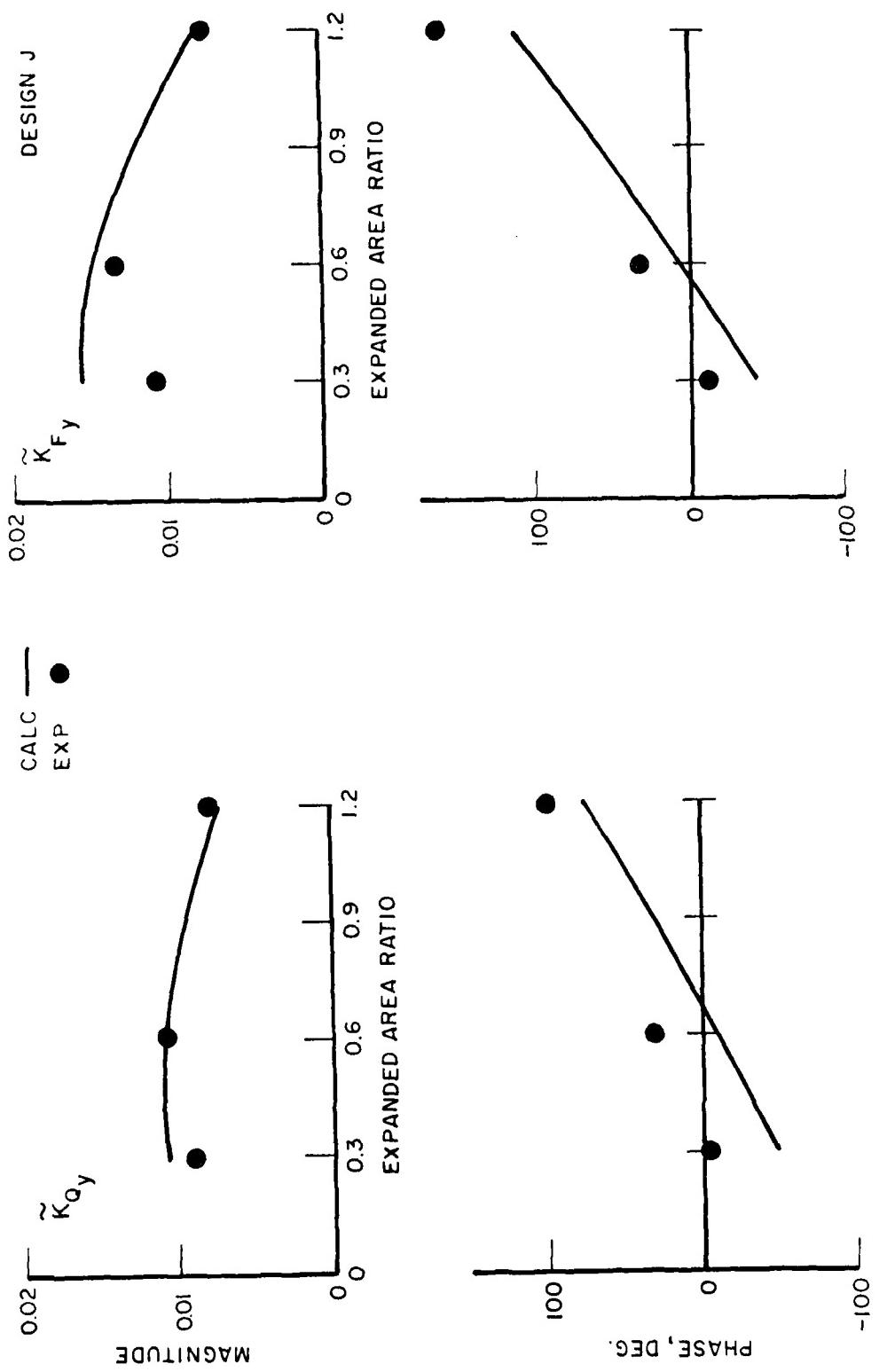
FIG. 8. BLADE-FREQUENCY TRANSVERSE FORCES AND MOMENTS OF DTNSRDC 3-BLADED PROPELLERS (IN 4-CYCLE SCREEN WAKE)
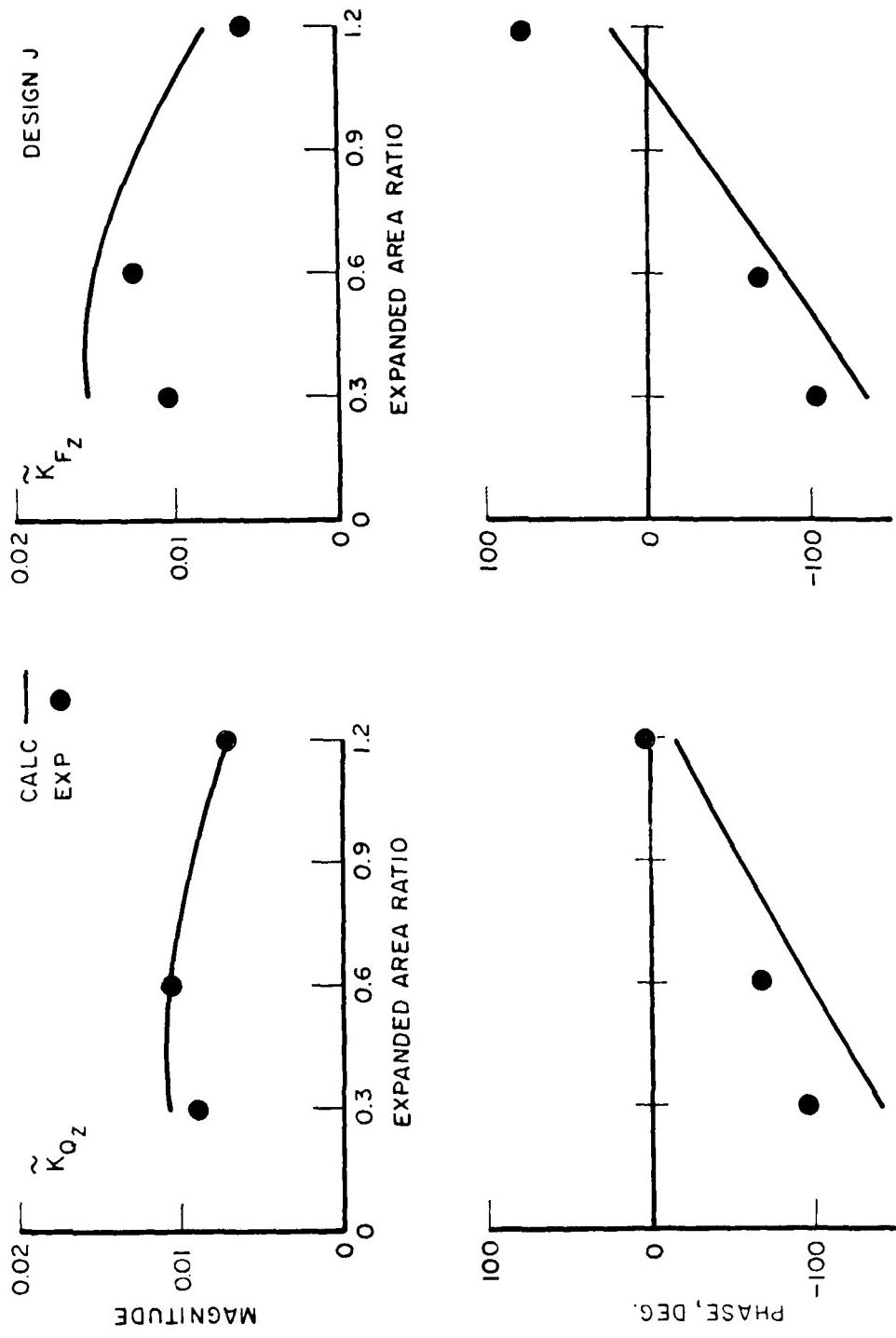
FIG. 9. BLADE-FREQUENCY TRANSVERSE FORCES AND MOMENTS OF DTNSRDC 3-BLADED PROPELLERS (IN 4-CYCLE SCREEN WAKE)
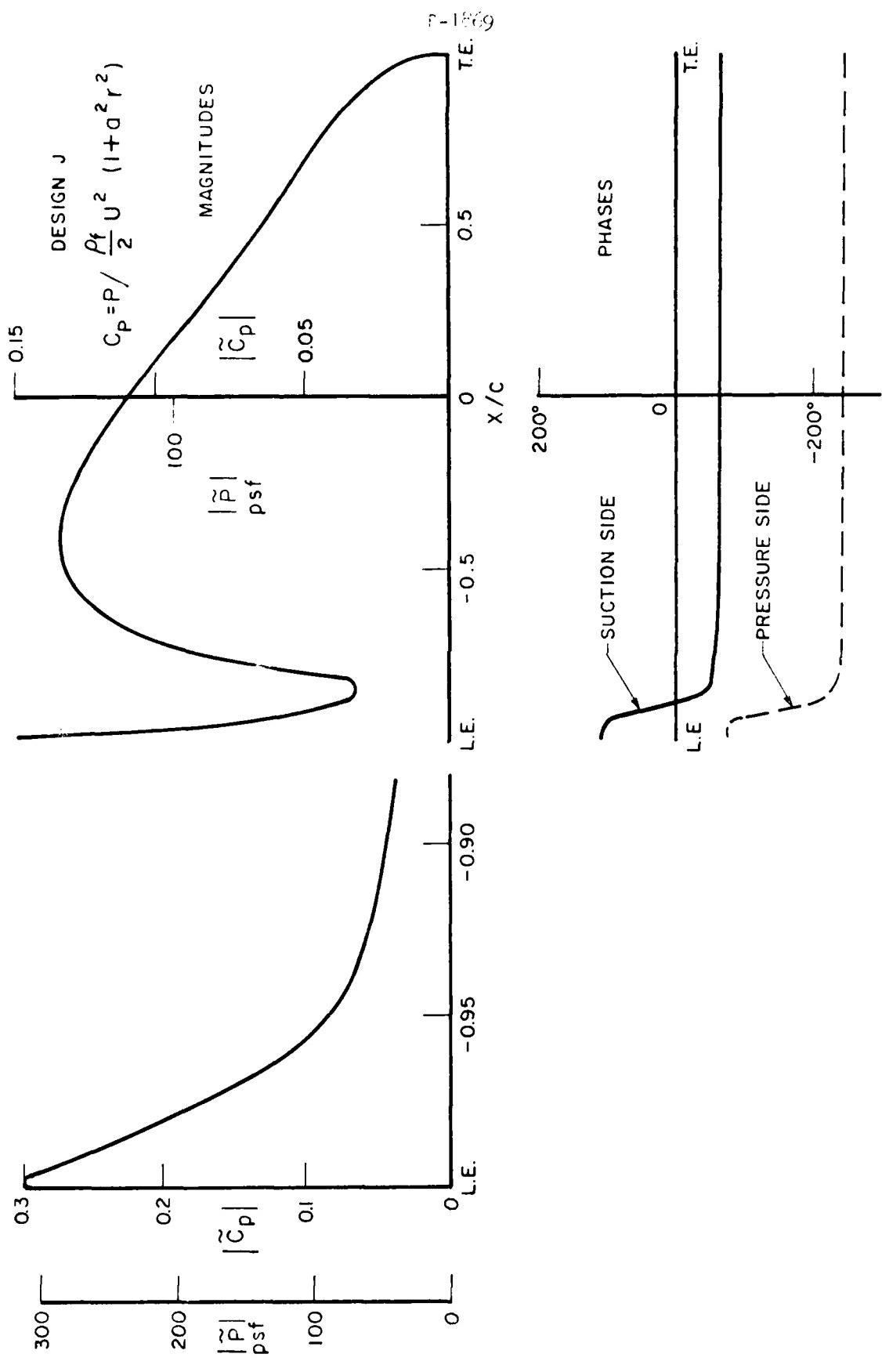
FIG. 10. BLADE-FREQUENCY CHORDWISE PRESSURE DISTRIBUTION ON EACH SIDE OF PROPELLER 4132 (EAR=0.3) AT 0.65 RADIUS
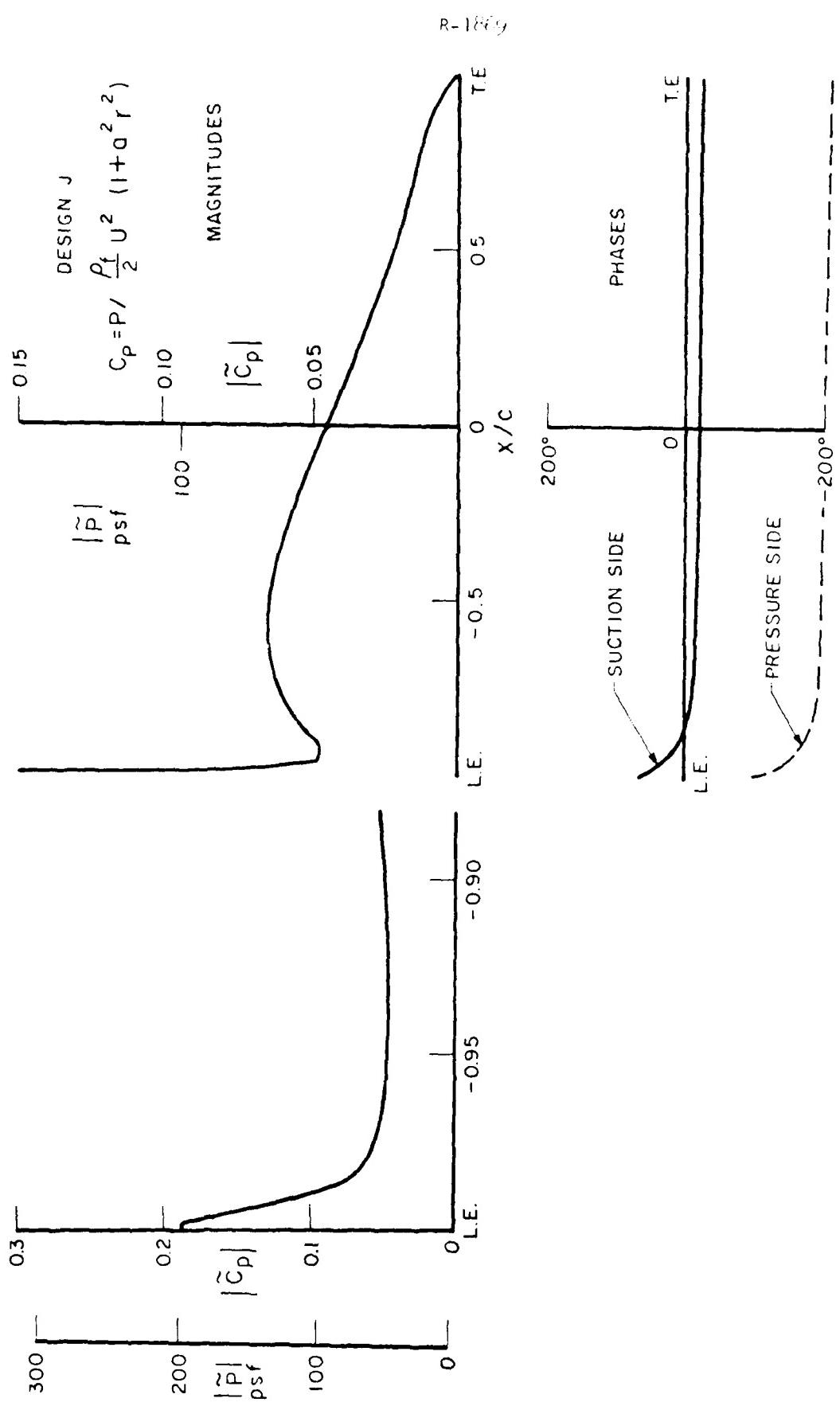
FIG. II. BLADE—FREQUENCY CHORDWISE PRESSURE DISTRIBUTION ON EACH SIDE OF PROPELLER 4118 (EAR=0.6) AT 0.65 RADIUS

DESIGN J

$$C_P = P / \frac{\rho_f}{2} U^2 (1 + a^2 r^2)$$

MAGNITUDES

PHASES
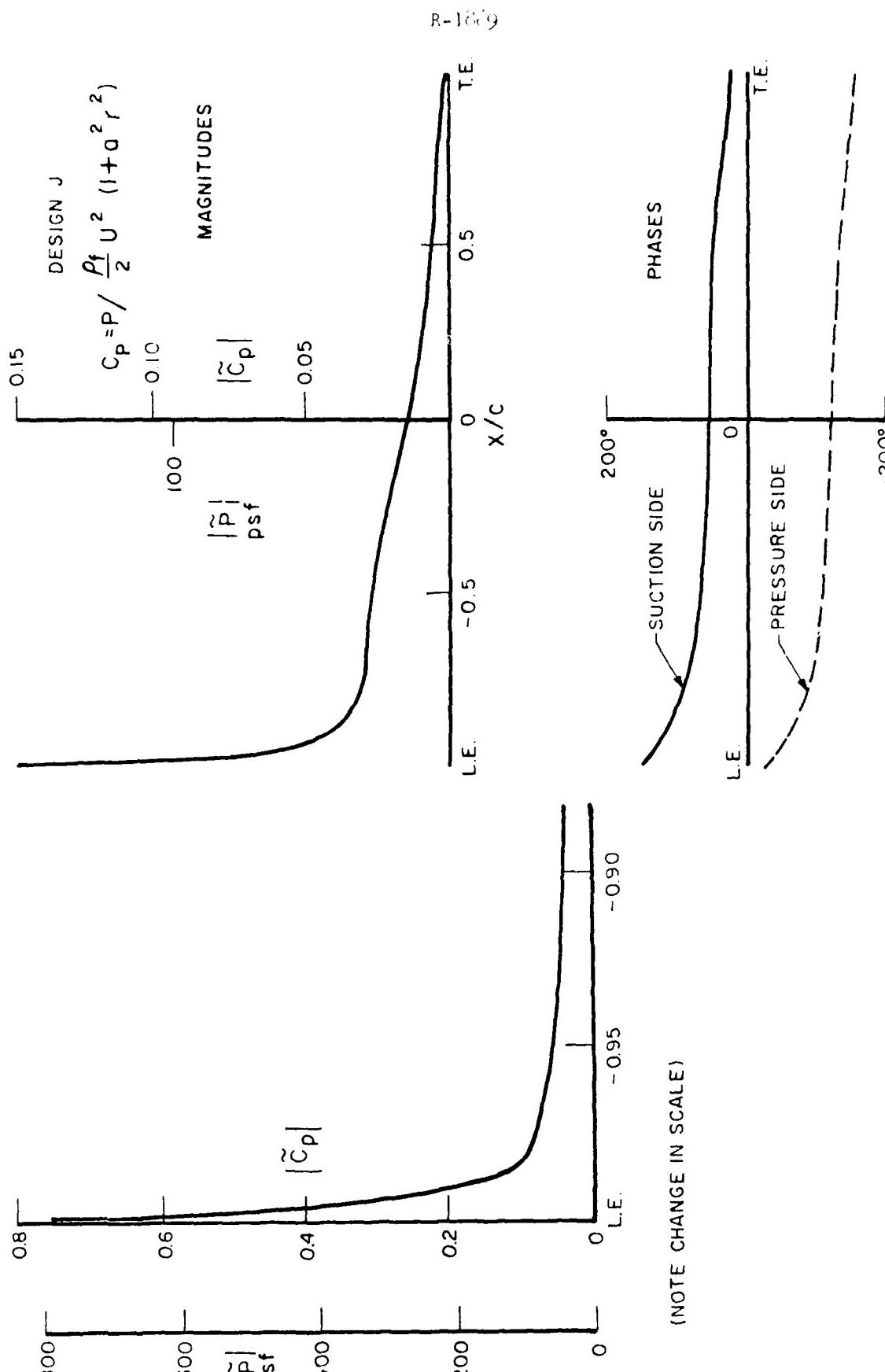
FIG. 12.   BLADE-FREQUENCY CHORDWISE PRESSURE DISTRIBUTION ON EACH SIDE OF PROPELLER 4133
(EAR=1.2) AT 0.65 RADIUS
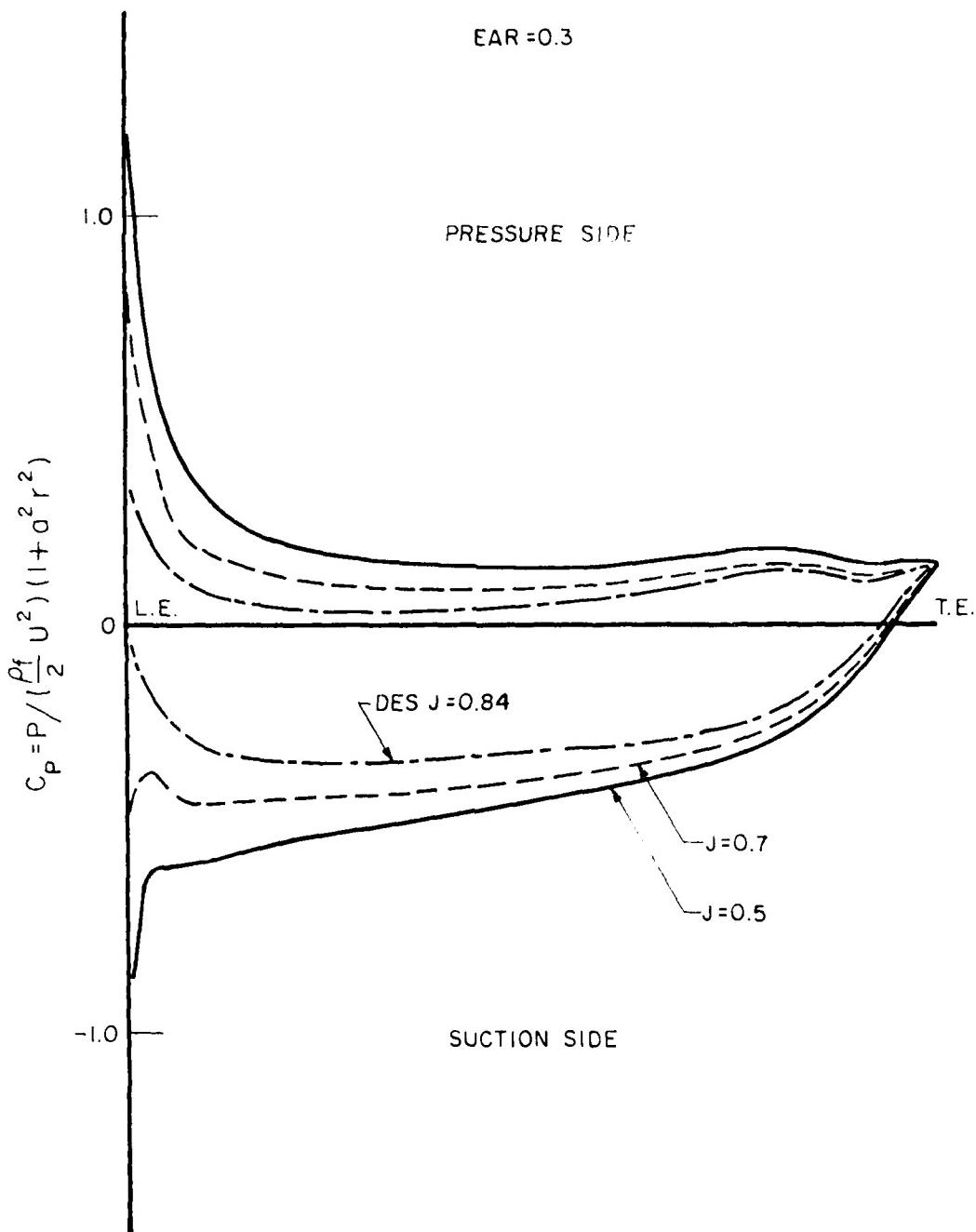
FIG. 13. STEADY-STATE CHORDWISE PRESSURE DISTRIBUTION AT
0.65 RADIUS ON PROPELLER 4132 (EAR=0.3) AT VARIOUS J.
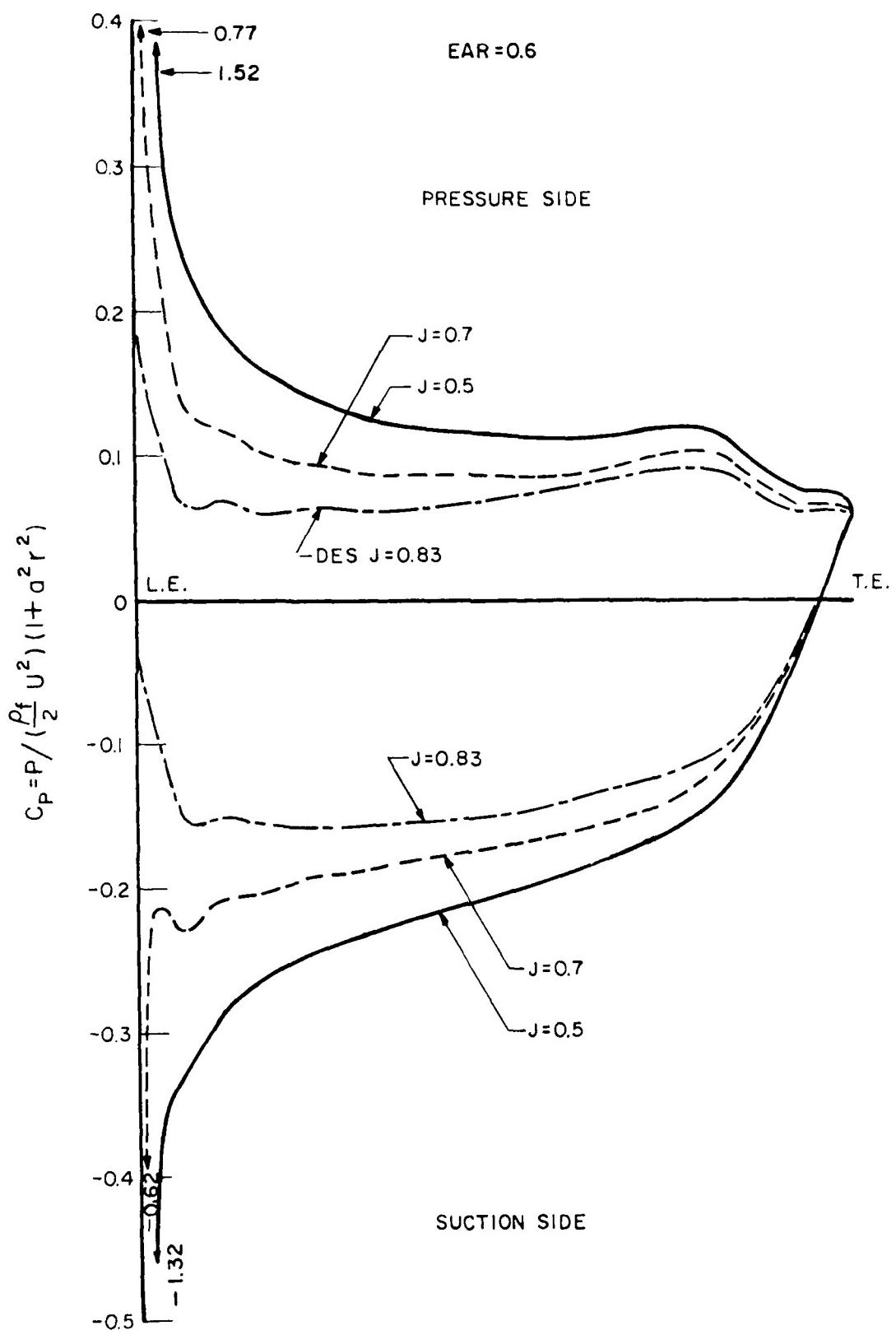
FIG. 14.   STEADY-STATE CHORDWISE PRESSURE DISTRIBUTION AT 0.65
RADIUS ON PROPELLER 4118 (EAR=0.6) AT VARIOUS J.
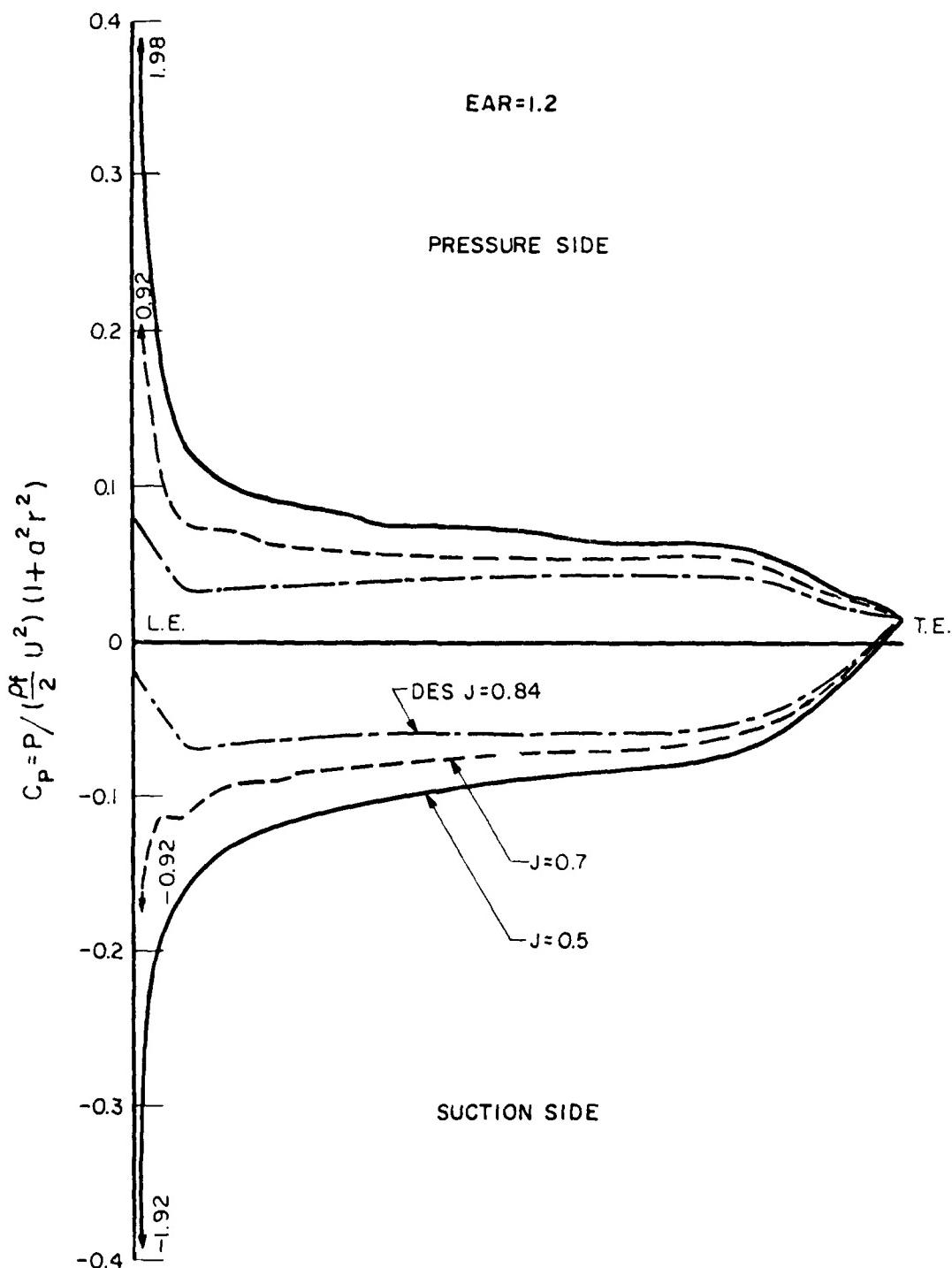
FIG.15.   STEADY-STATE CHORDWISE PRESSURE DISTRIBUTION AT
          0.65 RADIUS ON PROPELLER 4133(EAR=1.2) AT VARIOUS J.
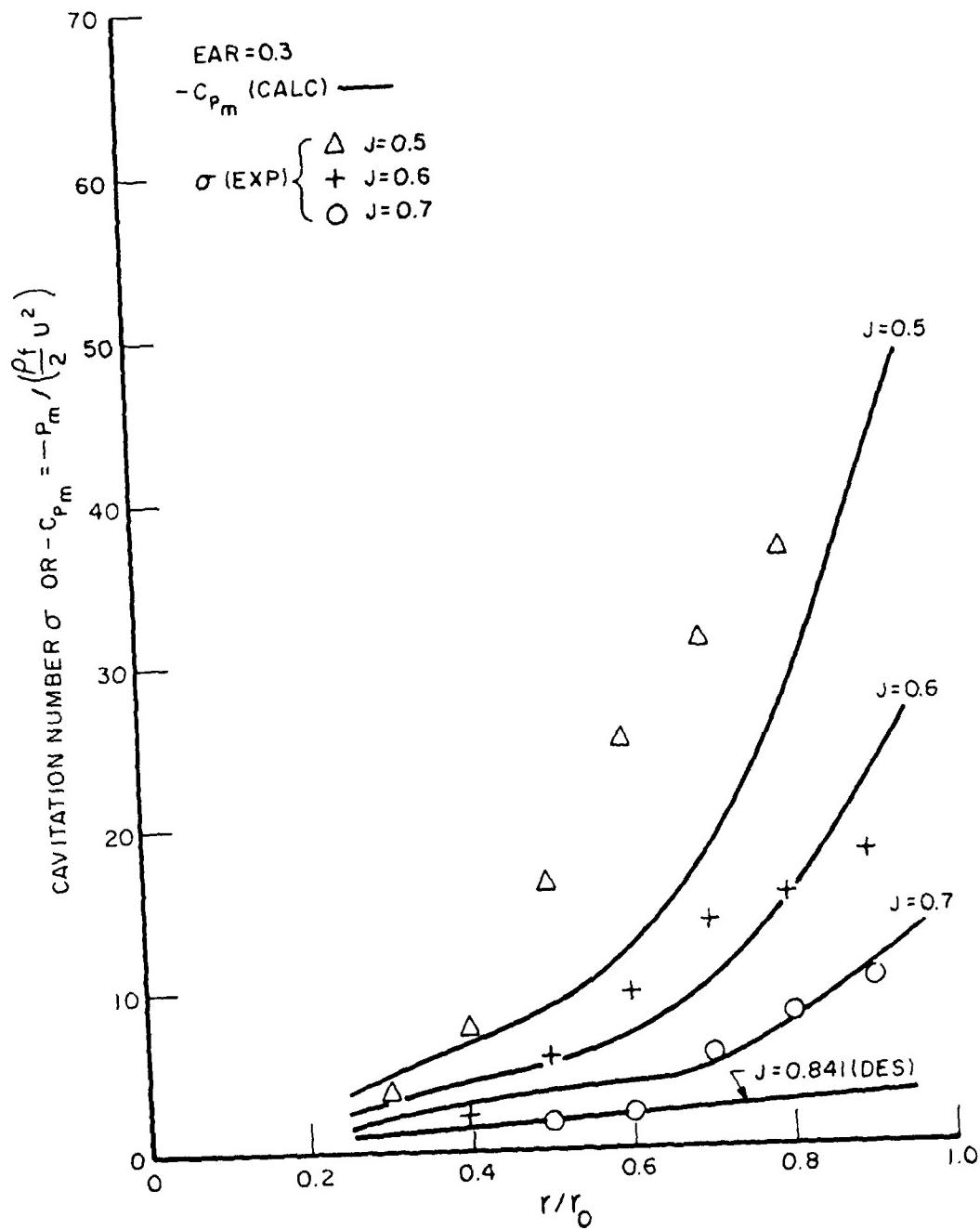
FIG. 16. COMPARISON OF CALCULATED $-C_{P_{min}}$ AND EXPERIMENTAL CAVITATION NUMBER σ, PROPELLER 4132 (EAR = 0.3)
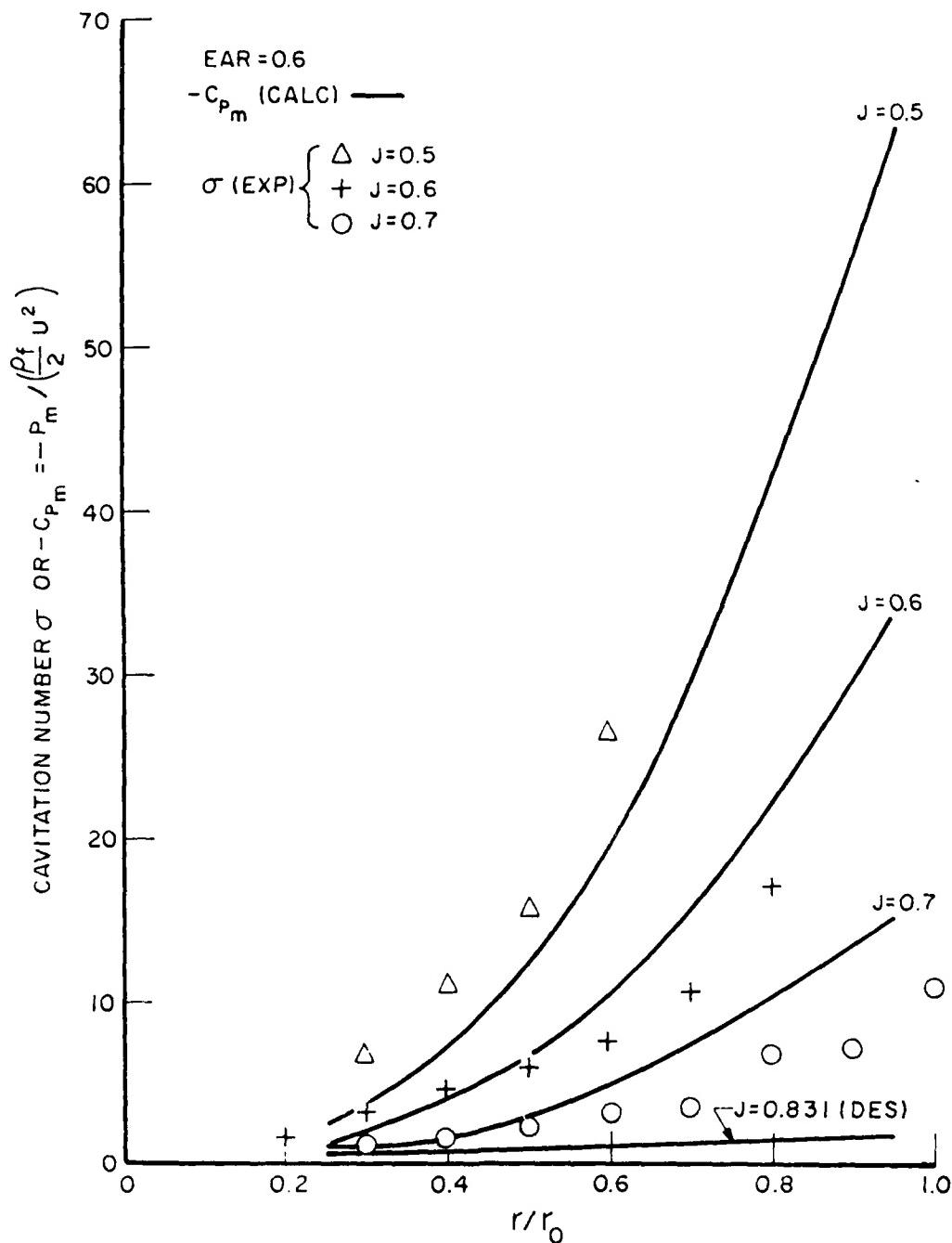
FIG. 17.   COMPARISON OF CALCULATED $-C_{P_{min}}$ AND EXPERIMENTAL
CAVITATION NUMBER σ, PROPELLER 4118 (EAR=0.6)
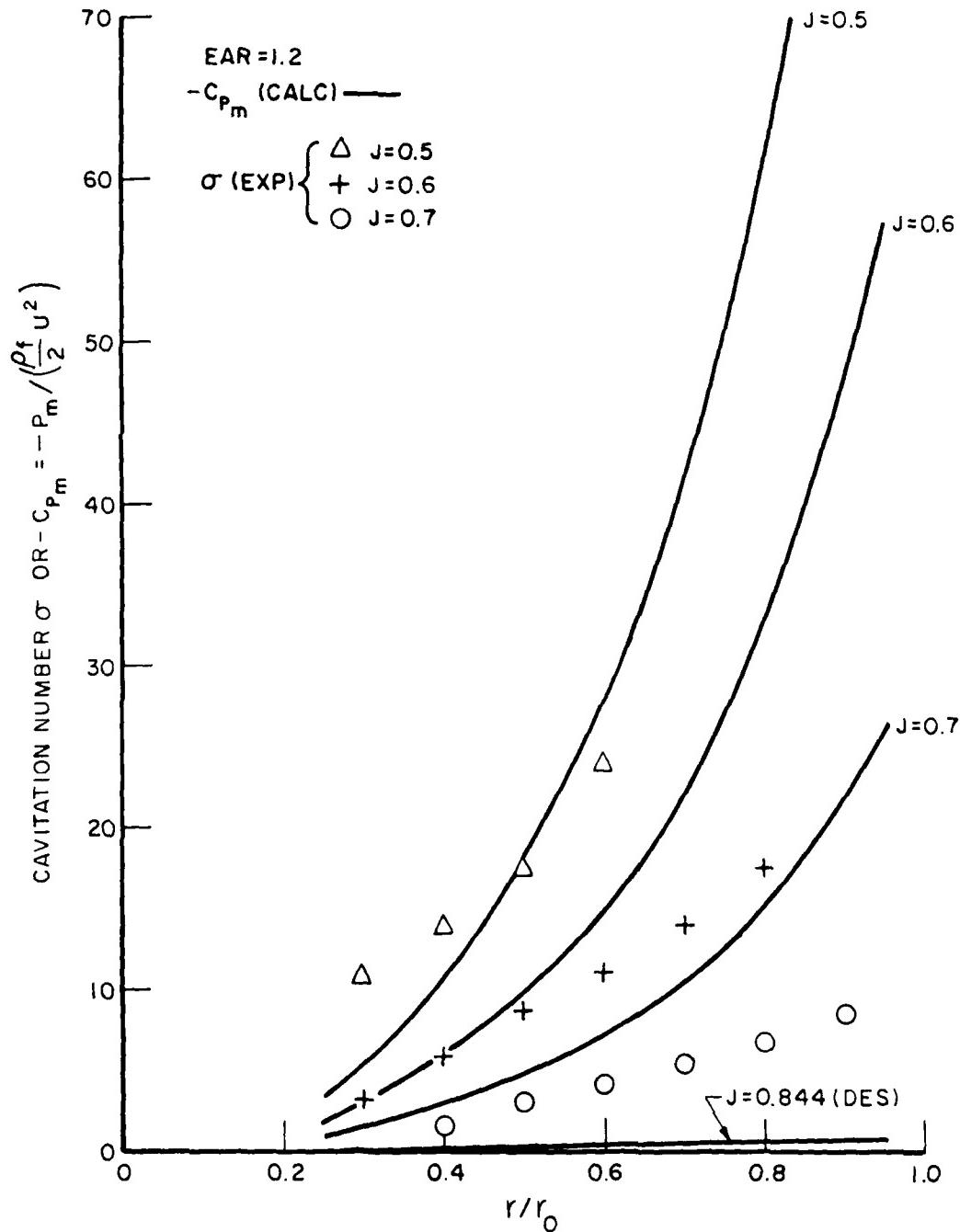
FIG. 18.   COMPARISON OF CALCULATED $-C_{P_{min}}$ AND EXPERIMENTAL
CAVITATION NUMBER σ, PROPELLER 4133 (EAR = 1.2)

APPENDIX A

1. Evaluation of the φ_α- and θ_α- Integrals of the Integral Equation (19)

1) $I^{(\bar{m})}(y) = \frac{1}{\pi} \int_0^\pi \Phi(\bar{m}) e^{iy\cos\varphi} d\varphi$

$\qquad I^{(1)}(y) = \frac{1}{\pi} \int_0^\pi (1-\cos\varphi) e^{iy\cos\varphi} d\varphi = J_0(y) - iJ_1(y)$

$\qquad I^{(2)}(y) = \frac{1}{\pi} \int_0^\pi (1+2\cos\varphi) e^{iy\cos\varphi} d\varphi = J_0(y) + i2J_1(y)$

$\qquad I^{(\bar{m}>2)}(y) = \frac{1}{\pi} \int_0^\pi \cos(\bar{m}-1)\varphi \, e^{iy\cos\varphi} d\varphi = i^{\bar{m}-1} J_{\bar{m}-1}(y)$

where $J_n(y)$ is the Bessel function of the first kind of order n and argument y

2) $\Lambda^{(n)}(z) = \int_0^\pi \Theta(\bar{n}) e^{-iz\cos\theta} \sin\theta \, d\theta$

$\qquad$ a) Birnbaum distribution

$\qquad\qquad \Lambda^{(1)}(z) = \frac{1}{\pi} \int_0^\pi \cot\frac{\theta}{2} e^{-iz\cos\theta} \sin\theta \, d\theta = J_0(z) - iJ_1(z)$

$\qquad\qquad \Lambda^{(\bar{n}>1)}(z) = \frac{1}{\pi} \int_0^\pi \sin(\bar{n}-1)\theta \, \sin\theta \, e^{-iz\cos\theta} d\theta$

$\qquad\qquad\qquad = \frac{(-i)^{\bar{n}-2}}{2} \left[J_{\bar{n}-2}(z) + J_{\bar{n}}(z) \right]$

$\qquad$ b) "Roof-top" distribution ($\bar{a}$ mean lines)

$\qquad\qquad \Lambda^{(1)}(z) = \int_0^{\cos^{-1}(1-2\bar{a})} e^{-iz\cos\theta} \sin\theta \, d\theta$

$\qquad\qquad\qquad + \int_{\cos^{-1}(1-2\bar{a})}^\pi \frac{(1+\cos\theta)}{2(1-\bar{a})} e^{-iz\cos\theta} \sin\theta \, d\theta$

$\qquad\qquad\qquad = e^{-iz} \left\{ \frac{i}{z} + \frac{1}{2(1-\bar{a})z^2} \left[e^{i2\bar{a}z} - e^{i2z} \right] \right\}$

$$\text{(For } \bar{a} = 1, \; \Lambda^{(1)}(z) = \frac{2 \sin z}{z} \; .)$$

$$\Lambda^{(\bar{n}>1)}(z) = 0$$

c) Sine series distribution

$$\Lambda^{(n)}(z) = \frac{1}{\pi} \int_0^\pi \sin \bar{n}\theta \, \sin\theta \, e^{-iz\cos\theta} \, d\theta$$

$$= \frac{(-i)^{\bar{n}-1}}{2} \left[J_{\bar{n}-1}(z) + J_{\bar{n}+1}(z) \right]$$

II. <u>Functions Required for Evaluating the Integrand of the Kernel Function</u>
<u>at the Singularity (see Reference 3) and the Propeller-generated</u>
<u>Moments (see section A,4)</u>

1) $I_1^{(\bar{m})}(y) = \frac{1}{\pi} \int_0^\pi \Phi(\bar{m}) \, e^{iy\cos\varphi} \cos\varphi \, d\varphi$

$$I_1^{(1)}(y) = -\frac{1}{2} \left[J_0(y) - J_2(y) \right] + iJ_1(y)$$

$$I_1^{(2)}(y) = \left[J_0(y) - J_2(y) \right] + iJ_1(y)$$

$$I_1^{(\bar{m}>2)}(y) = \frac{i^{\bar{m}-2}}{2} \left[- J_{\bar{m}}(y) + J_{\bar{m}-2}(y) \right]$$

2) $\Lambda_1^{\bar{n}}(z) = \int_0^\pi \Theta(\bar{n}) \, \sin\theta \, \cos\theta \, e^{-iz\cos\theta} \, d\theta$

a) Birnbaum distribution

$$\Lambda_1^{(1)}(z) = \frac{1}{2} \left[J_0(z) - J_2(z) \right] - iJ_1(z)$$

$$\Lambda_1^{(\bar{n}>1)}(z) = \frac{(-i)^{\bar{n}+1}}{4} \left[J_{\bar{n}-3}(z) - J_{\bar{n}+1}(z) \right]$$

b) "Roof-top distribution (ā mean lines)

$$\Lambda_1^{(1)}(z) = e^{-iz} \left\{ \frac{i}{z} + \frac{1}{z^2} + \frac{1}{z^2(1-\bar{a})} \left[\frac{(1-2\bar{a}}{2} - \frac{i}{z}) e^{i2\bar{a}z} \right. \right.$$

$$\left. \left. + \left(\frac{1}{2} + \frac{i}{z} \right) e^{i2z} \right] \right\}$$

(For $\bar{a} = 1$, $\Lambda_1^{(1)}(z) = \dfrac{i2}{z}\left(\cos z - \dfrac{\sin z}{z}\right)$.)

c) Sine series distribution

$$\Lambda_1^{(\bar{n})}(z) = \frac{(-i)^{\bar{n}+2}}{4}\left[J_{\bar{n}-2}(z) - J_{\bar{n}+2}(z)\right]$$

It is to be noted that the values for negative argument, i.e., $I^{(\bar{m})}(-y)$, $I_1^{(\bar{m})}(-y)$, $\Lambda^{(\bar{n})}(-z)$ and $\Lambda_1^{(\bar{n})}(-z)$, are the conjugates of the values given above.

APPENDIX B

TABLE OF INTEGRALS OF EQUATION (33)

1) $\displaystyle\int_0^\pi e^{\pm i\lambda\cos\theta}\sin\theta\,d\theta = \frac{2}{\lambda}\sin\lambda = 2G(\lambda)$ (=2 when $\lambda = 0$)

2) $\displaystyle\int_0^\pi e^{\pm i\lambda\cos\theta}\sin2\theta\,d\theta = \pm\frac{4i}{\lambda}\left(\frac{\sin\lambda}{\lambda} - \cos\lambda\right) = \pm4iF(\lambda)$ (=0 when $\lambda=0$)

3) $\displaystyle\int_0^\pi e^{\pm i\lambda\cos\theta}\sin3\theta\,d\theta = \frac{2}{\lambda}\left\{\sin\lambda\left(3-\frac{8}{\lambda^2}\right) + \frac{8}{\lambda}\cos\lambda\right\} = 6G(\lambda) - \frac{16}{\lambda}F(\lambda)$

                                                     (=2/3 when $\lambda=0$)

4) $\displaystyle\int_0^\pi e^{\pm i\lambda\cos\theta}\sin4\theta\,d\theta = \pm\frac{8i}{\lambda}\left\{\frac{\sin\lambda}{\lambda}\left(5-\frac{12}{\lambda^2}\right) + \cos\lambda\left(\frac{12}{\lambda^2}-1\right)\right\}$

$\displaystyle\qquad\qquad = \pm\frac{8i}{\lambda}\left\{4G(\lambda) + \left(\lambda-\frac{12}{\lambda}\right)F(\lambda)\right\}$ (=0 when $\lambda=0$)

5) $\displaystyle\int_0^\pi e^{\pm i\lambda\cos\theta}\cos\frac{\theta}{2}\,d\theta = 2J_0(\lambda) - 4\sum_{n=1}^\infty \frac{(-1)^n J_{2n}(\lambda)}{(4n+1)(4n-1)} \mp 4i\sum_{n=1}^\infty \frac{(-1)^n J_{2n-1}(\lambda)}{(4n-1)(4n-3)}$

$\displaystyle\qquad\qquad = B(\pm\lambda)$ (=2 when $\lambda=0$)

(Three or four terms of this series are sufficient.)

APPENDIX C

RESOLUTION OF FORCES AND MOMENTS

With the present coordinate system and sign convention (see Figures 1 to 3) the propeller, its N blades rotating with angular velocity $-\Omega$, is assumed to lie on a helicoidal surface given by

$$F(x,y,z) = x + \frac{1}{a} \tan^{-1} \frac{y}{z} = 0 \tag{C-1}$$

where in cylindrical coordinates

$$x = \varphi_0/a$$

$$y = -r \sin \theta$$

$$z = r \cos \theta$$

$$\theta = \varphi_0 - \Omega t + \bar{\theta}_n$$

The unit normal to this surface has components

$$\bar{n} = \frac{F_x, F_y, F_z}{\sqrt{F_x^2 + F_y^2 + F_z^2}} = \frac{1, z/ar^2, -y/ar^2}{\sqrt{1 + a^2 r^2}/ar} \tag{C-2}$$

so that

$$n_x = \frac{ar}{\sqrt{1 + a^2 r^2}} = \cos \beta$$

$$n_y = \frac{z/r}{\sqrt{1 + a^2 r^2}} = \sin \beta \cos \theta$$

$$n_z = \frac{-y/r}{\sqrt{1 + a^2 r^2}} = \sin \beta \sin \theta$$

where $\beta = \tan^{-1} \frac{1}{ar}$, the hydrodynamic pitch angle.

The elemental forces are then

$$\Delta F_x = \Delta P \cos \beta \; \Delta S$$

$$\Delta F_y = \Delta P \sin \beta \cos(\Omega t - \varphi_0 - \bar{\theta}_n) \; \Delta S \tag{C-3}$$

$$\Delta F_z = - \Delta P \sin \beta \sin(\Omega t - \varphi_0 - \theta_n) \; \Delta S$$

The elemental moments can be expressed as

$$\overrightarrow{\Delta Q} = \begin{vmatrix} i & j & k \\ x & y & z \\ n_x & n_y & n_z \end{vmatrix} (\Delta P)(\Delta S) \tag{C-4}$$

so that

$$\Delta Q_x = \Delta P(y n_z - z n_y) \; \Delta S \;\; = \; - \Delta P \; r \sin\beta \; \Delta S$$

$$\Delta Q_y = - \Delta P(x n_z - z n_x) \; \Delta S$$

$$= \Delta P \cdot r \left[\varphi_0 \tan\beta \sin\beta \sin(\Omega t - \varphi_0 - \bar{\theta}_n) + \cos\beta \cos(\Omega t - \varphi_0 - \bar{\theta}_n) \right] \Delta S$$

$$\Delta Q_z = \Delta P(x n_y - y n_x) \; \Delta S$$

$$= \Delta P \cdot r \left[\varphi_0 \tan\beta \sin\beta \cos(\Omega t - \varphi_0 - \bar{\theta}_n) - \cos\beta \sin(\Omega t - \varphi_0 - \bar{\theta}_n) \right] \Delta S$$

The total force in the x-direction (thrust) is

$$F_x = \mathrm{Re} \sum_{n=1}^{N} e^{iq(\Omega t - \bar{\theta}_n)} \int_S \int \Delta P^{(q)}(r,\varphi_0) \cos\beta(r) \; dS$$

Since $\; dS = r \, dr \, d\varphi_0 = r \theta_b^r \sin\varphi_\alpha \, d\varphi_\alpha \, dr, \; 0 \le \varphi_\alpha \le \pi$

$$L^{(q)}(r,\varphi_\alpha) = \Delta P^{(q)}(r,\varphi_0) \; r \; \theta_b^r$$

and $\;\; \displaystyle\sum_{n=1}^{N} e^{\pm iq\bar{\theta}_n} = \begin{cases} N \; \text{for } q = \ell N, \;\; \ell = 0,1,2,\ldots \\ 0 \; \text{otherwise} \end{cases}$

$$F_x = \text{Re}\left\{N\, e^{i\ell N\Omega t}\int_0^{\pi}\int_r L^{(\ell N)}(r,\varphi_\alpha)\cos\beta(r)\,\sin\varphi_\alpha\,d\varphi_\alpha\,dr\right\}$$

But $\displaystyle\int_0^{\pi} L^{(\ell N)}(r,\varphi_\alpha)\,\sin\varphi_\alpha\,d\varphi_\alpha = L^{(\ell N)}(r)$ the spanwise loading

therefore

$$F_x = \text{Re}\left\{N r_o\, e^{i\ell N\Omega t}\int_0^1 L^{(\ell N)}(r)\,\cos\beta(r)\,dr\right\} \tag{C-5}$$

The total force in the y-direction is

$$F_y = \text{Re}\sum_{n=1}^{N} e^{iq(\Omega t - \bar{\theta}_n)}\int_S \int \Delta P^{(q)}(r,\varphi_o)\sin\beta(r)\,\cos(\Omega t - \varphi_o - \bar{\theta}_n)\,dS$$

$$= \text{Re}\sum_{n=1}^{N}\frac{1}{2}\int_0^{\pi}\int_r L^{(q)}(r,\varphi_o)\sin\beta(r)\left[e^{i(q+1)(\Omega t - \bar{\theta}_n)}e^{i\theta_b^r\cos\varphi_\alpha}\right.$$

$$\left.+\; e^{i(q-1)(\Omega t - \bar{\theta}_n)}e^{-i\theta_b^r\cos\varphi_\alpha}\right]\cdot\sin\varphi_\alpha\,d\varphi_\alpha\,dr$$

Since $\displaystyle\sum_{n=1}^{N} e^{\pm i(q\pm1)\bar{\theta}_n} = \begin{cases} N & \text{for } q\pm1 = \ell N \\ 0 & \text{otherwise}\end{cases}$

$$F_y = \text{Re}\left\{\frac{N}{2}e^{i\ell N\Omega t}\int_0^{\pi}\int_r\left[L^{(\ell N-1)}(r,\varphi_\alpha)e^{i\theta_b^r\cos\varphi_\alpha} + L^{(\ell N+1)}(r,\varphi_\alpha)e^{-i\theta_b^r\cos\varphi_\alpha}\right]\right.$$

$$\left.\cdot\,\sin\beta(r)\,\sin\varphi_\alpha\,d\varphi_\alpha\,dr\right\}$$

The φ_α-integrals are

$$\int_0^{\pi} L^{(\ell N\mp1)}(r,\varphi_\alpha)\, e^{\pm i\theta_b^r\cos\varphi_\alpha}\,\sin\varphi_\alpha\,d\varphi_\alpha$$

$$= \int_0^{\pi}\sum_{\bar{n}=1} L^{(\ell N\mp1,\bar{n})}(r)\,\beta(\bar{n})e^{\pm i\theta_b^r\cos\varphi_\alpha}\,\sin\varphi_\alpha\,d\varphi_\alpha$$

$$= \sum_{\bar{n}=1} L^{(\ell N\mp1,\bar{n})}(r)\,\Lambda^{(\bar{n})}(\mp\theta_b^r) \tag{C-6}$$

where $\Lambda^{(\bar{n})}(\mp\theta_b^r)$ is given in Appendix A.

Therefore

$$F_y = \text{Re}\left\{\frac{Nr_o}{2} e^{i\ell N\Omega t} \int_o^1 \sum_{n=1} \left[L^{(\ell N-1,\bar{n})}(r)\, \Lambda^{(\bar{n})}(-\theta_b^r) + L^{(\ell N+1,\bar{n})}(r)\, \Lambda^{(\bar{n})}(\theta\right.\right.$$

$$\cdot \sin\beta(r)\, dr\Big\}$$

The vertical force is

$$F_z = \text{Re}\left\{\sum_{n=1}^N e^{iq(\Omega t-\bar{\theta}_n)} \int\int_S \Delta P^{(q)}(r,\varphi_o)\, \sin\beta(r)\, \sin(\Omega t-\varphi_o-\bar{\theta}_n)\, dS\right\}$$

and following the steps indicated in the development for F_y, the force is finally

$$F_z = \text{Re}\left\{\frac{-Nr_o}{2i} e^{i\ell N\Omega t} \int_o^1 \sum_{n=1} \left[L^{(\ell N-1,\bar{n})}(r)\, \Lambda^{(\bar{n})}(-\theta_b^r) - L^{(\ell N+1,\bar{n})}(r)\, \Lambda^{(\bar{n})}(\theta_b^r\right.\right.$$

$$\cdot \sin\beta(r)\, dr\Big\} \tag{C-8}$$

The moment about the x-axis (torque) is

$$Q_x = \text{Re}\left\{-\sum_{n=1}^N e^{iq(\Omega t-\bar{\theta}_n)} \int\int_S \Delta P^{(q)}(r,\varphi_o)\, \sin\beta(r)\, r\, dS\right\}$$

and by analogy with F_x this becomes

$$Q_x = \text{Re}\left\{-Nr_o^2 e^{i\ell N\Omega t} \int_o^1 L^{(\ell N)}(r)\, \sin\beta(r)\, r\, dr\right\} \tag{C-9}$$

The bending moment about the y-axis is

$$Q_y = \text{Re}\left\{\sum_{n=1}^N e^{iq(\Omega t-\bar{\theta}_n)} \int\int_S \Delta P^{(q)}(r,\varphi_o)[r\varphi_o \tan\beta(r)\, \sin\beta(r)\, \sin(\Omega t-\varphi_o-\bar{\theta}_n)\right.$$

$$+ r\cos\beta(r)\, \cos(\Omega t-\varphi_o-\bar{\theta}_n)]\, dS\Big\}$$

which with the trigonometric transformations employed before becomes

$$Q_y = \text{Re} \sum_{n=1}^{N} \frac{1}{2} \int_o \int_r \int^{\pi} L^{(q)}(r,\varphi_\alpha) \, i\theta_b^r \cos\varphi_\alpha \frac{\sin^2\beta(r)}{\cos\beta(r)} \left[e^{i(q+1)(\Omega t-\bar{\theta}_n)} e^{i\theta_b^r \cos\varphi_\alpha} \right.$$

$$- e^{i(q-1)(\Omega t-\bar{\theta}_n)} e^{-i\theta_b^r \cos\varphi_\alpha} \right] + \cos\beta(r) \left[e^{i(q+1)(\Omega t-\bar{\theta}_n)} e^{i\theta_b^r \cos\varphi_\alpha} \right.$$

$$\left. + e^{i(q-1)(\Omega t-\bar{\theta}_n)} e^{-i\theta_b^r \cos\varphi_\alpha} \right] r \sin\varphi_\alpha \, d\varphi_\alpha \, dr$$

$$= \text{Re} \frac{N}{2} e^{i\ell N\Omega t} \int_r \int \int_o^{\pi} i\theta_b^r \tan\beta(r) \sin\beta(r) \left[L^{(\ell N-1)}(r,\varphi_\alpha) e^{i\theta_b^r \cos\varphi_\alpha} \right.$$

$$\left. - L^{(\ell N+1)}(r,\varphi_\alpha) e^{-i\theta_b^r \cos\varphi_\alpha} \right] \cdot \cos\varphi_\alpha \sin\varphi_\alpha \, d\varphi_\alpha$$

$$+ \int_o^{\pi} \cos\beta(r) \left[L^{(\ell N-1)}(r,\varphi_\alpha) e^{i\theta_b^r \cos\varphi_\alpha} + L^{(\ell N+1)}(r,\varphi_\alpha) e^{-i\theta_b^r \cos\varphi_\alpha} \right]$$

$$\sin\varphi_\alpha \, d\varphi_\alpha \cdot r \, dr$$

The first φ_α-integral is

$$\int_o^{\pi} L^{(\ell N\mp 1)}(r,\varphi_\alpha) e^{\pm i\theta_b^r \cos\varphi_\alpha} \cos\varphi_\alpha \sin\varphi_\alpha \, d\varphi_\alpha$$

$$= \int_o^{\pi} \sum_{n=1}^{\infty} L^{(\ell N\mp 1,\bar{n})}(r) \, \Theta(\bar{n}) \, e^{\pm i\theta_b^r \cos\varphi_\alpha} \cos\varphi_\alpha \sin\varphi_\alpha \, d\varphi_\alpha$$

$$= \sum_{n=1}^{\infty} L^{(\ell N\mp 1,\bar{n})}(r) \, \Lambda_1^{(\bar{n})}(\mp\theta_b^r) \tag{C-10}$$

where $\Lambda_1^{(n)}(\ )$ is as defined in Appendix A. The second φ_α-integral
is given by (C-6). Finally,

$$Q_y = \text{Re} \frac{Nr_o^2}{2} e^{i\ell N\Omega t} \int_o^1 i\theta_b^r \sin\beta(r) \tan\beta(r) \sum_{n=1}^{\infty} \left[L^{(\ell N-1,\bar{n})}(r) \, \Lambda_1^{(\bar{n})}(-\theta_b^r) \right.$$

$$\left. - L^{(\ell N+1,\bar{n})}(r) \, \Lambda_1^{(\bar{n})}(\theta_b^r) \right] + \cos\beta(r) \sum_{n=1}^{\infty} \left[L^{(\ell N-1,\bar{n})}(r) \Lambda^{(\bar{n})}(-\theta_b^r) \right.$$

$$\left. + L^{(\ell N+1,\bar{n})}(r) \, \Lambda^{(\bar{n})}(\theta_b^r) \right] \cdot r \, dr \tag{C-11}$$

The bending moment about the z-axis is

$$Q_z = \text{Re} \sum_{n=1}^{N} e^{iq(\Omega t - \bar{\theta}_n)} \int\int_S \Delta P^{(q)}(r,\varphi_o)\left[r\varphi_o \tan\beta(r) \sin\beta(r) \cos(\Omega t - \varphi_o - \bar{\theta}_n)\right.$$

$$\left. - r\cos\beta(r) \sin(\Omega t - \varphi_o - \bar{\theta}_n)\right] dS$$

It can be shown that

$$Q_z = \text{Re}\left\{\frac{-Nr_o^2}{2i} e^{i\ell N\Omega t} \int_0^1 \left\{i\theta_b^r \sin\beta(r) \tan\beta(r) \sum_{n=1} \left[L^{(\ell N-1,\bar{n})}(r) \Lambda_1^{(\bar{n})}(-\theta_b^r)\right.\right.\right.$$

$$\left. + L^{(\ell N+1,\bar{n})}(r) \Lambda_1^{(\bar{n})}(\theta_b^r)\right] + \cos\beta(r) \sum_{n=1} \left[L^{(\ell N-1,\bar{n})}(r) \Lambda^{(\bar{n})}(-\theta_b^r)\right.$$

$$\left.\left.\left. - L^{(\ell N+1,\bar{n})}(r) \Lambda^{(\bar{n})}(\theta_b^r)\right]\right\} \cdot r\, dr\right\} \qquad (C-12)$$

In the text, and in the program as well, the hydrodynamic pitch angle $\beta(r)$ of the assumed helicoidal surface is replaced by the geometric pitch angle $\beta_p(r)$ of the actual propeller.

APPENDIX D

THE SINGULARITIES OF THE INTEGRANDS OF THE
BLADE PRESSURE DISTRIBUTION

In Equation (49) for the pressure due to thickness (non-lifting) it is seen that there is a singularity when $\rho = r$, $x = \xi$, $\theta_0 = \varphi_0$ and $\bar{\theta}_n = 0$ (i.e., $n = 1$). The singular part of the pressure can be expressed as (see Eq. (53) with the substitutions $\theta_0 = a\xi$ and $\varphi_0 = ax$):

$$P_{\tau_1} = i \frac{\rho_f U^2}{2\pi^2} \int_o^\pi \int_\rho \frac{\partial f(\rho,\theta_\alpha)}{\partial \theta_\alpha} \sqrt{1+a^2\rho^2} \int \int_{-\infty}^\infty k(IK)_o \, e^{ik(x-\xi)} \, dk$$

$$+ \sum_{m=1}^\infty \int_{-\infty}^\infty (IK)_m \left[(k-am)e^{i(k-am)(x-\xi)} + (k+am)e^{i(k+am)(x-\xi)} \right] dk \, d\theta_\alpha d\rho$$

$$(D-1)$$

For arbitrary thickness (see Eq. (32)).

$$\frac{\partial f(\rho,\theta_\alpha)}{\partial \theta_\alpha} \approx C_o(\rho) \cos \frac{\theta_\alpha}{2} + \sum_{n=1}^4 C_n(\rho) \sin n\theta_\alpha$$

where the coefficients are obtained as shown in sect. A,3,c. Then the trigonometric transformation

$$\xi = (\sigma^0 - \theta_b^\rho \cos\theta_\alpha)/a$$

yields

$$\cos\theta_\alpha = \frac{\sigma^0 - a\xi}{\theta_b^\rho}$$

$$\cos \frac{\theta_\alpha}{2} = \sqrt{\frac{\theta_b^\rho + \sigma^0 - a\xi}{2\theta_b^\rho}}$$

$$\sin\theta_\alpha \, d\theta_\alpha = \frac{a}{\theta_b^\rho} \, d\xi$$

$$\sin 2\theta_\alpha \, d\theta_\alpha = 2\sin\theta_\alpha \cos\theta_\alpha \, d\theta_\alpha = \frac{2a(\sigma^\rho - a\xi)d\xi}{(\theta_b^\rho)^2}$$

$$\sin 3\theta_\alpha \, d\theta_\alpha = \left[-1+4\frac{(\sigma^\rho - a\xi)^2}{(\theta_b^\rho)^2}\right]\frac{a}{\theta_b^\rho}\, d\xi$$

$$\sin 4\theta_\alpha = \left[8\left(\frac{\sigma^\rho - a\xi}{\theta_b^\rho}\right)^3 - 4\left(\frac{\sigma^\rho - a\xi}{\theta_b^\rho}\right)\right]\frac{a}{\theta_b^\rho}\, d\xi$$

and thus the slope can be expressed in the following form:

$$\frac{\partial f}{\partial\theta_\alpha}(\rho,\theta_\alpha)d\theta_\alpha \simeq \left\{\left[d_0(\rho) + \sqrt{d_1(\rho)} - d_2(\rho)\xi + d_3(\rho)\xi + d_4(\rho)\xi^2 + d_5(\rho)\xi^3\right]d\xi\right.$$

$$= \frac{F(\xi,\rho)}{\sqrt{1+a^2\rho^2}}\, d\xi$$

Equation (D-1) can be written as

$$P_1 = \frac{i\rho_f U^2}{2\pi}\int\int F(\xi,\rho)\left\{\int_{-\infty}^{\infty} k(IK)_0\, e^{ik(x-\xi)}dk\right.$$

$$+ \sum_{m=1}^{\infty}\int_{-\infty}^{\infty}(IK)_m\left[(k-am)e^{i(k-am)(x-\xi)}+(k+am)e^{i(k+am)(x-\xi)}\right]dk\right\}\, d\xi d\rho$$

$$(D-2)$$

For finite m the expansion of $1/R$ in the above has no singularity. The singular behavior is present only in the infinite m-series (see Reference 10). When $m \geq M$ large, the generalized mean value theorem can be used:

$$\int_c^d f(k)\, p(k)\, dk = f(A)\int_c^d p(k)\, dk, \quad c \leq A \leq d$$

where $f(k) = \begin{cases} I_m(|k|\rho)\, K_m(|k|r) & \text{for } \rho < r \\ I_m(|k|r)\, K_m(|k|\rho) & \text{for } r < \rho \end{cases}$

and $f(A) = I_m(|A|\rho) K_m(|A|r)$, etc. with $A \ll m$ (order).

By using Nicholson's[11] approximation for the product of the modified Bessel functions when $A \ll m$

$$f(A) \approx \frac{1}{2m} Z^m \text{ where } Z = \begin{cases} \rho/r & \text{for} \quad \rho < r \\ r/\rho & \text{for} \quad r < \rho \end{cases} \tag{D-3}$$

Then for large m the integral can be written as

$$I = \int_\xi \int_\rho F(\xi,\rho) \sum_{m=M}^\infty \frac{1}{m} Z^m \left\{ \cos am(x-\xi) \int_{-\infty}^\infty k e^{ik(x-\xi)} dk \right.$$

$$\left. + i \, a \, m \, \sin \, am(x-\xi) \int_{-\infty}^\infty e^{ik(x-\xi)} dk \right\} d\xi \, d\rho \tag{D-4}$$

From Jolley's collection of series summations[12]

$$ia \sum_{m=1}^\infty Z^m \sin ma(x-\xi) = \frac{iaZ \sin a(x-\xi)}{1-2Z \cos a(x-\xi)+Z^2} \text{ (see Jolley 499)}$$

Also $\dfrac{\partial}{\partial Z} \displaystyle\sum_{m=1}^\infty \frac{1}{m} Z^m \cos ma(x-\xi) = \frac{1}{Z} \sum_{m=1}^\infty Z^m \cos ma(x-\xi)$

$$= \frac{\cos a(x-\xi) - Z}{1-2Z \cos a(x-\xi)+Z^2} \text{ (see Jolley 500)}$$

Therefore

$$\sum_{m=1}^\infty \frac{1}{m} Z^m \cos ma(x-\xi) = \int \frac{\cos a(x-\xi) - Z}{1-2Z \cos a(x-\xi)+Z^2} \, dz$$

$$= -\frac{1}{2} \log \left[1 - 2Z \cos a(x-\xi)+Z^2 \right]$$

The m-series of (D-4) then is equivalent to

$$S_m = \left\{ -\frac{1}{2} \log \left[1 - 2z\cos a(x-\xi) + z^2\right] \int_{-\infty}^{\infty} k e^{ik(x-\xi)} dk \right.$$

$$+ \frac{iaZ\sin a(x-\xi)}{1 - 2 Z\cos a(x-\xi) + Z^2} \int_{-\infty}^{\infty} e^{ik(x-\xi)} dk$$

$$- \sum_{m=1}^{M} \frac{1}{m} Z^m \left\{ \cos am(x-\xi) \int_{-\infty}^{\infty} k e^{ik(x-\xi)} dk \right.$$

$$\left. + i\, am\, \sin am(x-\xi) \int_{-\infty}^{\infty} e^{ik(x-\xi)} dk \right\} \qquad (D-5)$$

where the finite m-series can be ignored since it is certainly not singular.

The k-integrals are evaluated as

$$\int_{-\infty}^{\infty} e^{ik(x-\xi)} dk = 2\pi\, \delta(x-\xi)$$

$$\qquad (D-6)$$

$$\int_{-\infty}^{\infty} k e^{ik(x-\xi)} dk = - i2\pi\, \delta'(x-\xi)$$

where $\delta(x-\xi)$ is the Dirac delta function and $\delta'(x-\xi)$ the derivative of this function with respect to $(x-\xi)$.

With the substitution of (D-5) and (D-6) and letting $x_o = x - \xi$, Equation (D-4) becomes

$$I = i2\pi \int_{x_o} \int_{\rho} F(x-x_o,\rho) \left\{ -\frac{1}{2} \log (1 - 2Z \cos ax_o + Z^2)\, \delta'(x_o) \right.$$

$$\left. - \frac{aZ \sin ax_o}{1 - 2Z \cos ax_o + Z^2}\, \delta(x_o) \right\}\, dx_o\, d\rho \qquad (D-7)$$

and integrating over x_o results in

$$I = +i\pi \int_{\rho} \left. \frac{\partial F(x-x_o)\rho)}{\partial x_o} \right|_{x_o=o} \log (1 - 2Z + Z^2)\, d\rho \qquad (D-8)$$

With $z = \rho/r$ or r/ρ,

$$\log(1-2Z+Z^2) = \log(1-Z)^2 = 2\log(1-Z)$$

$$= 2\log\left(\frac{r-\rho}{r}\right) \text{ or } 2\log\left(\frac{\rho-r}{\rho}\right)$$

hence the ρ-integral has a logarithmic singularity when $\rho \to r$ and this has a finite contribution and is integrable.

APPENDIX E

EVALUATION OF THE ρ-INTEGRATION IN
THE REGION OF THE SINGULARITY (SECTION B)

Let $\bar{K}(\rho)$ represent the integrand of the ρ-integration. It has been seen that when $\rho \rightarrow r$, $\bar{K}(\rho)$ varies as $\ln(\rho-r)$. A logarithmic singularity is integrable, but since the integration is performed numerically, special precautions must be taken. In the region of the singularity $\rho = r$, the integral is put in the form

$$I = \int_{r-\beta}^{r+\beta} \frac{M(\rho)}{\rho - r} d\rho \tag{E-1}$$

where $M(\rho) = (\rho-r)\bar{K}(\rho)$ so that $M = 0$ when $\rho = r$, and $\beta = \Delta r/2$.

The function $M(\rho)$ can be expanded about the singularity $\rho = r$ by the Lagrange formula

$$M(\rho) = \sum_{i=0}^{n} \frac{\Pi_n(\rho)}{(\rho-\rho_i)\ \Pi_n'(\rho_i)}\ M_{i+1} \quad i = 0,\ 1, \ldots n \tag{E-2}$$

where

$$\Pi_n(\rho) = (\rho-\rho_0)\ (\rho-\rho_1)\cdots(\rho-\rho_n)$$

$$\Pi_n'(\rho_i) = \frac{d}{d\rho}\ \Pi_n(\rho) \quad \text{evaluated at } \rho = \rho_i$$

and $M_{i+1} = M(\rho_i)$ (see Scarborough[13] and Watkins et al[14]).

In the strip from $r - \beta$ to $r + \beta$ (with $n = 4$ for the 5-point formula), $\rho_0 = r - \beta = r - 2\delta$, $\rho_1 = r - \delta$, etc. where $\delta = \beta/2$. Then

$$\Pi_n'(\rho_i) = (-1)^{4-i}\ \delta^4\ i!\ (4-i)! \tag{E-3}$$

and

$$M(\rho) = \frac{1}{\delta^4} \sum_{i=0}^{4} \frac{(-1)^i}{i!(4-1)!} \frac{(\rho-r+2\delta)(\rho-r+\delta)(\rho-r)(\rho-r-\delta)(\rho-r-2\delta)}{\rho - r + (2-i)\delta}\ M_{i+1} \tag{E-4}$$

where $M_3 = 0$ since $\rho_2 = r$.

The integral is

$$I = \int_{r-2\delta}^{r+2\delta} \frac{M(\rho)}{(\rho-r)} \, d\rho = \frac{1}{\delta^4} \int_{r-2\delta}^{r+2\delta} \left[g_0(\rho-r)^3 + \delta g_1(\rho-r)^2 + \delta^2 g_2(\rho-r) + \delta^3 g_3 + \frac{\delta^4 g_4}{\rho-r} \right] d\rho$$

(E-5)

where

$$g_0 = \frac{M_1 + M_5}{4!} - \frac{M_2 + M_4}{3!} + \frac{M_3}{2!}$$

$$g_1 = \frac{2(M_5 - M_1)}{4!} - \frac{(M_4 - M_2)}{3!}$$

$$g_2 = \frac{-(M_1 + M_5)}{4!} + \frac{4(M_2 + M_4)}{3!} - \frac{5M_3}{2!2!}$$

(E-6)

$$g_3 = \frac{2(M_1 - M_5)}{4!} - \frac{4(M_2 - M_4)}{3!}$$

$$g_4 = \frac{4}{2!2!} M_3 \quad (M_3 = 0)$$

then $I = \dfrac{1}{\delta^4} \left[\dfrac{\delta g_1}{3} 2(2\delta)^3 + \delta^3 g_3 \, 2(2\delta) \right]$

$$= \frac{16}{3} g_1 + 4g_3$$

or $I = \dfrac{1}{9}(M_5 - M_1) + \dfrac{16}{9}(M_4 - M_2)$

(E-7)

where $M_1 = -\beta \bar{K}_1 \quad (\rho = r - \beta)$

$M_2 = -\dfrac{\beta}{2} \bar{K}_2 \quad (\rho = r - \dfrac{\beta}{2})$

$M_4 = +\dfrac{\beta}{2} \bar{K}_4 \quad (\rho = r + \dfrac{\beta}{2})$

$M_5 = +\beta \bar{K}_5 \quad (\rho = r + \beta)$

Therefore

$$I = \frac{1}{9} \frac{\Delta r}{2} (\bar{K}_5 + \bar{K}_1) + \frac{16}{9} \frac{\Delta r}{4} (\bar{K}_4 + \bar{K}_2)$$

and

$$\frac{I}{\Delta r} = \frac{1}{18} (\bar{K}_5 + \bar{K}_1) + \frac{4}{9} (\bar{K}_4 + \bar{K}_2) \qquad\qquad (E-8)$$

DISTRIBUTION LIST

40	Commander
	David W. Taylor Naval Ship
	    Research and Development Center
	Bethesda, Md. 20084
	Attn: Code 1505 (1)
	       Code 5211.4 (39)
		1	Office of Naval Research
			Resident Representative
			715 Broadway (5th floor)
			New York, New York 10003

1   Officer-in-Charge
Annapolis Laboratory
Naval Ship Research and
    Development Center
Annapolis, Maryland 21402
Attn: Code 522.3 (Library)

7   Commander
Naval Sea Systems Command
Washington, D.C. 20360
Attn: SEA 09G32 (3)
       SEA 03512 (Peirce)
       SEA 037
       SEA 0322
       SEA 033

12   Director
Defence Documentation Center
5010 Duke Street
Alexandria, Virginia 22314

1   Office of Naval Research
800 N. Quincy Street
Arlington, Virginia 22217
Attn: Mr. R.D. Cooper (Code 438)

1   Office of Naval Research
Branch Office
492 Summer Street
Boston, Mass. 02210

1   Office of Naval Research
Branch Office (493)
536 S. Clark Street
Chicago, Illinois 60605

1   Chief Scientist
Office of Naval Research
Branch Office
1030 E. Green Street
Pasadena, Ca. 91106

1   Office of Naval Research
San Francisco Area Office
760 Market St., Rm 447
San Francisco, Ca. 94102

2   Director
Naval Research Laboratory
Washington, D.C. 20390
Attn: Code 2027
       Code 2629 (ONRL)

1   Commander
Naval Facilities Engineering
Command (Code 032C)
Washington, D.C. 20390

1   Library of Congress
Science and Technology Division
Washington, D.C. 20540

1   Commander
Naval Electronics Laboratory
    Center (Library)
San Diego, Ca. 92152

8   Commander
Naval Ship Engineering Center
Center Building
Prince Georges Center
Hyattsville, Maryland 20782
Attn: SEC 6034B
       SEC 6110
       SEC 6114H
       SEC 6120
       SEC 6136
       SEC 6144G
       SEC 6140B
       SEC 6148

1   Naval Ship Engineering Center
Norfolk Division
Small Craft Eng. Dept.
Norfolk, Virginia 23511
Attn: D. Blount (6660.03)

1	Library (Code 1640) Naval Oceanographic Office Washington, D.C. 20390	1	AFFOL/FYS (J. Olsen) Wright Patterson AFB Dayton, Ohio 45433
1	Technical Library Naval Proving Ground Dahlgren, Virginia 22448	1	Dept. of Transportation Library TAD-491.1 400 7th St., S.W. Washington, D.C. 20590
1	Commander (ADL) Naval Air Development Center Warminster, Penna. 18974	1	Charleston Naval Shipyard Technical Library Naval Base Charleston, S.C. 29408
1	Naval Underwater Weapons Research and Engineering Station (Library) Newport, R.I. 02840	1	Norfolk Naval Shipyard Technical Library Portsmouth, Virginia 23709
1	Commanding Officer (L31) Naval Civil Engineering Laboratory Port Hueneme, Ca. 93043	1	Philadelphia Naval Shipyard Philadelphia, Penna. 19112 Attn: Code 240
4	Commander Naval Undersea Center San Diego, Ca. 92132 Attn: Dr. A. Fabula (6005) Dr. J. Hoyt (2501) Library (13111)	1	Portsmouth Naval Shipyard Technical Library Portsmouth, N.H. 03801
1	Director Naval Research Laboratory Underwater Sound Reference Div. P.O. Box 8337 Orlando, Florida 32806	1	Puget Sound Naval Shipyard Engineering Library Bremerton, Wash. 98314
1	Library Naval Underwater Systems Center Newport, R.I. 02840	1	Long Beach Naval Shipyard Technical Library (246L) Long Beach, Ca. 90801
		1	Hunters Point Naval Shipyard Technical Library (Code 202.3) San Francisco, Ca. 94135
1	Research Center Library Waterways Experiment Station Corps of Engineers P.O. Box 631 Vicksburg, Mississippi 39180	1	Pearl Harbor Naval Shipyard Code 202.32 Box 400, FPO San Francisco, Ca. 96610
2	National Bureau of Standards Washington, D.C. 20234 Attn: P. Klebanoff (FM 105) Fluid Mechanics Hydraulic Section	1	Mare Island Naval Shipyard Shipyard Technical Library Code 202.3 Vallejo, Ca. 94592
1	AFOSR/NAM 1400 Wilson Blvd. Arlington, Virginia 22209	1	Assistant Chief Design Engineer for Naval Architecture (Code 250) Mare Island Naval Shipyard Vallejo, Ca. 94592

3   U.S. Naval Academy
Annapolis, Maryland 21402
Attn: Technical Library
Dr. Bruce Johnson
Prof. P. Van Mater, Jr.

3   Naval Postgraduate School
Monterey, Ca. 93940
Attn: Library, Code 2124
Dr. T. Sarpkaya
Prof. J. Miller

1   Capt. L.S. McCready, USMS
Director, National Maritime
Research Center
U.S. Merchant Marine Academy
Kings Point, L.I., N.Y. 11204

1   U.S. Merchant Marine Academy
Kings Point, L.I., N.Y. 11204
Attn: Academy Library

1   Library
The Pennsylvania State Univ.
Ordnance Research Laboratory
P.O. Box 30
State College, Penna. 16801

1   Bolt, Beranek and Newman
1701 N. For Myer Drive
Arlington, Virginia 22211
Attn: Dr. F. Jackson

1   Bolt, Beranek and Newman
50 Moulton Street
Cambridge, Mass. 02138
Attn: Library

1   Bethlehem Steel Corporation
Center Technical Division
Sparrows Point Yard
Sparrows Point, Maryland 21219

1   Bethlehem Steel Corporation
25 Broadway
New York, New York 10004
Attn: Library (Shipbuilding)

1   Cambridge Acoustical Asso., Inc.
1033 Massachusetts Ave.
Cambridge, Mass. 02138
Attn: Dr. M. Junger

1   CALSPAN Corporation
P.O. Box 235
Buffalo, New York 14221
Attn: Dr. A. Ritter
Aerodynamics Res. Dept.

1   Esso International
Design Division, Tanker Dept.
15 West 51st Street
New York, New York 10019

1   Mr. V. Boatwright, Jr.
R&D Manager
Electric Boat Division
General Dynamics Corporation
Groton, Conn. 06340

1   Gibbs and Cox, Inc.
21 West Street
New York, New York 10006
Attn: Technical Information Control

2   Hydronautics, Inc.
Pindell School Road
Howard County
Laurel, Maryland 20810
Attn: Library
Mr. M. Gertler

2   McDonnell Douglas Aircraft Co.
3855 Lakewood Blvd.
Long Beach, Ca. 90801
Attn: J. Hess
T. Cebeci

1   Lockheed Missiles and Space Co.
P.O. Box 504
Sunnyvale, Ca. 94088
Attn: Mr. R. L. Waid, Dept. 57-74
Bldg. 150, Facility 1

1   Newport News Shipbuilding and
Dry Dock Company
4101 Washington Ave.
Newport News, Virginia 23607
Attn: Technical Library Dept.

1   North American Aviation, Inc.
Space and Information Systems
12214 Lakewood Blvd.
Downey, Ca. 90241
Attn: Mr. Ben Ujihara

1 Nielsen Engineering & Research, Inc.
510 Clude Avenue
Mountain View, Ca. 94043
Attn: Mr. S. Spangler

1 Oceanics, Inc.
Technical Industrial Park
Plainview, L.I., N.Y. 11803

1 Society of Naval Architects
    and Marine Engineers
74 Trinity Place
New York, New York 10006
Attn: Technical Library

1 Sun Shipbuilding & Dry Dock Co.
Chester, Penna. 19000
Attn: Chief Naval Architect

1 Sperry Systems Management Div.
Sperry Rand Corporation
Great Neck, N.Y. 11020
Attn: Technical Library

1 Stanford Research Institute
Menlo Park, Ca. 94025
Attn: Library G-021

2 Southwest Research Institute
P.O. Drawer 28510
San Antonio, Texas 78284
Attn: Applied Mechanics Review
      Dr. H. Abramson

1 Tracor, Inc.
6500 Tracor Lane
Austin, Texas 78721

1 Mr. Robert Taggart
3930 Walnut Street
Fairfax, Virginia 22030

1 Ocean Engineering Department
Woods Hole Oceanographic Inst.
Woods Hole, Mass. 02543

1 Worcester Polytechnic Inst.
Alden Research Laboratories
Worcester, Mass. 01609
Attn: Technical Library

1 Applied Physics Laboratory
University of Washington
1013 N. E. 40th St.
Seattle, Washington 98105
Attn: Technical Library

1 University of Bridgeport
Bridgeport, Conn. 06602
Attn: Dr. E. Uram

1 Cornell University
Graduate School of Aerospace Eng.
Ithaca, New York 14850
Attn: Prof. W. R. Sears

4 University of California
Naval Architecture Department
College of Engineering
Berkeley, Ca. 94720
Attn: Library
      Prof. W. Webster
      Prof. J. Paulling
      Prof. J. Wehausen

3 California Institute of Technology
Pasadena, Ca. 91109
Attn: Aeronautics Library
      Dr. T. Y. Wu
      Dr. A. J. Acosta

1 Docs/Repts/Trans. Section
Scripps Institution of
    Oceanography Library
University of California, San Diego
P.O. Box 2367
La Jolla, Ca. 92037

1 Catholic University of America
Washington, D.C. 20017
Attn: Dr. S. Heller
      Dept. of Civil & Mech. Eng.

1 Colorado State University
Foothills Campus
Fort Collins, Colorado 80521
Attn: Reading Room
      Engineering Research Center

1 University of California at San Diego
La Jolla, Ca. 92038
Attn: Dr. A. T. Ellis
      Dept. of Applied Math.

2   Florida Atlantic University
Ocean Engineering Department
Boca Raton, Fla. 33432
Attn: Technical Library
      Dr. S. Dunne

2   Harvard University
Pierce Hall
Cambridge, Mass. 02138
Attn: Prof. G. Carrier
      Gordon McKay Library

1   University of Hawaii
Dept. of Ocean Engineering
2565 The Mall
Honolulu, Hawaii 96822
Attn: Dr. C. Bretschneider

1   University of Illinois
Urbana, Illinois 61801
Attn: Dr. J. Robertson

3   Institute of Hydraulic Res.
The University of Iowa
Iowa City, Iowa 52240
Attn: Library
      Dr. L. Landweber
      Dr. J. Kennedy

1   The John Hopkins University
Baltimore, Md. 21218
Attn: Prof. O. Phillips
      Mechanics Dept.

1   Kansas State University
Engineering Experiment Station
Seaton Hall
Manhattan, Kansas 66502
Attn: Prof. D. Nesmith

1   University of Kansas
Chm Civil Engr. Dept. Library
Lawrence, Kansas 60644

5   Department of Ocean Engineering
Massachusetts Inst. of Technology
Cambridge, Mass. 02139
Attn: Department Library
      Prof. P. Leehey
      Prof. P. Mandel
      Prof. M. Abkowitz
      Dr. J. Newman

1   Parsons Laboratory
Massachusetts Inst. of Technology
Cambridge, Mass. 02139
Attn: Prof. A. Ippen

5   St. Anthony Falls Hydraulic Laboratory
University of Minnesota
Mississippi River at 3rd Ave. S.E.
Minneapolis, Minnesota 55414
Attn: Prof. E. Silberman
      Mr. J. Wetzel
      Mr. F. Schiebe
      Mr. J. Killen
      Dr. C. Song

3   Department of Naval Architecture
     and Marine Engineering
University of Michigan
Ann Arbor, Michigan 48104
Attn: Library
      Dr. T. F. Ogilvie
      Prof. F. Hammitt

2   College of Engineering
University of Notre Dame
Notre Dame, Indiana 46556
Attn: Engineering Library
      Dr. A. Strandhagen

2   New York University
Courant Inst. of Math. Sciences
251 Mercier Street
New York, New York 10012
Attn: Prof. A. Peters
      Prof. J. Stoker

1   City College, CUNY
Convent Ave. and 138th St.
New York, N.Y. 10031
Attn: Prof. W. Pierson, Jr.

1   Dept. of Aerospace and Mechanical Sciences
Princeton University
Princeton, N.J. 08540
Attn: Prof. G. Mellor

3   Davidson Laboratory
Stevens Institute of Technology
711 Hudson Street
Hoboken, New Jersey 07030
Attn: Library
      Dr. J. Breslin
      Dr. S. Tsakonas

1 Applied Research Laboratory Library
University of Texas
P.O. Box 8029
Austin, Texas 78712

1 College of Engineering
Utah State University
Logan, Utah 84321
Attn: Dr. R. Jeppson

2 Stanford University
Stanford, Ca. 94305
Attn: Engineering Library
   Dr. R. Street

3 Webb Institute of Naval Architecture
Crescent Beach Road
Glen Cove, L.I., N.Y. 11542
 Attn: Library
    Prof. E. V. Lewis
    Prof. L. W. Ward

1 National Science Foundation
Engineering Division Library
1800 G Street, N.W.
Washington, D.C. 20550

1 University of Connecticut
Box U-37
Storrs, Conn. 06268
Attn: Dr. V. Scottron
   Hydraulic Research Lab.

1 Applied Research Laboratory
P.O. Box 30
State College, Pa. 16801
Attn: Dr. B. Parkin, Director
   Garfield Thomas Water Tunnel

1 Dr. Michael E. McCormick
Naval Systems Engineering Department
U.S. Naval Academy
Annapolis, Maryland 21402

1 Dr. Douglas E. Humphreys (Code 712)
Naval Coastal Systems Laboratory
Panama City, Florida 32401